High-resolution multi-proxy analysis on paleoclimatic changes in the Eastern Mediterranean during the Last Interglacial

Master Thesis

By

Devika Varma

(20141031)

Indian Institute of Science Education and Research, Pune

Under the guidance of

Prof. Dr. Kai-Uwe Hinrichs

MARUM & Department of Geosciences

University of Bremen, Germany

IISER PUNE

marum Center for Marine Environmental Sciences

Universität Bremen

Certificate

This is to certify that this dissertation entitled "**High-resolution multi-proxy analysis on paleoclimatic changes in the Eastern Mediterranean during the Last Interglacial**", towards the partial fulfilment of the BS-MS dual degree programme at the Indian Institute of Science Education and Research, Pune, represents study/work carried out by Devika Varma at MARUM, University of Bremen, under the supervision of Dr. Kai-Uwe Hinrichs**,** Professor of Organic Geochemistry**,** MARUM & Department of Geosciences, University of Bremen, Germany, during the academic year 2018-2019.

Prof. Kai-Uwe Hinrichs
University of Bremen

Devika Varma
IISER, Pune

Date: 14th March 2019

Declaration

I hereby declare that the research work presented in the report entitled "**High-resolution multi-proxy analysis on paleoclimatic changes in the Eastern Mediterranean during the Last Interglacial**" have been carried out by me at MARUM & Department of Geosciences, University of Bremen under the supervision of Dr. Kai-Uwe Hinrichs and the same has not been submitted elsewhere for any other degree.

Devika Varma
IISER, Pune

Prof. Kai-Uwe Hinrichs
University of Bremen

Date: 14th March 2019

Acknowledgements

First and foremost, I want to thank my supervisor Dr. Kai-Uwe Hinrichs, for giving me the wonderful opportunity to work in the lab and using the high-tech machines and all other facilities that made this study possible. I express my sincere gratitude to Dr. Kai for giving me all the valuable feedbacks and supporting me throughout the project.

I also take this opportunity to thank the BremenIDEA programme for supporting me through the initial stages of the project. The same gratitude goes to Dr. Hartmut Schulz for providing me with the sediment core used in this study.

Special thanks to Dr. Igor Obreht for proofreading my report and for all the guidance and encouragement provided. Hearty thanks to all the members of the ZOOMecular team and AG Hinrichs; Jenny, Xavi and Stani for all technical and lab assistance, Dr. Heidi Taubner for µ-XRF support, Dr. Lars Wörmer and Dr. Tiffany Napier for timely discussions, Dr. David De Vleeschouwer and Dr. Julius Lipp for programming scripts, Susanne and Yvonne for their help in and out of the lab. And thanks to all other members of the team in providing a creative and cheerful environment to work in and making my time in Germany way easier and enjoyable.

Further thanks go to my professors at IISER, Dr. Sudipta Sarkar and Dr. Neena Joseph for their constant support and motivation from the beginning.

I also express my deep gratitude to my parents, grandparents and uncle for putting up with me and constantly helping me to stay on track. Thank you to Deba and Seethu for believing in me and pushing me forward.

Contents

List of Figures

List of tables

ABSTRACT

The climatic optimum during the last interglacial was the time interval during which the average sea level was ~5-6m higher, and more humid and warmer climate (by ~3°C from the present value) prevailed. However, studies done so far related to this period fail to provide any direct indicator of climate and environmental variability on annual to decadal timescales. Hence in this study, using recent advancements in molecular Mass Spectrometry Imaging, an ultra-high resolution reconstruction of the paleoenvironmental conditions ~125,000 years ago was done.

Organic-rich sapropel S5 from the Eastern Mediterranean, formed during the last interglacial, comprises informative biomarkers like glycerol dialkyl glycerol tetraethers, alkenones and fatty acids, which were used to generate molecular stratigraphic records of their distribution. $U^{k'}_{37}$ and CCaT paleothermometry generated from these biomarkers are indicative of sea surface temperature as well as oxygen limitation in response to the stratification of water column respectively, during the sapropel deposition. The average chain length of long-chain fatty acids records the regional vegetation changes in the Mediterranean borderlands and plausibly indicates the response of vegetation on the shift of Inter-Tropical Convergence Zone and variation in the North African monsoonal intensity. Various elemental abundances document a complex interplay of oceanographic and hydrological conditions during this period. For example, Br abundances indicate increased productivity during sapropel deposition, while K, Ti and Zr indicate variations in drainage and dust intensity.

The CCaT proxy derived sea surface temperature and average chain length of long-chain fatty acids show prominent multi-decadal oscillations during this period. Similar oscillations in elemental data (for Ca, Fe, Ti and K) highlight a coupling between low and mid-latitude hydrodynamic changes and teleconnections between various components of the global climate system during the last interglacial.

1. INTRODUCTION

1.1 The Mediterranean Sea, its circulation pattern and climate

The Mediterranean Sea is located in mid-latitude roughly between 30°N and 45°N and it spans from 5°W to 36°E (Figure 1). It has an average depth of 1500 m and the deepest point being ca. 5260 m (in the Calypso Deep). It is surrounded by landmasses from all sides with a small passage connecting to the open Atlantic Ocean and thus making it highly responsive to subtle external forcing and climatic changes in the surrounding terrestrial area. Hence the sediments in the Mediterranean serve as an excellent archive of the regional climatic forcings.

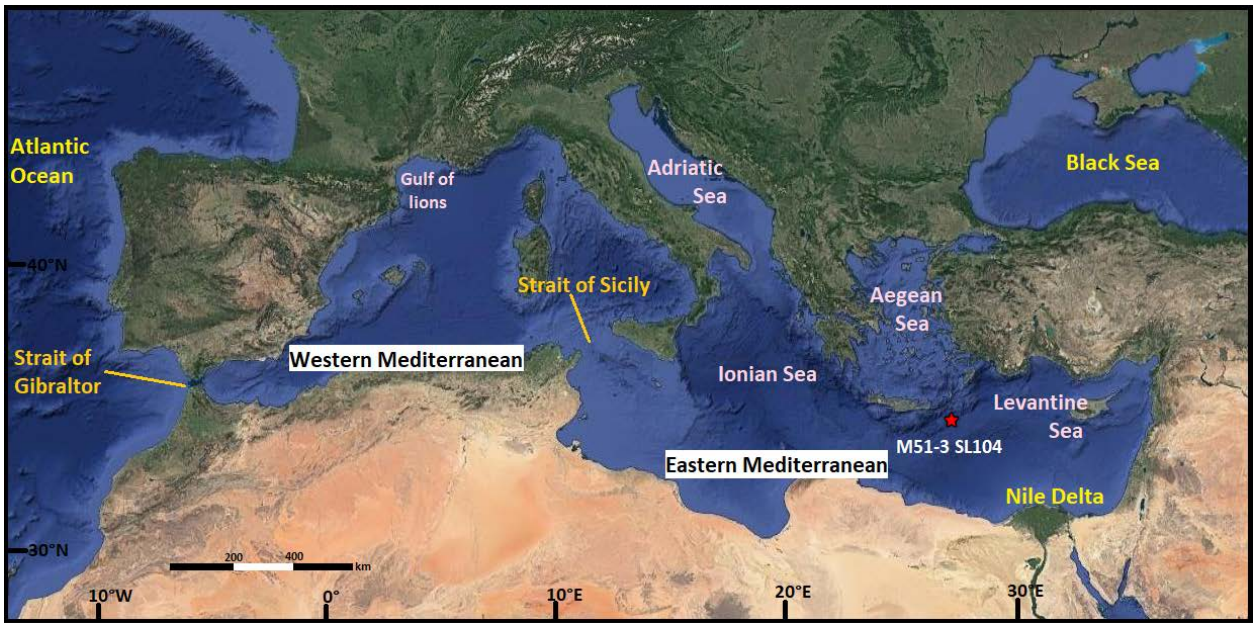

Figure 1: Map of the Mediterranean Sea- The location of the studied core M51-3-SL104 is indicated with red star. Modified from Google Earth satellite image.

The Mediterranean circulation has an anti-estuarine pattern where evaporation exceeds the precipitation and run-off, leaving more saline surface waters and leads to density-driven circulation. The saline water (salinity of 36.2 psu) from the Atlantic Ocean enters the western Mediterranean through the Strait of Gibraltar by mixing with the Mediterranean Intermediate Water, forming Modified Atlantic Waters. The salinity of the water keeps increasing as evaporation occurs as it flows further into the Eastern Mediterranean through Strait of Sicily ending up with a salinity of about 38.5 psu (Moller, 2012). As the temperature lowers during winter the highly saline surface water sinks

and forms Levantine Intermediate Water at 150-600 m depth at the Levantine region in the Eastern Mediterranean (Figure 1). The Levantine Intermediate Water then advances westward at that depth and joins the open Atlantic Ocean. It also mixes with less saline but colder deep water to form the Western and Eastern Mediterranean Deep Water at the Gulf of Lions, and Adriatic and the Aegean Sea respectively (Rohling et al., 2009). Due to this circulation pattern, the Eastern Mediterranean especially remains as a nutrient desert by the removal of nutrient-rich intermediate water to the open Atlantic.

The Mediterranean Sea circulation is influenced by several factors viz. intensity and variability in African monsoon, North Atlantic oscillation, change in orbital parameters and its effect on summer insolation and seasonal shifts, glacial-interglacial cycles and the mid-latitude climatic system. The seasonal shifts of Inter Tropical Convergence Zone (ITCZ) and hence the atmospheric cells with the westerlies and trade winds regulate the Mediterranean climate of dry summers and wet winters.

1.2 Sapropel formation

Sapropels are organic carbon-rich layers (usually with TOC > 2%) formed during anoxic conditions that tend to preserve sediments from diagenesis or degradation (van Santvoort et al., 1997). They are characterized by fine sub-mm scale lamination and are usually free of bioturbation.

The amount of insolation received by the Earth is generally modulated by its precession cycle along with changes in eccentricity and obliquity. During precessional minima, the Northern Hemisphere gets increased insolation during summer and reduced winter insolation. This leads to more seasonal contrast such that the ITCZ moves further north during the summer which intensifies the trade winds and as a consequence strengthens the North African monsoon system (Rossignol-Strick et al., 1982). This drastically increases the precipitation over the Mediterranean catchment areas and leads to the higher contribution of river discharge to warm, low salinity surface water leading to the formation of a stable stratified water column (Rohling et al., 2015). When there is stability in the water column, there is more buoyant and warmer water on the surface, and denser and cooler water at the bottom. This prevents convective overturning circulation to occur and hence leads to a lack of ventilation in the bottom waters

(Rossignol-Strick et al., 1982). Thus a condition of precessional minima favours the preservation of organic matter and formation of sapropel (Figure 2).

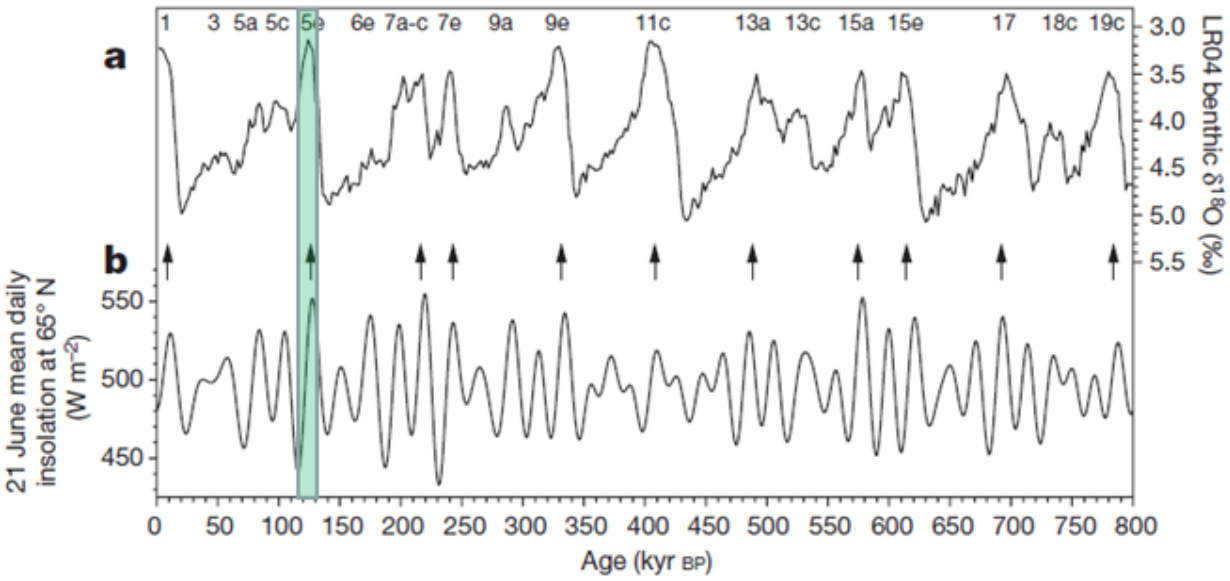

Figure 2: Marine isotope sub-stages and Insolation of past 800,000 years- (a) LR04 benthic $\delta^{18}O$ (b) Mean insolation at 65°N. The arrows correspond to insolation maxima and corresponding benthic $\delta^{18}O$ minima during which sapropel deposition occurred. The shaded region corresponds to MIS 5e and tentatively to the formation of sapropel S5 (Tzedakis et al., 2017).

When there is a freshwater influx from rivers to ocean due to increased precipitation, it leads to weakening of anti-estuarine circulation in the Mediterranean basins with the Atlantic Ocean. This weakening in circulation results in intermediate water to be formed at a shallower depth and along with the shoaling of the nutricline leads to bringing up of more nutrients from beneath to the photic zone. This is predicted to result in increased primary productivity and development of a deep chlorophyll maximum (Rohling and Gieskes, 1989). Altogether, sapropel formation essentially requires both enhanced productivity as well as anoxic conditions for its preservation.

1.3 The Eemian interglacial and Sapropel S5

The Marine Isotopic Stage 5 (MIS 5) contains sub-stage MIS 5e between 130- 116 ka called the Eemian interglacial or the Last Interglacial (Moller, 2012) (Figure 2). During the climatic optimum, at time of sapropel S5 formation, the average sea level was around 6 m higher, and a more humid and warmer temperature prevailed. The temperature was around 3°C than the present value was indicated by pollens of

thermophilic and temperate trees found profusely in the Eemian biostratigraphic unit (Moller, 2012). The S5 sapropel is known to range from 25– 120 cm depending upon its location and the spatial variability in organic carbon productivity (Rohling et al., 2015).

The $\delta^{18}O$ data suggest that during the last interglacial, the ITCZ penetration had reached far northward to around 21°N (Rohling et al., 2002) and the maximum penetration of monsoonal precipitation extends until 25°N (Toucanne et al., 2015). Hence the Mediterranean climate is realized to be under the influence of freshwater discharge from various rivers and wadi systems from its borderlands which is discussed in more detail in Section 1.4.1.2.

Around 3 kyr preceding the sapropel S5 formation, a step-wise reduction in deep-water ventilation was predicted due to gradual sea level rise (Grant et al., 2012). Followed by this, an abrupt onset of North African monsoon flooding observed from the sharp $\delta^{18}O$ shift to lighter values marks the onset of sapropel formation (Marino et al., 2007) (Figure 3B and C). As a result, a basin-wide decrease in deep-water ventilation occurred in the Eastern Mediterranean, but the development of seafloor anoxia is known to be varying depending on the depth and spatial variability of organic carbon export (Rohling et al., 2015). Moller, (2012) shows an instant development of sea-floor anoxia in the core SL104, seen as benthic azoic condition at the onset and throughout the sapropel, except for small re-population of these foraminifera in the bioturbated layers (Figure 3G).

Within ~650 years in the Aegean Sea (± 100 to 300 years in the open Mediterranean), a sudden advent of isorenieratene peak is observed, which are markers for populations of Chlorobiaceae (anaerobic green S- bacteria that requires sulphur and low light conditions). This indicates the development of euxinic conditions that expanded to the photic layer, to depths of 200 m or less. Around the same time, the $\delta^{18}O$ values also reach its lightest value along with the sea surface temperature (SST) increase (Marino et al., 2007) (Figure 3A).

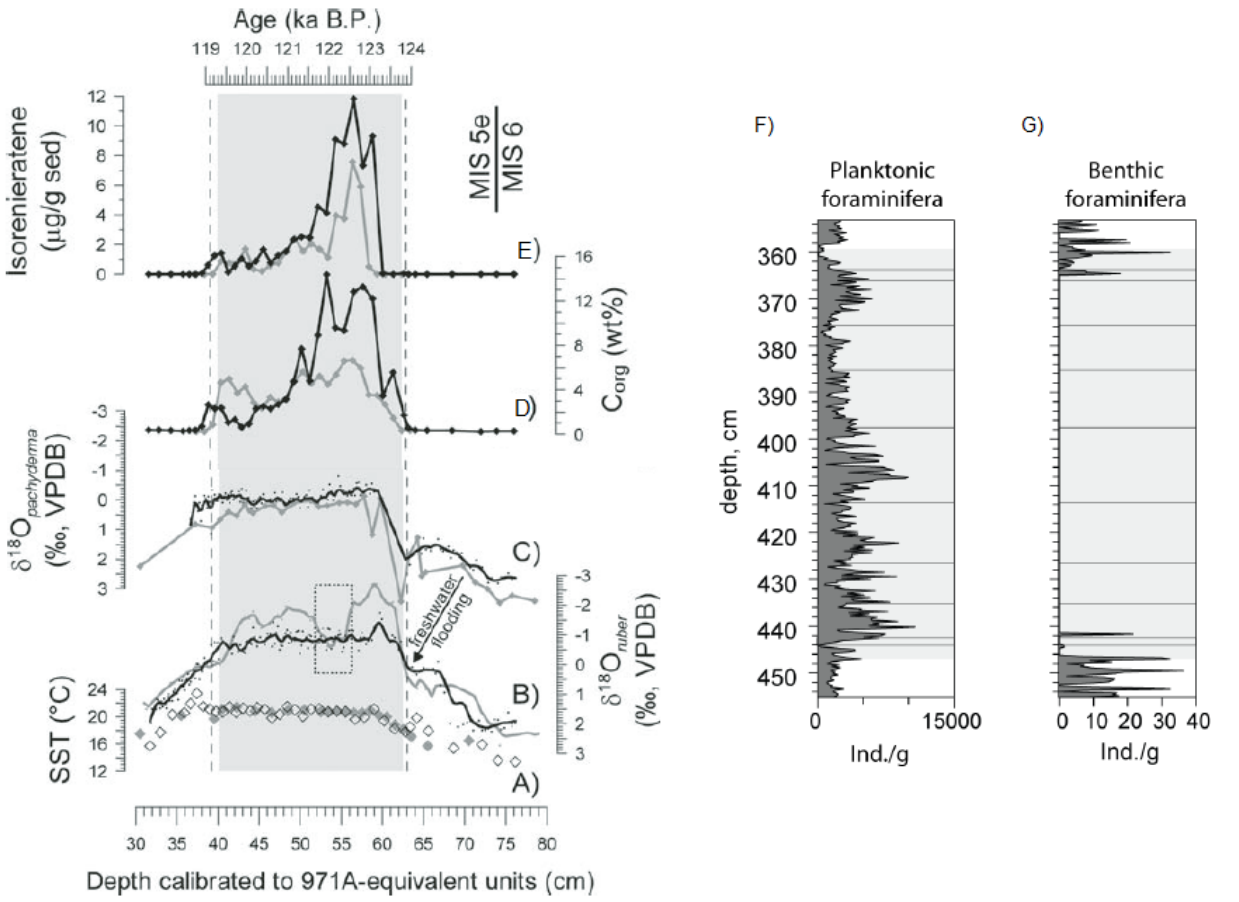

Figure 3: Foraminiferal oxygen isotopes and biomarker data A) SST from alkenone based paleothermometry, B) and C) $\delta^{18}O$ values from foraminifera D) C_{org} and E) isorenieratene concentration from core 971A (Levantine basin-gray) and LC21 (Aegean Sea-black) (Marino et al., 2007). F) and G) planktonic and benthic foraminifera per gram sediment from core SL104 (Moller, 2012). Shaded area corresponds to the sapropel region.

1.4 Study location and scope of the thesis

The sediment core under study, M51-3 SL104 is located in the Eastern Mediterranean Sea (EMS), south-east of Crete (Figure 1). The sapropel S5 in this core ranges from 359.5- 446.3 cm and is broadly characterized to contain two facies within. The bottom 9 cm of the sapropel constitutes the non- diatomic facies and the remaining sapropel towards the top shows diatomic facies characterized by clearly laminated sediments. The sedimentation rate varies from around 6 cm/kyr in the non- diatomic region to around 26 cm/kyr in the diatomic region.

The diatomic region contains fine sub-mm scale lamination (which can be observed as varves couplet) where the lighter lamina belongs to mass-sinking of mat-forming

diatoms like Rhizosolenid, *Hemiaulus hauckii*, *Thalassiotrix*, at the wake of winter (Kemp et al., 1999; Moller, 2012). They are known to bloom near the chemocline exploiting nutrients in the highly stratified water column in the summer (Kemp et al., 1999). Since they are capable of vertical migration within the water column they get a significant advantage compared to other non-specialized organisms incapable of migrating to a shallower nutricline for nutrients in summer. The darker lamina consists of a mixed assemblage of diatoms (like *Thalassionema* species) and terrigenous inputs (Kemp et al., 1999; Moller, 2012; Kemp and Villareal, 2013).

In addition to the lamination, on a larger area, mm to cm scale layering can be observed based on its colour and predominant laminae constituting them. Hence within the sapropel, the darker layers denote pluvial periods and lighter ones correspond to comparatively drier periods.

Wu et al. (2018) describes the various sources of freshwater input coming into the Eastern Mediterranean by analyzing the Sr and Nd isotopes and major and rare earth elements. Depending on the location of the sediment core at the south-east of Crete, the major fluvial contributions are made by Aegean riverine inputs and Nile discharge during sapropel S5 deposition. Detrital input from Saharan also has some contribution.

1.4.1 Elemental proxies

1.4.1.1 Paleoproductivity indicators

Barite ($BaSO_4$) precipitation occurs in sediments associated with decaying organic matter and is widely used in inferring surface water productivity. Consequently, the variation in biogenic Ba content within the sapropel is indicative of total organic carbon, and enrichment in the sapropel layers is demonstrated (Weldeab et al., 2003).

Bromine, which is also a good indicator of marine productivity and correlated to marine organic carbon content shows enrichment in these sapropelic layers (Ziegler et al., 2008). Though the nature of the association between Br and organic matter is still debated, the synthesis of several brominated organic compounds has been identified to be of marine origin. Since diatoms are abundant in the studied sediment core biogenic silica contribution is also predicted to be high.

1.4.1.2 Terrestrial input proxies

Recent studies from Wu et al. (2018) with the isotopic signature from LREE/HREE (light to heavy rare earth element ratio), a mafic provenance is established for the river-borne sediments at the site of the studied core. The Northern Borderland of Eastern Mediterranean (NBEM) is known to be a contributor of illite and chlorite, and K and Mg. Kaolinite comes in from Southern Borderlands, from the Sahara and has high Ti and Zr contribution from rutile/ sphene and zircon minerals respectively (Figure 4). Significant amount of Nile-derived Ti is also noted in the south-eastern Mediterranean. Hence, detrital K input versus Ti along with the clay mineral ratios might help in discerning the intricate mixture of the Nile and NBEM contribution into the studied site.

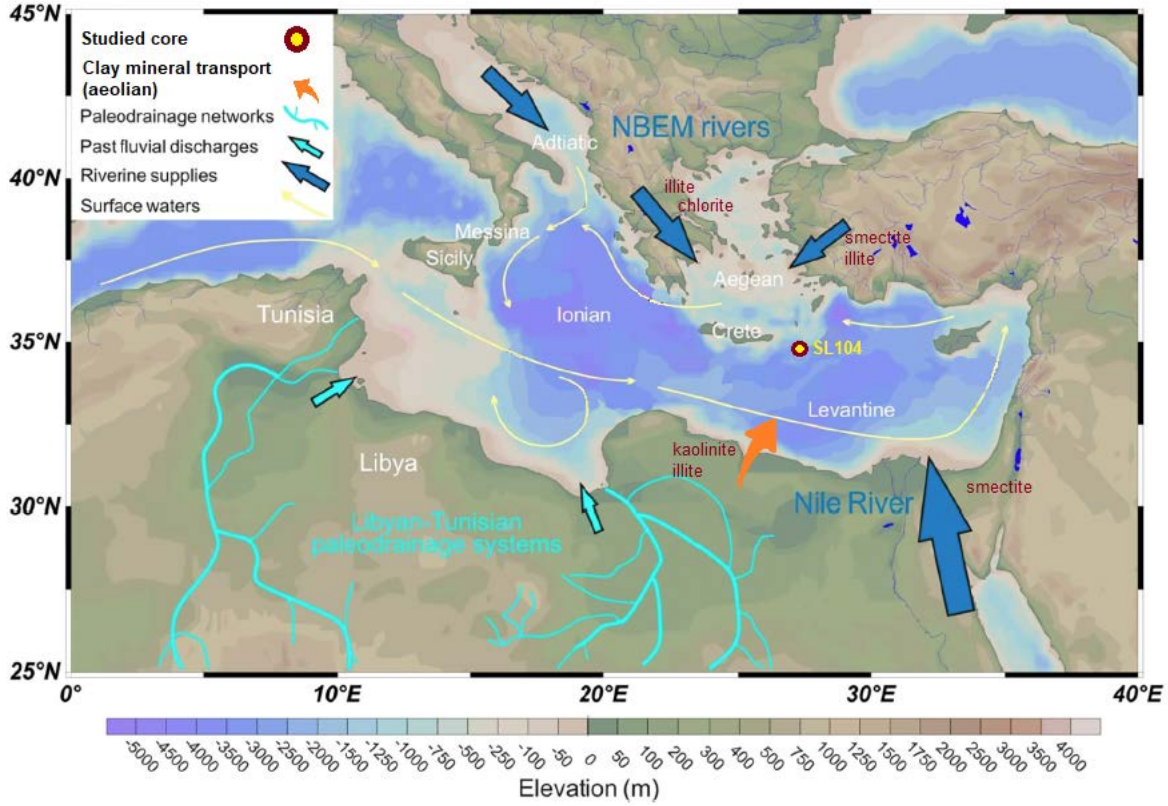

Figure 4: Detrital sediment provenance and mineral inputs to the site of the studied core. Modified after Wu et al. (2018)

1.4.1.3 Elements indicating post-depositional oxidation

Towards the end of the sapropel deposition, bottom water re-oxygenation occurs and leads to oxidation of Mn^{2+} in the sediment pore waters to MnO_2. This can be observed as a significant peak along with the peak of trace element Cu, as observed at the end of

the sapropel S1 indicating post-depositional oxidation front (Thomson et al., 2006). However, the mechanism behind this chalcophile precipitation still remains elusive. Hence Mn/Ti and Cu/Ti help in identifying the oxic front and the end of the sapropel deposition.

1.4.2 Lipid biomarkers as paleoenvironmental proxies

Lipid biomarkers serve as paleoenvironmental proxies by preserving their molecular structures which are modulated based on the environmental conditions in which they form. Thus, studying the variation in abundances of different biomarkers at different times helps in decoding the past environmental conditions that they reflect. Multiple molecules and proxies have been used in this study, as listed below (Figure 5) to have a multifaceted approach in unravelling the issue in hand.

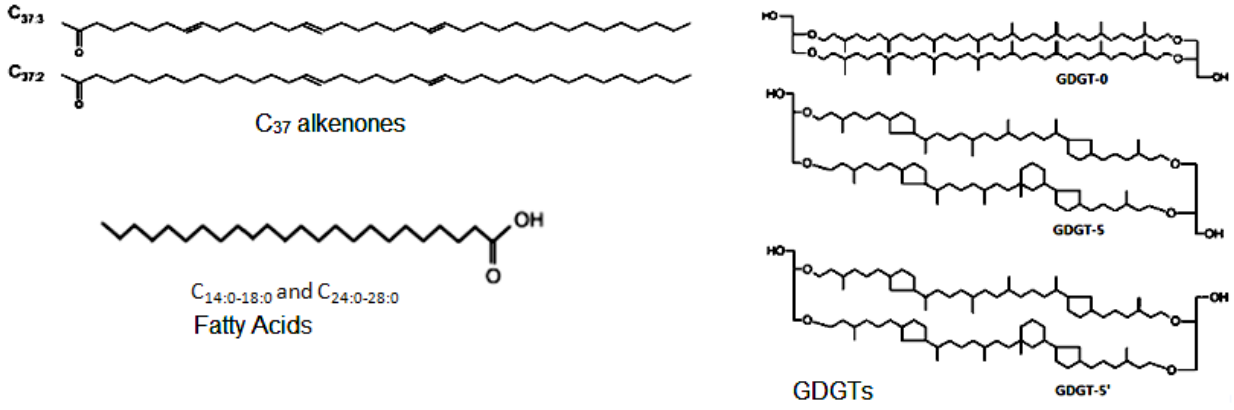

Figure 5: Biomarkers as paleoenvironmental proxies- alkenones, GDGTs and fatty acids

Glycerol dialkyl glycerol tetraethers (GDGTs)- are mainly produced by few phyla of archaea like *Thaumarchaeota* and *Euryarchaeota.* Depending on the degree of cyclization in these molecules, various proxies have been created like TEX_{86} (Tetraether index of tetraethers consisting of 86 carbon atoms; Schouten et al., 2002) and CCaT (crenarchaeol–caldarchaeol tetraether index; Wörmer et al., 2014), which are mainly used in constructing Sea Surface temperature (SST). Recent findings suggest that factors other than temperature are also likely to regulate the GDGT composition under different environmental conditions (Qin et al., 2015; Evans et al., 2018). Factors like ammonium and oxygen limitation might also play a significant role in defining the extent of cyclization and abundance in the natural setting.

Alkenones- are synthesized by phytoplankton species of the class Prymnesiophyceae. These organisms tend to respond to changes in ambient temperature by varying the degree of unsaturation of alkenones (Müller et al., 1998). Thus $U^{k'}_{37}$ (Unsaturation index of C_{37} alkenones) remains to be used as a robust SST proxy.

Fatty acids- originate from various organisms ranging from bacteria to higher plant. They serve as important indicators of their sources and ecological conditions in which they are generated. Short chain fatty acids $C_{14:0\text{-}18:0}$ are produced predominantly by bacteria, diatoms, green algae and prymnesiophytes indicative of their marine autochthonous origin (Volkman et al., 2003), whereas long-chain fatty acids ($C_{24:0\text{-}28:0}$) comes from the terrestrial source from various vascular plants. The average chain length (ACL) of long-chain fatty are known to show vegetational changes between C_3 and C_4 plants and the humid or drier environmental condition in which they form respectively (Hughen et al., 2004).

1.5 Objectives

Studies done so far related to sapropel S5 formation and reconstruction of the variability in the Eemian interglacial have mainly used isotopic analysis on micropaleontological proxies and palynology at coarse resolution. The main goal of this study is to generate ultra-high resolution molecular stratigraphic records of the Mediterranean Sapropel S5 on annual to decadal time scales using Mass Spectrometry Imaging (MSI) technique to shed light on climatic changes that occurred during sapropel formation. The biomarker analysis utilizes Laser Desorption Ionization Coupled Fourier Transform – Ion Cyclotron Resonance – Mass Spectrometer (LDI FT-ICR-MS). In order to validate the high resolution MSI results, conventional analytical tools like Gas Chromatography/ Mass Spectrometry (GC/MS) and High-Performance Liquid Chromatography/ Mass Spectrometry (HPLC/MS) were used.

Objective 1: To evaluate the relation between paleoecological (vegetational) and paleoclimatic changes during the climatic optimum in the Last Interglacial. The results would serve as a model for climate variability during the most recent period that was warmer than modern and will enable comparisons to Holocene in future studies.

Elemental profiles at high resolution using micro- X-ray fluorescence (μ-XRF) will supplement the molecular-level results and provide a view of additional factors shaping the paleoclimate.

Objective 2: To analyze the high-resolution data generated (for a time period spanning 4.8 kyrs) for cyclicity patterns that can be attributed to annual-decadal oscillations, and to infer their relationship to various climatic processes and ocean circulation on a global scale.

2. MATERIALS AND METHODS

2.1 Sediment core

The studied sediment core SL104 was obtained from the University of Tübingen, Germany in a collaboration with Dr. Michal Kucera and Dr. Hartmut Schulz. The core was initially collected from the Eastern Mediterranean during marine expedition METEOR M51/3 La Valetta – Istanbul onboard research vessel RV METEOR. The core (location 34.8247°N, 27.2925°E) was obtained from a water depth of 2155 m from a part of the Pliny Trench, south-east of Crete (Figure 6) (*METEOR -Berichte 03-1 Ostatlantik-Mittelmeer-Schwarzes Meer*, 2003)

2.2 Age model

The core age model (121.7-126.4 kya ~4.8 kyr) is based on Moller, (2012). The sapropel S5 spans around 86.8 cm ranging from 359.5- 446.3 cm. The non-sapropel marl at the base or during the early phases before the sapropel deposition set in (till 126.37 kya) has a sedimentation rate of 4.8 cm/kyr. Following that, 10.6 cm corresponding to the non-diatomic sapropel (126.37- 124.55 kyr) has a sedimentation rate of 5.8 cm/kyr. High sedimentation rate of 26 cm/kyr is present throughout the diatomic facies in the sapropel till 121.66 kyr (or 359.5 cm) except for 0.9 cm region in between (414.4- 413.5 cm depth), having a sedimentation rate of 450 cm/kyr (123.736 - 123.734 kyr).

Since the sapropel was highly porous due to the abundance of diatomic frustules in them, they naturally tend to expand a bit during sample handling and storage. This may have lead to around 1.8 cm expansion in length for the studied sediment core which

was taken into account by applying a linear scaling of the length to get a refined age model.

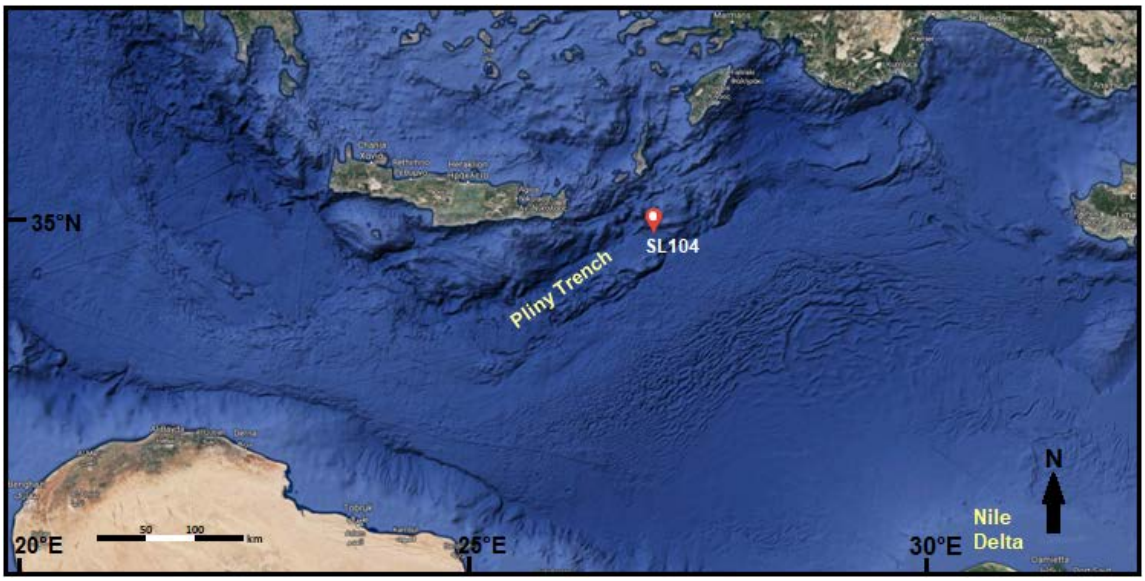

Figure 6: Sediment location in Pliny Trench. Modified from Google Earth satellite image.

2.3 Sample preparation technique for elemental and biomarker analysis

The protocol used for sample preparation was based on Alfken et al. (2019) (Figure 7).

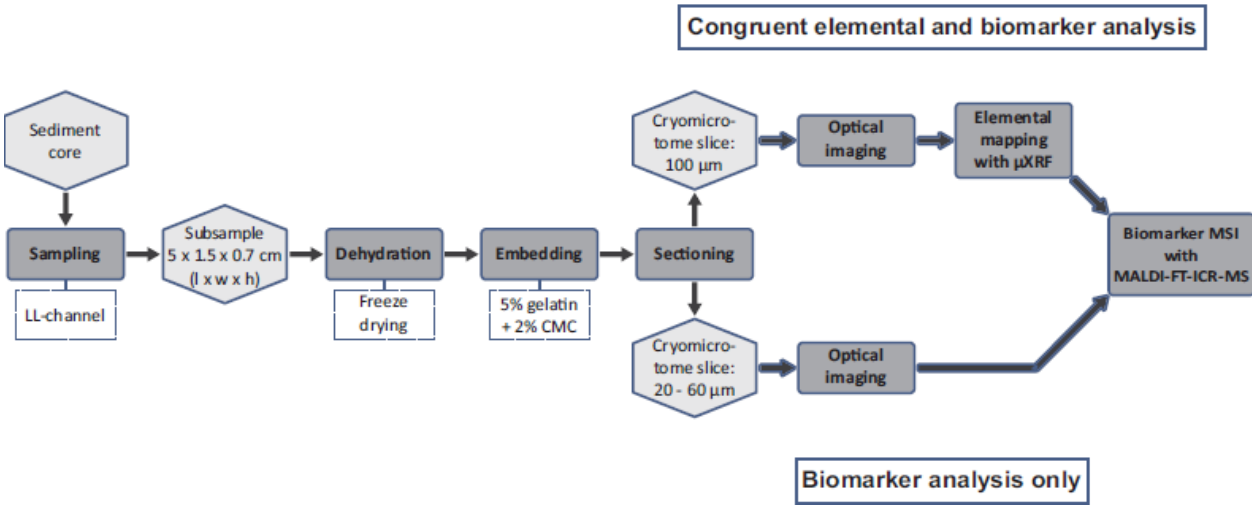

Figure 7: Overview of the sample preparation protocol for elemental and biomarker analysis. From Alfken et al. (2019)

One metre length of the sediment core SL104 consisting the sapropel was sampled with four double L-channels of width 1.5 cm, height 0.7 cm, and length of 25 cm each.

Following this, digital imaging of all the four sections was performed with a GEOSCAN colour line scan camera on Multi-Sensor Core Logger to obtain discrete measurements of colour (red, green, blue) and lightness (% values) at a resolution of 1 mm. In order to visualize the fine-scale lamina in detail, X-ray radiograph of the 25 cm sample sections were obtained with a Faxitron 43855A X-ray cabinet at 45 kV, 3 mA and 7 min exposure time in AGFA Strukturix D4 FW film.

Sub-sampling of each 25 cm sediment section into smaller 5 cm sections were done. The sub-sections were freeze-dried in an ALPHA 1-4 LD freeze dryer to ensure that the wet sediment section is dry as well as intact prior to further analysis using micro-X-Ray Fluorescence system (µ-XRF). A gelatin + CMC (sodium carboxymethyl cellulose) mixture in 5% + 1% was used as an embedding medium, dissolved in Milli-Q maintained at a temperature below 80°C for the sediment sub-sections. After embedding, 60µm thin slices were obtained using a cryomicrotome (Microm HM 505 E Cryostat, GMI) maintained around -17 °C and fixed to indium-tinoxide-coated (ITO) slides from Bruker Daltonik (See Figure 8).

2.4 Elemental mapping using micro-X-Ray Fluorescence system

The variation in elemental composition within the sediment can be analyzed through known elemental proxies (and their ratios like Si/Ti, Br/Ti, Ca/Ti etc.) and helps us to infer about various environmental and climate changes. Non-destructive elemental analyses of the sediment sections were done using a Bruker M4 Tornado µ-XRF system with Rh source at 50 kV, 600 µA. Measurements were taken under vacuum at 20 mbar pressure with 3 ms/pix for 3 cycles at a high resolution of 50 µm on the intact, freeze-dried sub-samples of 5 cm. The spatial distribution of the elements were also obtained and mapped onto the high-resolution Video Image taken (Figure 9). Analysis of the data was done on Bruker M4 Tornado Software 1.3 and MATLAB scripts were used to remove the outliers and generate downcore elemental profiles.

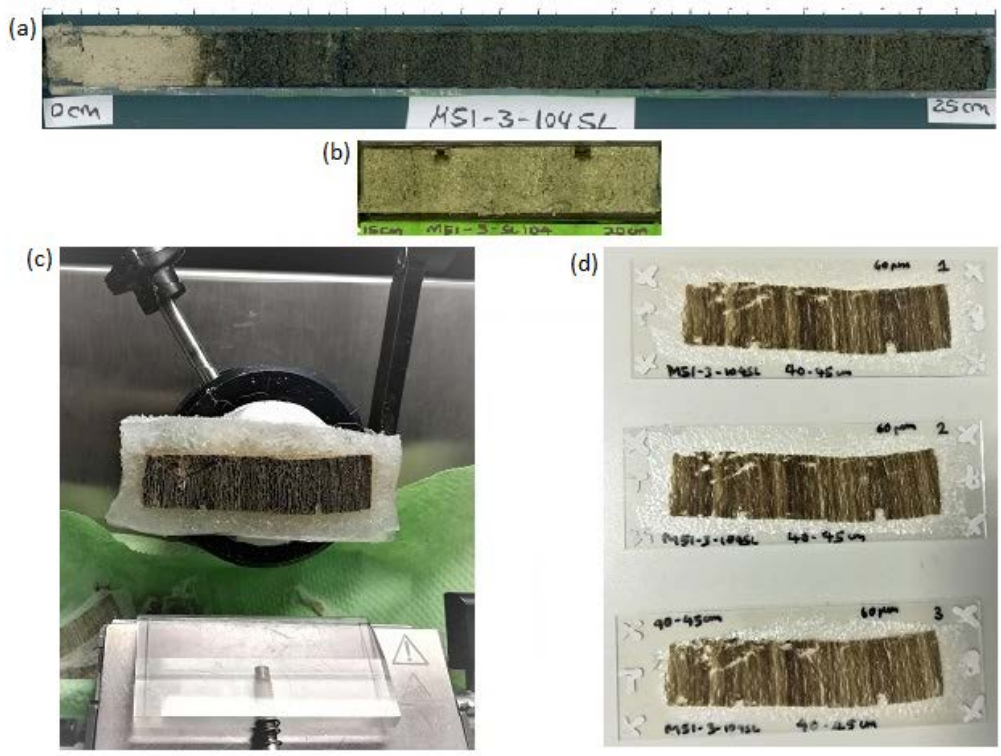

Figure 8: Sample preparation images- (a) Double L-channel sampled 25 cm section (b) freeze dried 5 cm sub-section (c) Embedded sample in cryomicrotome (d) Thin slices in ITO slides for FT-ICR-MS measurements

2.5 Mass Spectrometry Imaging

Laser Desorption ionization coupled Fourier Transform-Ion Cyclotron Resonance-Mass Spectrometry (LDI coupled FT-ICR-MS) was used to generate spatial distribution maps by MSI and downcore profiles of lipid biomarkers like GDGTs, alkenones and fatty acids (Figure 9).

It works on the basis of determining the m/z ratio of ions based on their cyclotron frequency in a fixed magnetic field. After collision induced ionization of the ions, they are injected inside an ion trap and is excited and detected by the detection plates in the cell. They are converted to a frequency spectrum with a Fourier transform which is then converted to a mass spectrum. A 7T solariX FT-ICR-MS with 1 kHz Smartbeam II laser (Bruker Daltoniks) was used in different Continuous Accumulation Of Selected Ions (CASI) windows, particular to different classes of biomarkers in hand (Table 1) to enhance sensitivity by separating the target ions from their background. Similar to that, MultiCASI with two CASI windows were set to obtain targeted fatty acids from both

windows simultaneously. Various parameters from Laser power (LP), Laser shots (LS), Laser frequency (LF) and Large Laser focus were also specifically selected.

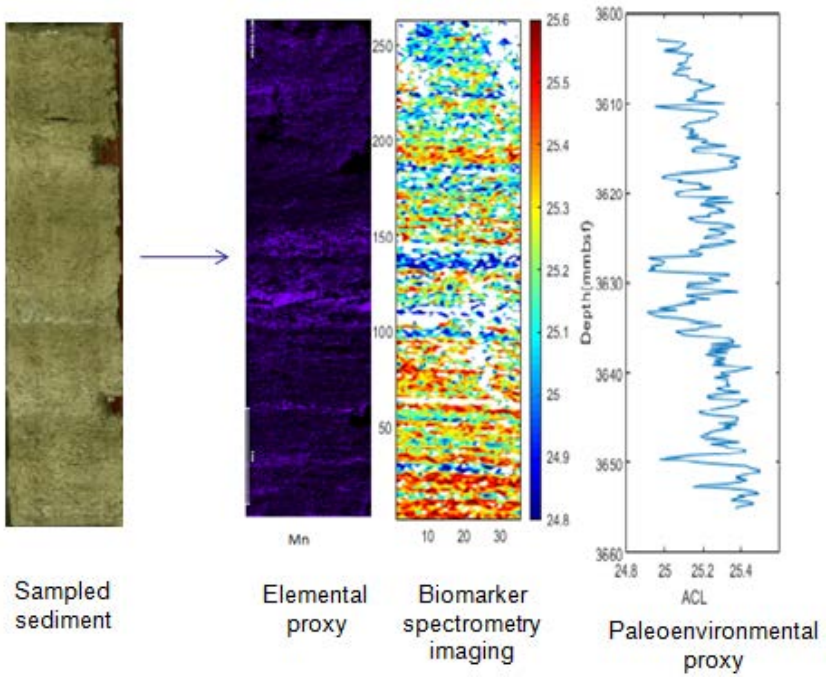

Figure 9: Elemental mapping and biomarker spectrometry imaging-5cm sample section showing elemental profile of Mn from the µ-XRF; MSI of fatty acid biomarker generated from FT-ICR-MS data; the downcore profile of ACL proxy calculated (from left to right).

Biomarkers	Method (mode, size)	CASI window (isolation m/z, isolation width)	Time of flight (ms)	Collision Voltage (V)	MALDI Parameters
GDGTs	Positive, 600-2000 m/z, 256k	1320, 20	1.6	-10	LP 65% LS 700 LF 1000 Hz
Alkenones	Positive, 300-2000 m/z, 512k	554, 12	0.8	-5	LP 60% LS 500/700 LF 1000 Hz
Fatty acids	Positive, 150-1000 m/z, 512k	Multi CASI 280, 65 420, 65	0.6	-5	LP 60-70% LS 500/700 LF 1000 Hz
	Positive, 150-2000 m/z, 1M	420, 70	0.8	-5	LP 55% LS 500 LF 1000 Hz

Table 1: Parameters defined for FT-ICR-MS measurements

On an average, ~13000 spectra were obtained for each 5 cm sub-samples with a resolution of 200 µm. A data reduction of 50% was done for storage in the ftms Control 2.1.0 (Bruker Daltonik). The data obtained were calibrated with specific calibrants

(Pyropheophorbide-A, GDGT-5, $C_{16:0}$ and $C_{24:0}$ fatty acids- see Table 2) defined within the isolation window in Bruker Data Analysis 4.4. The mass spectra in the region of interest were also exported from Data Analysis 4.4. Subsequently, MATLAB scripts were used to generate heat maps superposed on X-ray radiograph. Multiple data points in the same horizon obtained from the MSI were averaged and transformed into a single data point to obtain a down-core profile as shown in Figure 9 (Alfken et al., 2019). Data points were only generated for a minimum of 10 spots per horizon. The formulas used of the calculating proxies are summarized in Table 3. Additional MATLAB scripts were used to generate time series plot for the whole sapropel (by associating specific depth to fixed time) by using the age model as discussed in section 2.2.

Biomarkers	**CASI window (isolation m/z, isolation width)**	**Calibrants**	**Calibrant window (± mDa)**	**Signal to Noise ratio**
GDGTs	1320, 20	Pyropheophorbide-A	7-10	1
Alkenones	554, 12	GDGT-5	3-7	0.7
Fatty acids	Multi CASI 280, 65 420, 65	$C_{16:0}$ and $C_{24:0}$ fatty acids	5-6	0.3
	420, 70			

Table 2: Calibration of biomarkers and signal/noise given

Biomarker	**Proxy calculations**	**Reference**
GDGTs	CCaT=GDGT-5/(GDGT-5+GDGT-0) SST= 54.428 –(21.916/CCaT)	Modified after Wörmer et al. (2014) by Nina Rohlfs (unpublished data)
Alkenones ($C_{37:2}$ and $C_{37:3}$)	$U^{k'}_{37}=C_{37:2}$ /($C_{37:2}$+ $C_{37:3}$) SST=($U^{k'}_{37}$-0.043)/0.033	Müller et al. (1998)
Fatty acids ($C_{24/26/28}$ or $C_{14/16/18}$ indicates long and short fatty acids)	ACL= (24* $C_{24:0}$ + 26* $C_{26:0}$ + 28* $C_{28:0}$) / ($C_{24:0}$ + $C_{26:0}$ + $C_{28:0}$)	Poynter et al. (1989)
	TARFA= ($C_{24:0}$ + $C_{26:0}$ + $C_{28:0}$) / ($C_{14:0}$ + $C_{16:0}$ + $C_{18:0}$)	Meyers, (1997)

Table 3: Key formulas of the proxies used in the study

2.6 Spectral, Wavelet and Phase Analysis of Time-Series

The combined data of the biomarker proxy and its respective age obtained from the age model was initially linearly interpolated and then de-trended with R-scripts (all the used scripts are attached in the appendix). Several toolkits were then utilized for spectral analysis. A Multi-taper method (MTM) which reduces the variance of spectral estimates by multiplying the data by orthogonal tapers was computed to get spectral density estimation (Percival and Walden, 1993). It decreases the spectral leakage or out-of-band bias outside a frequency with half the bandwidth.

Additionally, wavelet analysis (Figure 10) was carried out where a Fourier transformation was done by using infinite and cyclic nature of the time series. This helps to analyze the changes in the time-frequency domain (H. Trauth, 2015).

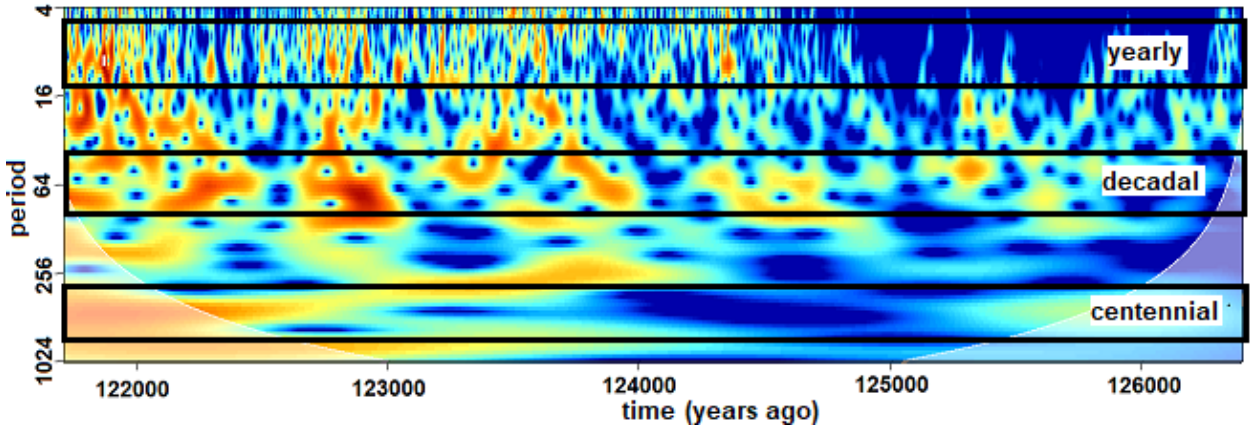

Figure 10: Model wavelet analysis plot showing yearly, decadal and centennial scale variability signals

Phase analysis was done by applying a bandpass filter for signals categorized into the range of yearly (7-14 years), decadal (50-70 years) and centennial (400-800 years) scales (See Figure 10). The script involves Cross Spectrum analysis where a Fast Fourier Transform was done to obtain the magnitude of coherence, cross-spectral phase value and frequency of the signal. The coherence of the data under comparison was obtained from this bandpass filtering and is indicated by concentric circles (ranging from 0 to 1) in the phase analysis chart (Figure 11). Phase relations between model sinusoidal waves are depicted in Figure 11, in polar coordinates with respect to its quadrants in the circular chart.

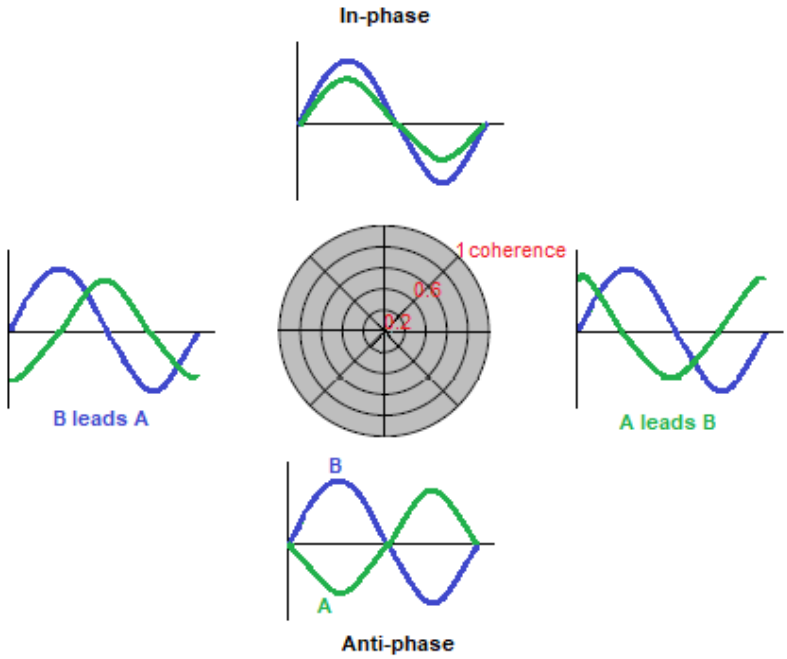

Figure 11: Phase analysis chart showing coherence and phase relations between sinusoidal waves B versus A

2.7 Conventional approach to biomarker analysis

Conventional GC/MS and HPLC/APCI-MS measurements were done to correlate biomarker data with the FT-ICR-MS measurements which would serve as its proof of concept as well. First, a broad-scale correlation for the whole ~90 cm sapropel section was done by sampling at 10 cm intervals. Further, measurements with a high resolution of 0.5 cm sampling interval for a chosen 5 cm sub-section (depth 3994 to 4044 mm) were also done. Three additional samples from the middle (in between 50-55cm sample range or 4045-4075mm depth range- See Table A1) were also obtained when re-sampling of the sections of sample range 50-55 cm and 60-65 cm were done, due to handling issue while embedding these sample sections. Hence a total of 23 samples were used for conventional measurements.

Extraction of sediment samples for the GC and LC measurements were done with Bligh and Dyer technique (Bligh and Dyer, 1959). Around 0.1- 0.8 g of sediment was freeze-dried and extracted in dichloromethane, methanol and phosphate buffer in 1:2:0.8 ratio, in v:v mixture by ultrasonication. 5 µg each of GC and LC standards, GC standard mix (2-Methyloctadecanoic acid, 1-Nonadecanol, Behemic acid Methylester, Cholestane)

and C21 Phosphocholine respectively were added to each sample. Two iterations each of phosphate buffer and trichloroacetic acid buffer were done. Following this, the organic and aqueous phases were separated with dichloromethane and MilliQ respectively in 3 cycles. The organic phase collected as total lipid extract (TLE) was evaporated under nitrogen gas in the TurboVap II and stored. See Table A1 in the appendix for more details.

Derivatization of fatty acids from the lipid extract was required for better separation in GC. For this, silylation of the hydroxyl group by replacing trimethylsilylether group to it was done for 8% TLE in 50 µl bis(trimethylsilyl)trifluoroacetamide (BSTFA) and 100 µl pyridine catalyst and incubated at 70°C for 1.5 hours modified from the method described by (Knapp, 1980)

2.7.1 Gas Chromatography/ Mass Spectrometry (GC/MS)

All the 23 samples were initially measured in Thermo Finnigan Trace GC-FID (flame ionization detector) equipped with Restek Rxi-5ms capillary column (30 m × 0.25 mm ID) for alkenones. Thereafter derivatized samples from TLE were used to detect fatty acids in the GC-FID. An AS3000 autosampler was used for 1 µl sample injection in splitless mode. This was used for the purpose of quantification of different biomarkers in the samples. For qualitative confirmation of the signals measured in GC-FID, Thermo Quest Trace MS analysis was done for 3 samples with similar AS3000 autosampler. Helium at a constant flow rate of 1 mL/min was used as a carrier gas. The GC was set to an initial temperature of 60°C and held for one minute, then heated to 150°C at a rate of 10°C/min, and then to 310°C at 4°C/min and held for 20 minutes.

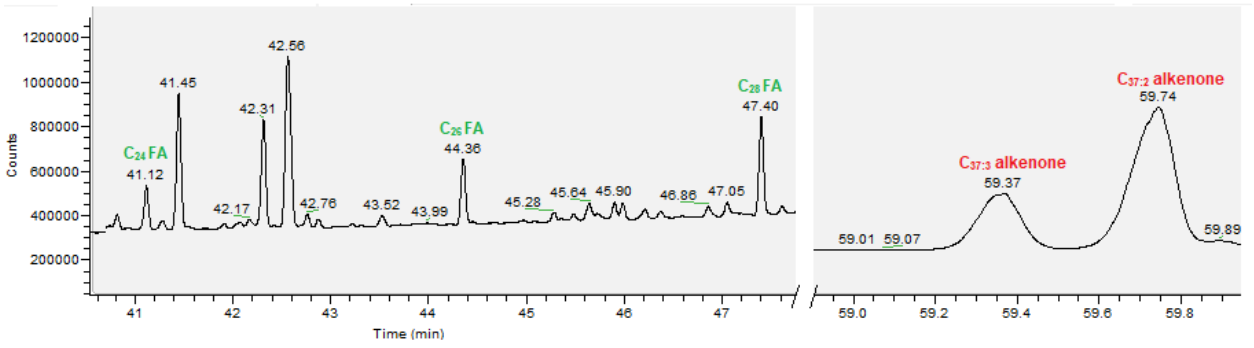

Figure 12: GC Chromatograms for $C_{24:0-28:0}$ fatty acids and $C_{37:2}$ and $C_{37:3}$ alkenones

Analysis following the GC/MS measurements was done on Thermo X-Calibur 3.1.66.10 2015, Thermo Fisher Scientific, Qual-browser, where retention times for specific compounds were identified from the MS spectra and the area under the curve was integrated by filtering area and peak noise factor (Figure 12).

2.7.2 High Performance Liquid Chromatography/ Atmospheric Pressure Chemical Ionization-Mass Spectrometry (HPLC/APCI-MS)

Since GDGTs are non-volatile high molecular weight compounds detection with GC is not feasible. Hence HPLC/APCI-MS from the method described in Becker et al. (2015) was used for this purpose. Measurements were done on Dionex Ultimate 3000 RSLC UHPLC instrument coupled to Bruker maXis Ultra-High resolution quadrupole time-of-flight mass spectrometry. 10 µl of TLE sample dissolved in hexane:isopropanol (99.5:0.5, v:v) with additional 1-2 ng of LC standard (C_{46}GTGT), was injected into two HILIC columns connected in series and maintained at 50°C. A solvent gradient of hexane (solvent A) and hexane:isopropanol (90:10, v:v) (solvent B) was used starting with 97% of A and 3% of B at a constant flow rate of 0.5 ml/min and increasing B thereafter. Bruker Compass Data Analysis 4.4 was used for identifying and quantifying the GDGTs by area integration (Figure 13).

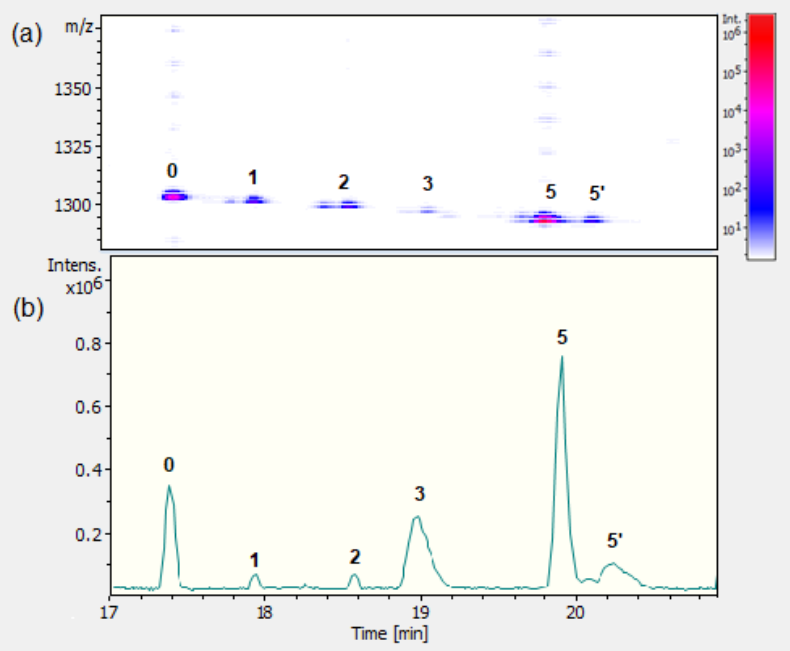

Figure 13: GDGT's peak identification from HPLC data- (a) Density map and (b) Base position chromatogram of GDGTs (0 to 5 and 5')

2.8 Principal component analysis

Principal component analysis (PCA) is a method of reducing the numerous variables into new orthogonal variables and visualizing variability and correlations between them. Each new component which accounts for as much of the variance in the data is generated by a linear combination of the given variables (Jolliffe, 2005). The analysis was done using PAST PAleontological STatistics, Version 3.22.

All the variables used for the analysis (all elemental and biomarker proxies) were first standardized using their respective mean and standard deviation so that the analysis isn't skewed towards variables with higher values. The standardization ensures each principal component (PC) will have mean 0 and standard deviation defined by the square root of their eigenvalues. The data set was grouped and colour-coded on the basis of changing characteristics of the sediment sample and inferences were drawn on the basis of their clustering. The PCA was done with correlation matrix since the variable where of different scales. Significant principal components were identified from Scree plot, showing the percentage of variation accounted for by each PCs. The scatter plot of the data points with vectors of corresponding variable indicates the strength to which each variable influence a PC. Further, correlations between the variables were analyzed with their respective loading scores to each component.

2.9 High-resolution zoomed-in video for biomarker proxies

In order to visualize the high-resolution data generated, a zoomed-in plot of each 5 cm sub-sections were made and concatenated to form a series using a python script. A window that runs at 120 pix/sec was set-up to make a video of approximately 2 min. A DVD attached with the Thesis contains the Video for the proxies.

With the sedimentation rate of ~26 cm/kyr from top of sapropel to ~435.7 cm, each 1 mm corresponds to around 3.76 years. From ~435.7 cm till the bottom of the sapropel, the sedimentation rate was ~6 cm/kyr, hence each millimeter corresponds to around 16.6 years.

3. RESULTS AND DISCUSSION

3.1 Elemental mapping

Since it is vital to understand the geochemical setting in which the sapropel was formed, a detailed study on the elemental composition of the sediment core is essential.

3.1.1 Paleoproductivity indicators

Main elements used for studying paleoproductivity during sapropel formation were Br, indicating marine organic carbon (MOC), Si/Ti and Ca/Ti denoting contributions from biogenic silica and carbonate production respectively.

From the general trend observed for Br values it can be inferred that there is a slight increase in productivity right from the beginning of the sapropel formation (Figure 14). Following this, a gradual increasing trend is observed in the non-diatomic region and consistent high values in the rest of the sapropel. This affirms the hypothesis of increased organic carbon export during the times of sapropel deposition.

Comparing the µ-XRF Br counts per second (cps) values with normalized Br/Cl ratios from Moller (2012), it is observed that the normalization hasn't made any significant change in its pattern (Figure 14). Ziegler et al. (2008) also mentions a technique of normalizing Br with Ti to infer about relative input of sedimentary components. Taking these together it suggests that the Br in the studied sediment core is a primary (autochthonous) signal of marine organic matter and contribution of allochthonous bromine origin is meager.

Rohling et al. (2015) have shown that it requires around 500-600 years for sea-floor anoxia to expand throughout the sapropel. But the immediate onset of sea-floor anoxia is observed in the open Mediterranean and the Aegean Sea. This might be possible from the mass sinking of mat-forming diatoms creating an anoxic blanket that covers the seafloor in areas of high export productivity (Kemp et al., 1999; Struck et al., 2002; Casford et al., 2003).

Si normalized to Ti acts as a proxy for biogenic silica mainly from diatoms (Agnihotri et al., 2008). It shows an increase at the onset of sapropel deposition followed by a steep rise around 125 kya (Figure 15) and shows significantly higher values in diatomic facies

(where the major contribution from mat-forming diatoms started) as expected. Moller (2012) study shows the presence of some diatomic frustules observed even in non-diatomic facies, showing signs of dissolution but no lamination from the mat-forming diatoms. This can be attributed to the increase in diatom productivity during the initial stages of sapropel formation where they underwent severe dissolution and reached a level of saturation of silica in the bottom waters (Moller, 2012). Following this, the increased Si values were observed and transition to diatomic facies occurred. A deep chlorophyll maximum might have developed around 125.8 kya (see section 3.2.1) that enabled the special vertically moving mat-forming diatoms to exploit the nutrients from the chemocline in the strong stratified water column giving them a significant advantage over other organisms. Hence distinct laminations of these mat-forming diatoms indicating seasonal changes were deposited and preserved.

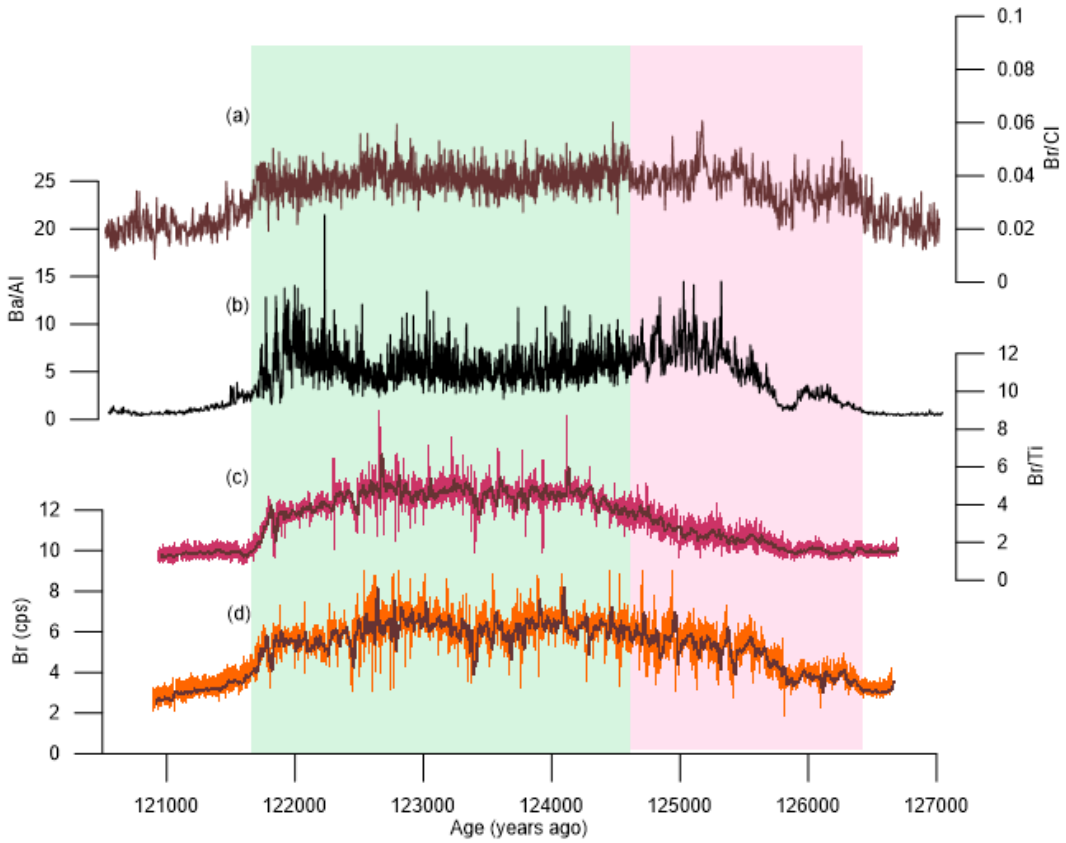

Figure 14: Elemental indicators of paleoproductivity- (a) Br/Cl ratio and (b) Ba/Al ratio (Moller, 2012). (c) Br normalized to Ti (d) Br profile with 50 points moving average. The whole shaded region represents the extent of sapropel, with pink region being non-diatomic facies and green shaded region corresponds to diatomic facies of the sapropel.

Ca/Ti shows a fluctuating trend throughout the sapropel (Figure 15) and is difficult to interpret. The decreased values within the diatomic facies might not necessarily indicate decreased biogenic carbonate production, but dilution from the increased silica content during those times.

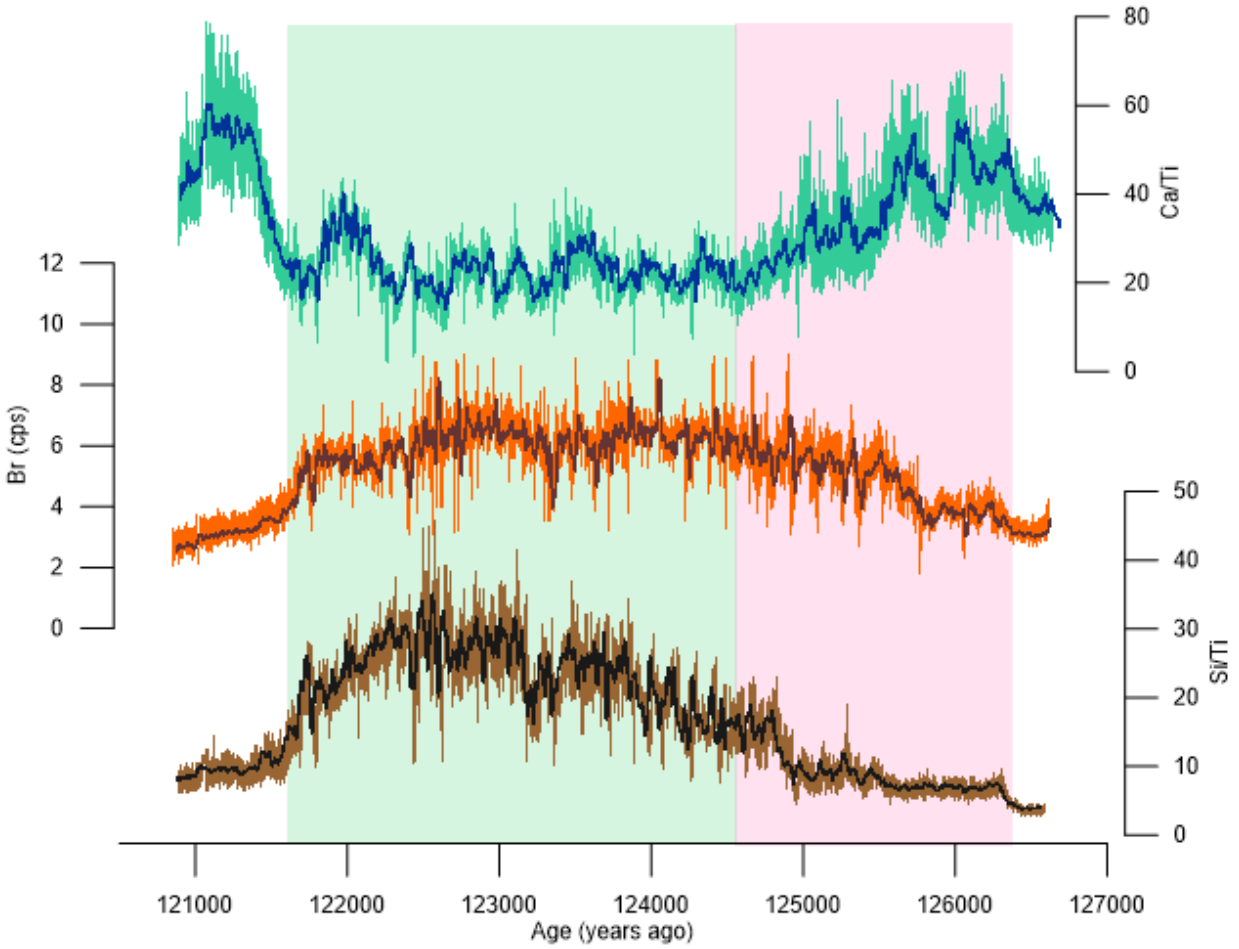

Figure 15: Biogenic silica and carbonate with Br profile- Ca, Si values normalized to Ti and Br values depicting MOC. All with a moving average of 50 points.

3.1.2 Detrital input and source indicators

Zr is an indicator of aeolian input, while K and Ti mainly originate from fluvial input (Martinez-Ruiz et al., 2015; Wu et al., 2018). These elements have been considered as key elements in understanding the contributions from various sources to the core site in this study. There is a significant decrease in the values (in cps) of all these elements in the diatomic region mainly because of the dilution effect caused by the predominance of silica in this facies (Figure 16).

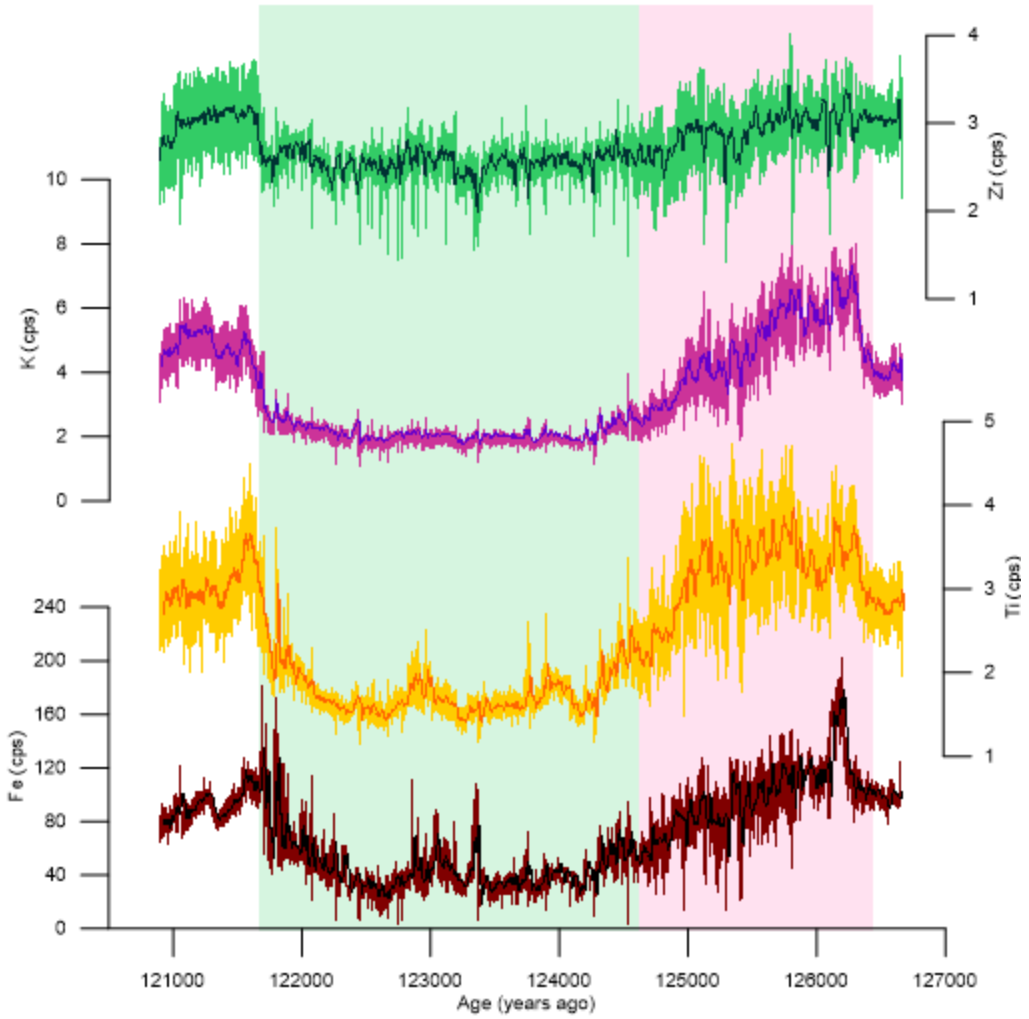

Figure 16: Main detrital input indicators- elemental data of Zr, K, Ti and Fe. All with a moving average of 50 points.

Earlier studies (Sangiorgi et al., 2005; Moller, 2012) have interpreted Ti and K to be from Saharan dust which is considered to be low within the sapropel due to increased vegetational cover. But a more recent study (Wu et al., 2018) have shown diverse sources contributing various detrital material to the site of the studied core. Since new insights can't be provided from just the elemental profiles, fine-scale zooming into the changing fluxes need to be considered as discussed in section 3.5.1.

3.1.3 Oxidation-front towards the end of sapropel deposition

Since the studied sapropel S5 doesn't show any real post-depositional oxidation as indicated by previous studies unlike sapropel S1 (Sangiorgi et al., 2005; Thomson et al., 2006), the Mn/Ti peak and accumulation of chalcophile at the end of the sapropel might

indicate diagenetic remobilisation and deposition at the edge of the downward diffusing oxygen front formed during bottom water re-oxygenation (Figure 17).

There is a peak in Mn/Ti around 123.4 kya which indicates partial oxidation which is likely to be very regional, during this time. A similar trend is observed in core BAN89GC09 from south of Crete in the open Mediterranean (Sangiorgi et al., 2005).

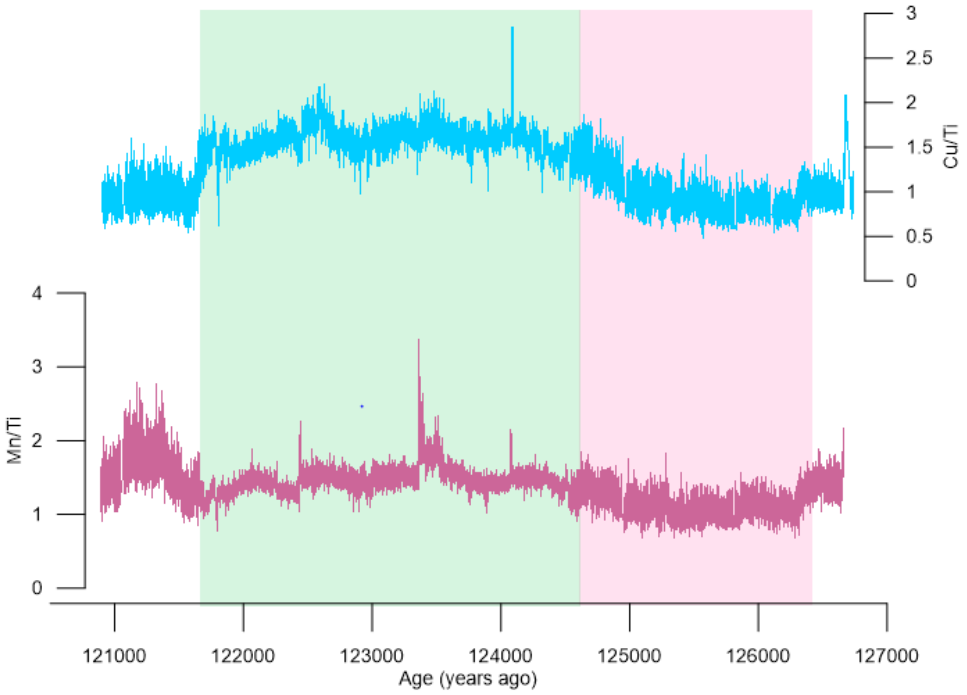

Figure 17: Oxidation-front indicating Cu/Ti and Mn/Ti ratios towards the end of sapropel deposition.

3.2 MSI of biomarker proxies

Twenty sub-sections each of 5 cm were analyzed using LDI-FT-ICR-MS and an average of 57.68, 50.53, 57.13 % successful spectra were obtained for $U^{k'}_{37,}$ CCaT and ACL of fatty acids respectively. Various comparisons and implications from them are discussed below.

3.2.1 Comparing Sea Surface Temperature (SST) proxies

The recent temperature ranges at the Pliny trench area is around 23.6 °C and 18.8 °C in summer and winter respectively and an annual average of 20.5 °C (Conkright et al., 2002). Figure 18 shows that the reconstructed temperature from $U^{k'}_{37}$ data tend to show values similar to mean annual temperature in the Mediterranean while CCaT based

SST data range tend to be more similar to mean summer temperature. This is similar to the results from Kim et al. (2014) where they show that the GDGT derived SST proxy from *Thaumarchaeota* agrees better with warmer summer/autumn SSTs in the Mediterranean than winter or annual mean. (Another GDGT derived temperature proxy TEX_{86}^{L} shows very similar variation like CCaT- see Appendix Figure A1). The amplitude of variation seen in the temperature implies high seasonal contrast between summer and winter temperature during the times of sapropel formation when the extent of the ITCZ shift was augmented.

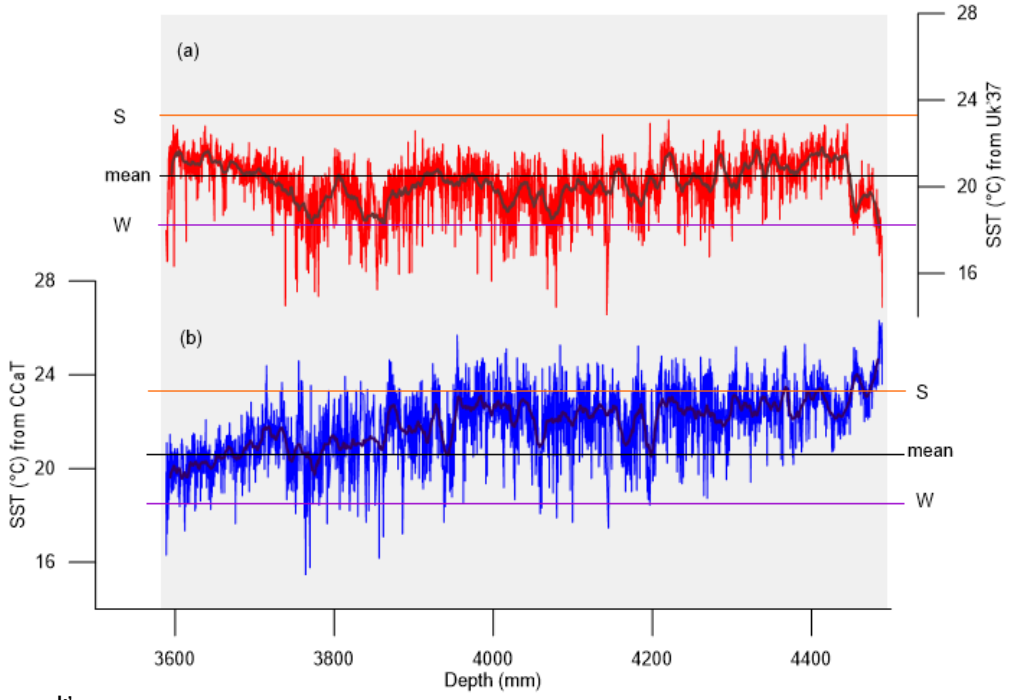

Figure 18: $U^{k'}_{37}$ and CCaT based SST with a moving average of 50 points. The shaded grey area corresponds to the extent of sapropel. Summer (S), mean average and winter (W) temperatures are shown by the lines.

Comparing the previously reconstructed SST available from the literature (Rohling et al., 2002; Marino et al., 2007; Moller, 2012), the trend shown by $U^{k'}_{37}$ values seems to be more promising (See Figure 19 and Figure 3) in reconstructing SST.

Marino et al. (2007) shows that along with a sharp $\delta^{18}O$ shift to lighter values, SST from core 971A, KS205 and SL104 show a gradual increase at the onset of sapropel formation and freshwater flooding (Figure 20). The $U^{k'}_{37}$ SST data (Figure 20) shows a similar increase around 125.8 kya (~600yrs after the onset of sapropel). Br values representing MOC also shows a similar trend where it is gradually increasing till around

125.8 kya and reaching the highest productivity following that (Figure A2). This may indicate that along with the increased freshening and increased upper ocean temperature, a shoaling of pycnocline occured around this time. This led to nutrient-rich water reaching the photic zone and development of a deep chlorophyll maximum (at around 100-140 m in the Eastern Mediterranean) subsequently (Weldeab et al., 2003). Development of photic zone euxinia (as indicated by the Marino et al., 2007 – isorenieratene concentration) and absence of *G. inflate* which are considered as indicators of vertical mixing of upper water column (Sangiorgi et al., 2005) also supports the development of more stable stratified water column around this time.

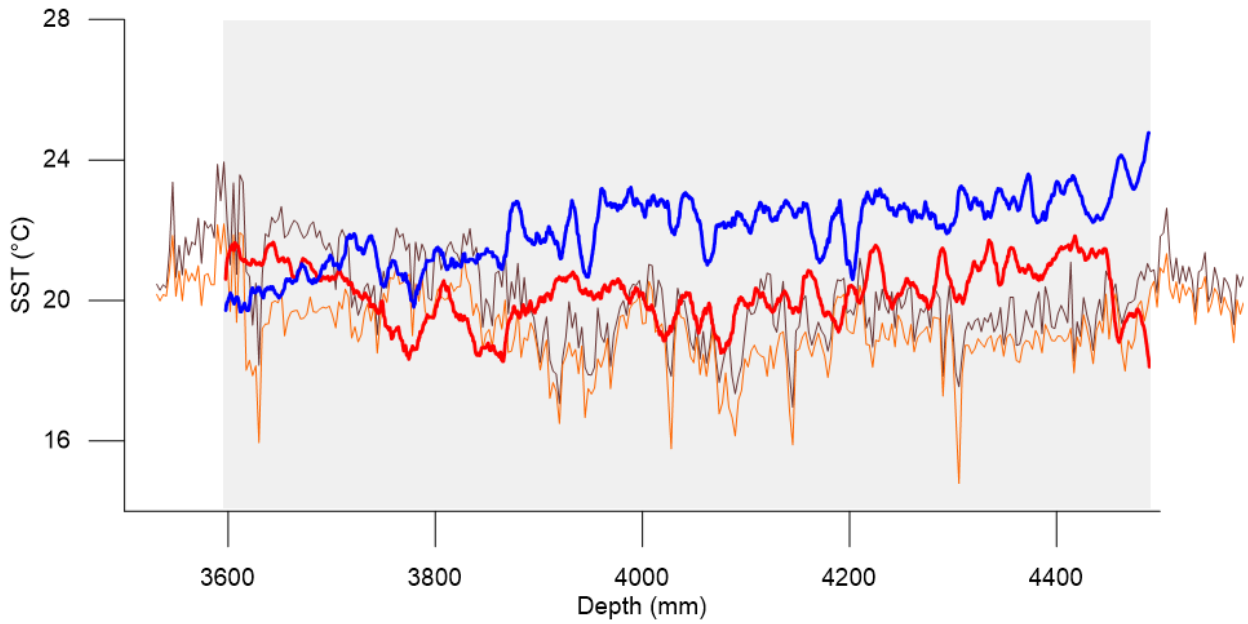

Figure 19: Comparing SST reconstruction for the sapropel section (shown as grey shaded region). Lines indicate a moving average of 50 points for SST based on $U^{k'}_{37}$ (red) and SST based on CCaT (blue). The brown line and orange lines indicate the upper and lower limit of annual average temperature calculated from census data of planktonic foraminifera (Moller, 2012). The graph is plotted in the depth units (in mm) to compare it with the SST data from the literature, also provided in the same units.

The variation between the CCaT derived SST with other alkenone derived SSTs points to additional factors that might be modulating the CCaT proxy as shown by Qin et al. (2015); Evans et al. (2018). After deep chlorophyll maximum formation due to shoaling of the pycnocline, CCaT values broadly follow a very similar trend to $U^{k'}_{37}$ derived SST (Figure 18, 19 and Figure A2). While during the initial stages of sapropel formation, higher CCaT values indicate low salinity surface water influence from sudden increase

in freshwater flux and lower nutrient and oxygen conditions (due to lack of upwelling of nutrients from bottom water or winter mixing indicated by absence of *G. inflata* (Sangiorgi et al., 2005)). This corresponds to low productivity areas from Br profile till around 125.8 kya, further supporting the hypothesis. This might give warmer CCaT values in the initial stages of sapropel deposition.

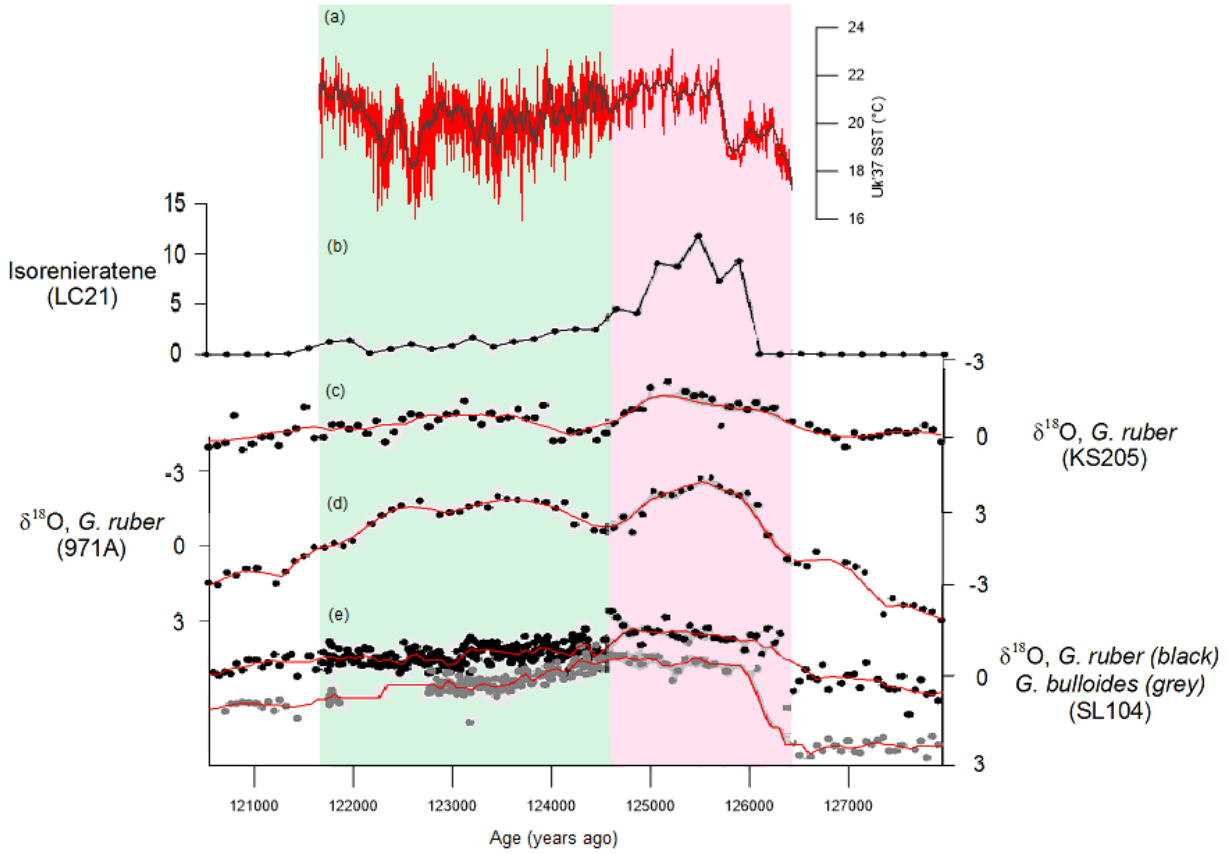

Figure 20: Development of deep chlorophyll maximum implied from $\delta^{18}O$ and other proxies- (a) $U^{k'}_{37}$ based SST (b) Isorenieratene concentration (µg/g sed) (Marino et al., 2007) (c) and (d) $\delta^{18}O$ values from *G. ruber* (Cane et al., 2002) (e) $\delta^{18}O$ values from *G. ruber* and *G. bulloides* from core SL104 (Moller, 2012).

Since the GDGT derived temperature proxy from *Thaumarchaeota* agree better with warmer summer/autumn SSTs in the Mediterranean (Kim et al., 2014), it may indicate that the depth of Thaumarchaeal production may have become shallower (hence warmer). Since euxinic and anoxic conditions prevailed near the photic zone during the same time along with intensified water column stratification (Marino et al., 2007; Rohling et al., 2015), they may have undergone high oxygen stress during that time (warmer signal) (Qin et al., 2015). The deviation of CCaT SST at the end of the sapropel seems

to follow the decreasing insolation pattern around that time (see Figure A3), while $U^{k'}_{37}$ SST increases further, implying conditions of warmer temperature in the surface layer. Hence CCaT signal is under the influence of salinity and acute oxygen limitation here, in addition to SST.

3.2.2 Regional vegetation changes during the climatic optimum

The average chain length of fatty acids shows a general increasing trend towards the top of the sapropel, going from lower ACL to higher ACL values (Figure 21). This might be indicative of changes in the type of terrigenous vegetation cover over the Saharan region. Since additional isotopic data is required to establish that the vegetation change from a C_3 dominated cover (lower ACL) to C_4 dominated ones (higher ACL) occurred, interpreting them as vegetation indicators must be done cautiously. Several terrestrial proxies from leaf waxes produced by land plants comprising n-alkanes, n-alkanols and n-alkanoic acids (fatty acids) are governed by additional factors like moisture conditions (humidity/ aridity), temperature, evapotranspiration other than changes in the plant biome (Diefendorf and Freimuth, 2017). However, there may be a transition trend that can be inferred from the ACL profile, where there was a humid condition at the onset of sapropel to more drier conditions towards the end (similar to the relation inferred by Hughen et al. (2004) in studies done in Cariaco Basin). This trend intimates the shift of ITCZ southwards and the decline in monsoonal intensity as the insolation decreases.

The terrigenous to aqueous ratio of fatty acids, TARFA (Figure 21) shows the variation of terrigenous (allochthonous) fatty acids with respect to autochthonous marine ones. There are few outlier regions in the TARFA profile giving anomalously high values (substantially above 1), possibly due to some ionization issue (see Figure A4) and single deviant values. Excluding these, the TARFA values depicted here are well in range, showing a larger fraction of fatty acids of marine origin as expected in this marine sediment coming into the site and variation of terrigenous fatty acids recorded here.

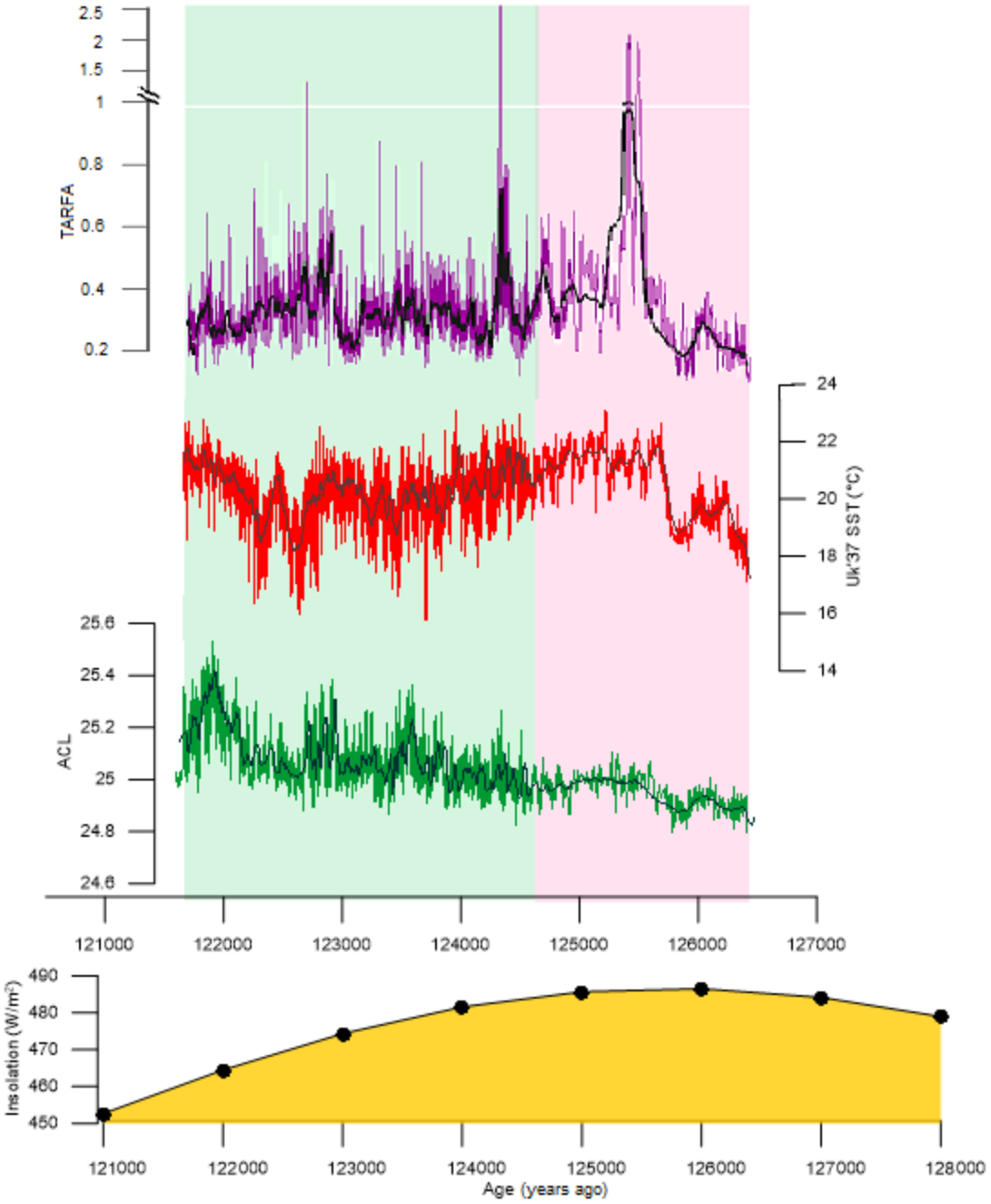

Figure 21: Paleovegetation indicators with SST and insolation curve- TARFA for fatty acids (purple), $U^{k'}_{37}$ based SST (red), ACLof long-chain fatty acids (green). Summer insolation curve at 65°N (Berger and Loutre, 1991).

3.3 Validating MSI data by conventional methods

In order to evaluate whether the FT-ICR-MS derived proxy data show a similar trend in variation with conventional methods, they were compared with measurements taken with HPLC/GC-MS methods. All the LC measurements were analyzed and internal calibration was checked for standard deviation less than 0.5 ppm.

3.3.1 Broad-scale correlation for the whole sapropel

All the three proxies, in general, showed a good correlation between the FT measurements and the conventional GC and LC measurements (Figure 22).

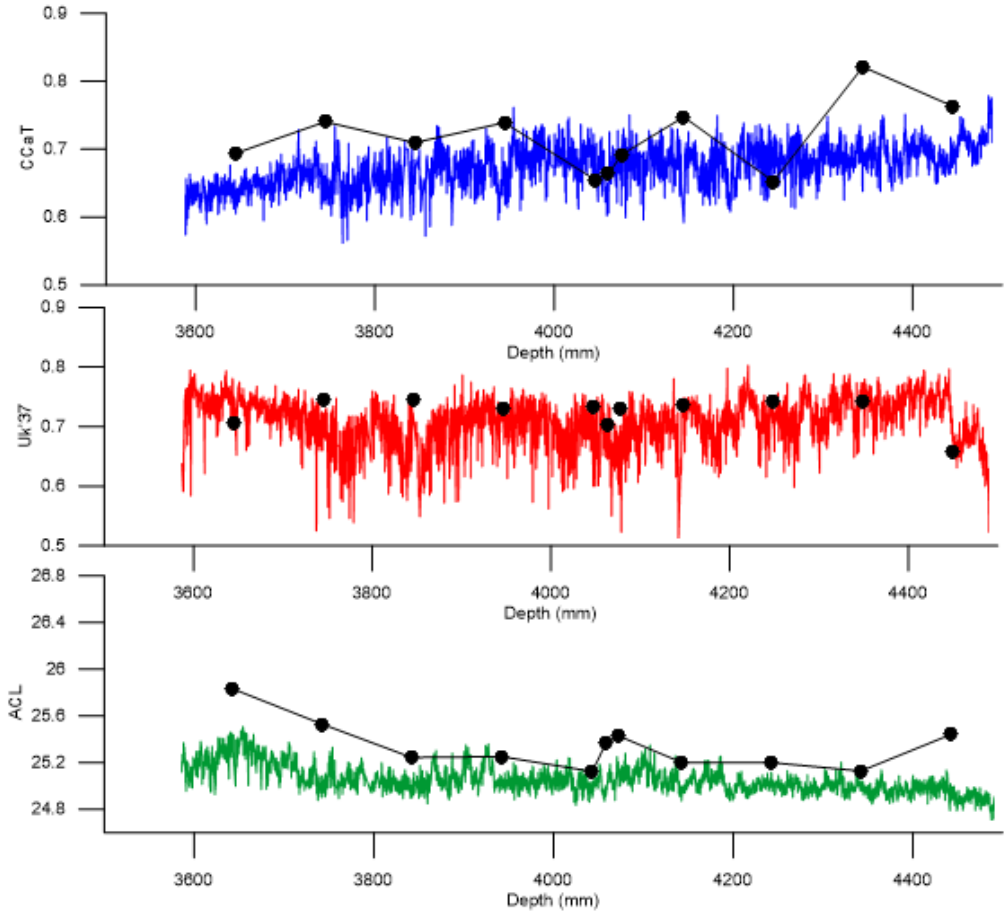

Figure 22: Comparing CCaT, $U^{k'}_{37}$ and ACL trends from FT measurements (blue, red and green plots respectively) with GC and LC measurements (black line/scatter plot- size of the marker approximately represents the sample depth averaged by GC measurements).

Though the absolute values are deviating between the conventional and FT-ICR-MS methods, the trend displayed is generally consistent. The deviation is acceptable given the variation in setting up parameters like time of flight in the FT measurements which might give a consistent shift in the values obtained. The shift is more apparent for the ACL values of fatty acids which are mainly because of the MultiCASI method used with two windows of interest. This might lead to a significant shift in the absolute values as both the windows are working at the same time of flight value set, which might affect

the efficiency of detection of these ions. Nonetheless, the trend observed is concordant between FT and the conventional method.

3.3.2 High-resolution correlation for sub-sample

The high-resolution conventional data of 0.5 cm resolution performed with selected 5 cm interval fits well with the FT measurements from the same interval. The general trend between the conventional and FT method in both CCaT and $U^{k'}_{37}$ SST values are coherent, similar to what was observed in broad scale correlation (Figure 23).

To test the sensitivity of the MultiCASI method and to compare it with how the values might change if just a single window is used, this 5 cm sub-sample was also measured in a single window for the long-chain fatty acids. This is shown in the comparison between the MultiCASI method (ACL (i) in Figure 23) and single window CASI method (ACL (ii) in Figure 23). The units of GC measurements are the same as ACL (ii) single CASI window and they are closely agreeing with each other. The MultiCASI measured ACL (i) though is shifted in absolute values and in terms of amplitude, the trend depicted is similar. Consequently, variations of the data can be considered as a reliable signal, although the amplitude of variations should be considered with care.

Linear correlation between LDI-FT-ICR-MS and GC/HPLC-MS measurements was checked (Figure 24) by comparing GC/LC data points with the average of the FT data from the same interval (see vertical bars in Figure 23). The ACL comparison plot was made after removing the first outlier point seen in the GC measurement for the ACL. The R^2 values of ACL and CCaT thus obtained (R^2=0.757 and 0.657 respectively) gives a good correlation. Though the comparison with $U^{k'}_{37}$ data shows that the correlation isn't that robust (since R^2=0.41 is rather small) a similarity in trend can be observed as discussed above.

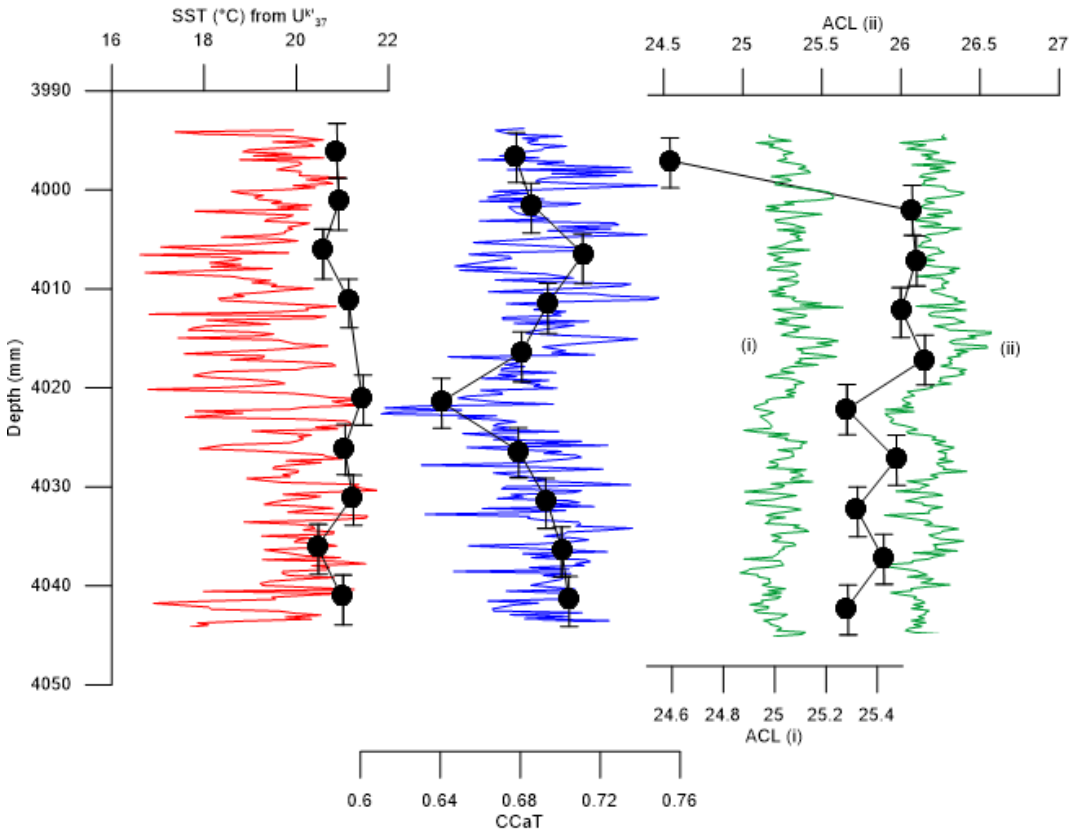

Figure 23: $U^{k'}_{37}$ SST (red), CCaT (blue), and ACL (green) trends for 5 cm sub-section. ACL (i) indicates measurements from MultiCASI window and ACL (ii) indicates data from single CASI window. Black line/scatter plot shows GC data. The vertical bars in the marker approximately represent the sample depth averaged by GC measurements. ACL (ii) is the x-axis for GC data of ACL.

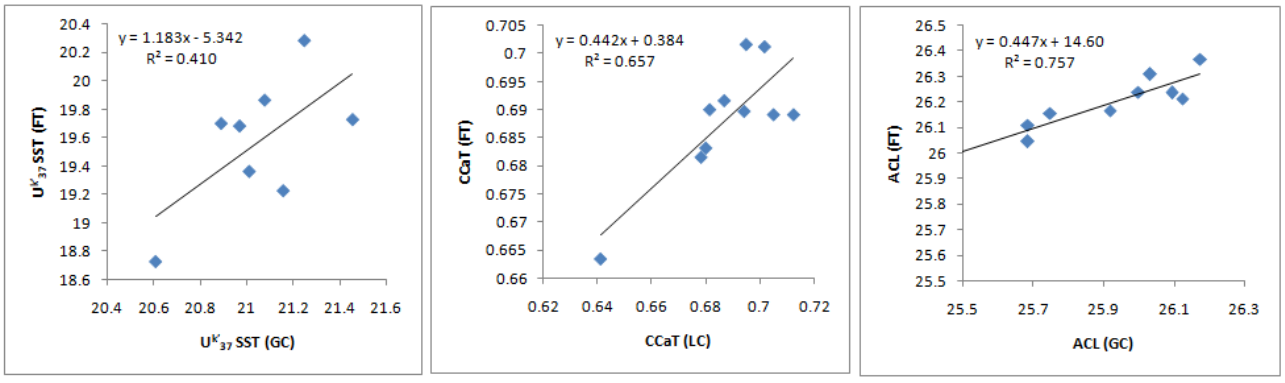

Figure 24: Linear correlation between LDI-FT-ICR-MS vs. GC/HPLC-MS measurements (averaged for the same interval) for $U^{k'}_{37}$, CCaT and ACL data.

3.4 PCA on elemental and biomarker proxies

PCA analysis was performed on all the biomarker proxies and elemental data to investigate the clustering and correlation between them.

The non-diatomic sapropel till lightest $\delta^{18}O$ values (brown in Figure 25) shows a clustering along the PC1 which is further away from rest of the sapropel data points and gives a signal more similar to non-sapropel marl area. This is similar to what was observed by Moller (2012), indicating that the geochemical setting during the initial stages of sapropel formation was quite different in this transitional time.

The organic-rich sapropel data points are shown to form a different cluster along the negative axis of PC1 where they show clustering of elements contributing to the biogenic fraction of the sediment (Br, Si, Cu) (Figure 25). Trace element Cu is known to complex with enzymes of several marine phytoplankton (Morel et al., 2003) which explains its correlation with the biogenic component.

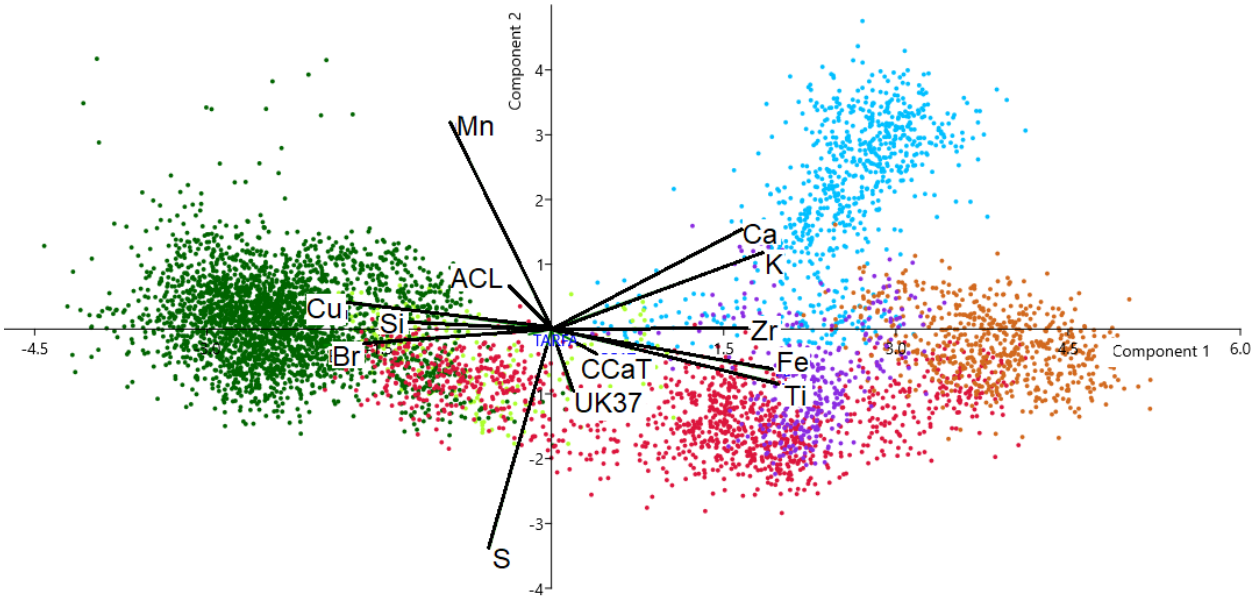

Figure 25: PCA analysis of elements and biomarkers-Scatter plot for PC 1 (x-axis) and 2 (y-axis). The data was colour coded based on the region it represents in terms of their age. Transition is from initial non-sapropel (purple) data to non-diatomic sapropel till lightest $\delta^{18}O$ values (brown) to rest of the non-diatomic sapropel (crimson) to diatomic sapropel (green) to top bioturbated sapropel (yellowish green) to post sapropel marl (sky blue).

In contrary, values on the positive direction of PC1 show clustering of elements contributing to terrigenous/detrital part of the sediment are observed (Ti, K, Fe, Zr). Mn and S are elements indicative of redox conditions and has more influence on PC2, but in opposite directions, indicating different settings (oxic and anoxic conditions respectively) to which it contributes. Ca is seen to correlate more with the terrigenous

fraction though biogenic carbonate is abundantly also present in the sapropel. This is also evident from the loading plots of PC1 and 2 (Figure 26).

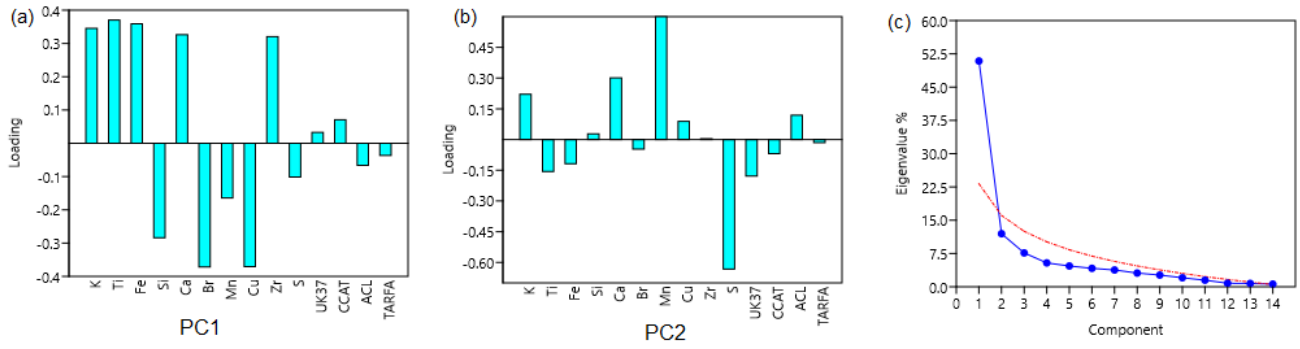

Figure 26: (a) and (b) Loading plots for PC1 and PC2 respectively. (c) Scree plot

Table 4 shows all the principal components and the percentage of variance explained by each of them. Table 5 shows loadings for PC1 and 2. Hence, PC1 is capturing the behavior of detrital vs. biogenic components in the sediment and in counter relation (see the transitional trend from positive to negative PC loadings respectively in Figure 27). PC2 records redox setting in the sediment sample in general, showing negative loadings in the beginning during euxinic conditions (around 125 kya) and shifting towards more positive oxic conditions towards the end of sapropel (Figure 27). Though care should be taken regarding this interpretation since PC2 explains only 12% of the variance. It is also observed that ACL and TARFA show higher loading towards the biogenic fraction and is in relation to PC1. In contrary, CCaT and $U^{k'}_{37}$ show loading in the opposite direction.

Further PCA was done on a few selected elemental ratios and biomarker proxies to verify if they show similar correlation as non-normalized elemental ratios with biomarkers (Figure 28). Similar results to the previous PCA were obtained here as well. Si and Br normalized to Ti were used to obtain the relationship between biogenic silica contribution and normalized MOC.

The biomarker proxies show similar distribution as before into biogenic and non-biogenic clusters (see Figure 29 and Table 6 and 7). But the contribution to PC2 is rather difficult to delineate.

PC	Eigenvalue	% variance
1	6.27737	50.895
2	1.47626	11.969
3	0.941872	7.6364
4	0.664965	5.3914
5	0.57983	4.7011
6	0.513804	4.1658
7	0.46759	3.7911
8	0.382764	3.1033
9	0.326499	2.6472
10	0.252097	2.0439
11	0.183177	1.4852
12	0.100218	0.81254
13	0.0925991	0.75077
14	0.0748709	0.60703

	PC 1	PC 2
K	**0.34534**	0.22114
Ti	**0.37048**	-0.15614
Fe	**0.35896**	-0.118
Si	**-0.28411**	0.027364
Ca	**0.32652**	**0.30149**
Br	**-0.37151**	-0.04696
Mn	-0.16443	**0.59979**
Cu	**-0.37059**	0.088744
Zr	**0.32073**	0.003554
S	-0.10129	**-0.63287**
UK37	0.032625	-0.17815
CCAT	0.070546	-0.06912
ACL	-0.0664	0.11848
TARFA	-0.03652	-0.01494

Table 4: (left) Principal components with their eigenvalues and % of the variance for data represented in Figure 25.

Table 5: (right) Major principal component analysis loadings. Bolded loadings here correspond to values greater than the square root of (1/n), where n is the number of variables used, thus indicating their significance.

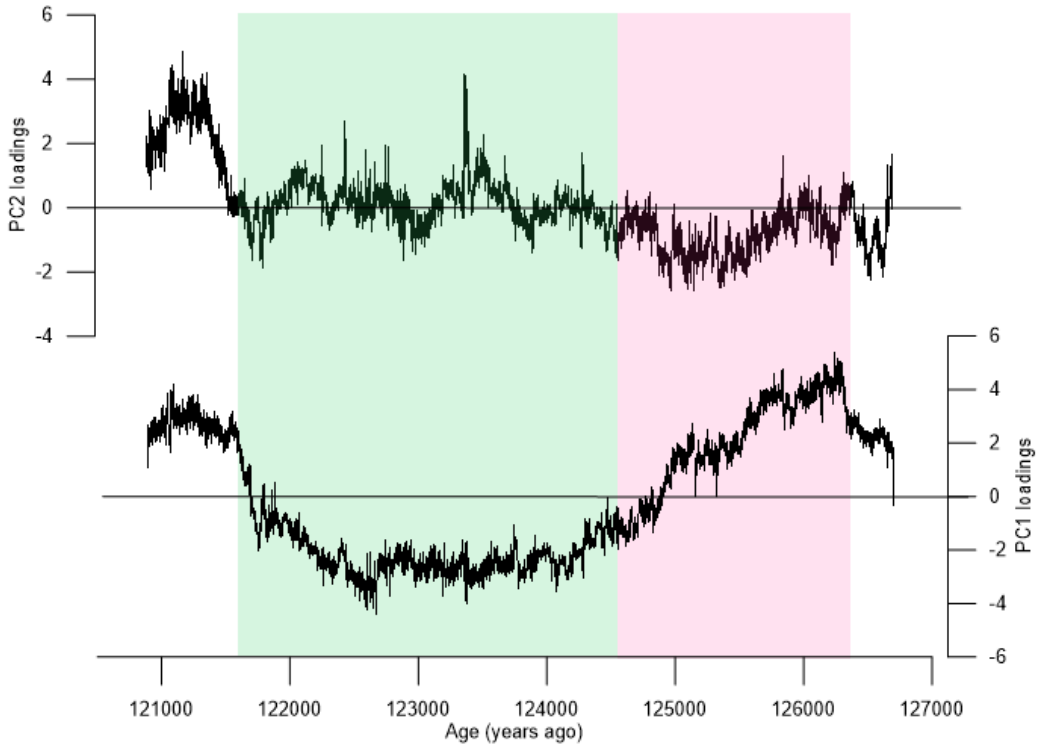

Figure 27: PC1 and PC2 loadings depicted in the age model showing contributions to of detrital vs. biogenic components in PC1 and redox settings for PC2.

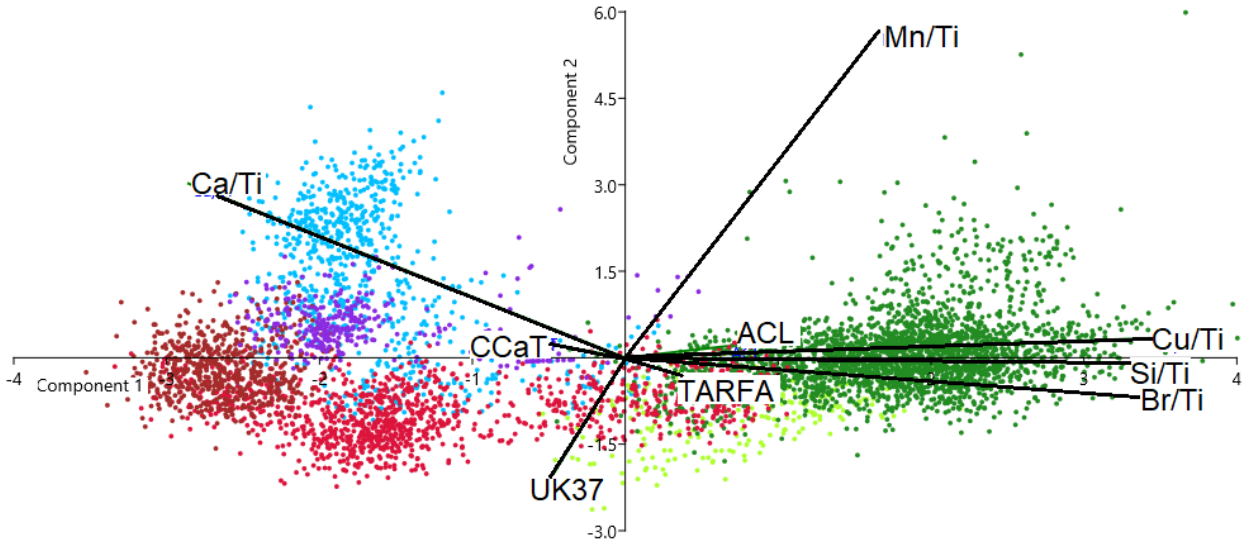

Figure 28: Scatter plot for PCA for elemental ratios and biomarker proxies. Same colour coding is followed as in Figure 25.

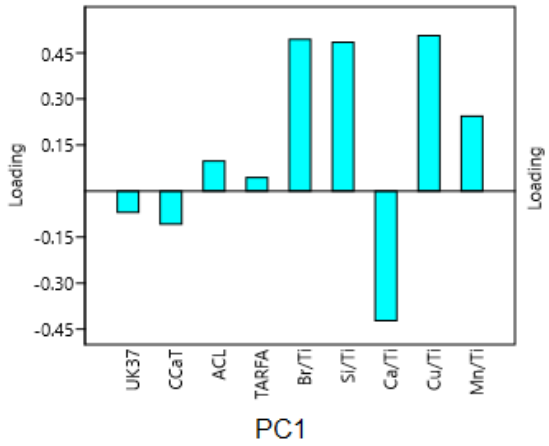

PC	Eigenvalue	% variance
1	3.54222	48.111
2	0.996237	13.531
3	0.805509	10.94
4	0.616105	8.368
5	0.507094	6.8874
6	0.385099	5.2304
7	0.242795	3.2977
8	0.155238	2.1085
9	0.112351	1.526

	PC 1	PC 2
UK37	-0.06921	-0.29685
CCaT	-0.10753	0.053054
ACL	0.097607	0.029552
TARFA	0.043991	-0.03832
Br/Ti	**0.49371**	-0.10113
Si/Ti	**0.48437**	-0.01352
Ca/Ti	**-0.42198**	**0.44633**
Cu/Ti	**0.50617**	0.050219
Mn/Ti	0.24402	**0.83342**

Figure 29: Loadings for PC1 for elemental ratios and biomarkers

Table 6: (left) Principal components with their eigenvalues and % of the variance for elemental ratios for the data represented in Figure 28.

Table 7: (right) Major principal component analysis loadings for elemental ratios and biomarkers. Bolded loadings here correspond to values greater than the square root of (1/n), where n is the number of variables used, thus indicating their significance.

PCA analysis on the biomarkers alone was done to observe how the clustering of data varies when compared with clustering observed with the sediments (Figure A5). It shows that the non-diatomic values (crimson) and diatomic values (green) cluster together as opposed to the separation observed when elemental data were combined. This implies that the change in the geochemical setting with a strong correlation between biogenic and terrigenous elements is controlling the PCA analysis to separate

the non-diatomic and diatomic regions from each other. Since the percentages of variance explained by the PCs are spread over all the PC values, it is difficult to make a clear conclusion on correlations between various biomarkers, though an anti-correlation between CCaT and ACL and positive correlation between TARFA and $U^{k'}_{37}$ is observed. This anti-correlation between CCaT and ACL indicates that periods of increase in summer temperature and monsoonal precipitation coincides with decreased ACL, indicative of humid climate. Further comparisons and analysis of these biomarkers will be dealt with in section 3.5.4.

3.5 Spectral, wavelet and phase analysis

Various elemental and biomarker proxy data were considered for these spectral, wavelet and phase analysis and only the ones that showed a consistent trend with high enough coherence are discussed here.

3.5.1 Contribution of detrital fraction from riverine inputs

In order to discern the source of detrital sediment coming into the location of the studied sediment core, specific phase analysis was done on major elements like K, Ti and Zr known to contribute detrital material via aeolian/ fluvial input.

Bandpass filter output (Figure 30) shows that in decadal and yearly scale (Figure not shown here), both K and Ti are highly coherent (same frequency range but different phase relation), which suggest either a common source or common forcing behind them and might feature certain deviation giving a lead or a lag. The coherence of Zr with K and Ti is comparatively less as seen from phase analysis plot as well (Figure 31).

The phase analysis depicts a lead of K with Ti by around 2.6 years on a yearly scale and around 15 years in the decadal scale. This difference, given their high coherence, indicates a common forcing of increased monsoonal discharge during the sapropel times but different sources of K and Ti coming in from the Aegean Sea riverine inputs and Nile discharge respectively (Wu et al., 2018). Zr and Ti are seen to be approximately in anti-phase with each other. Given that the source of Zr is mostly from aeolian flux from the Saharan region, this suggests that periods of wet and dry cycles control the Ti influx from Nile discharge and Zr transported by aeolian input from the Sahara. It is also evident that since none of the elements is approximately in-phase with

each other, they may not have a common origin contributing to synchronous flux into the Mediterranean.

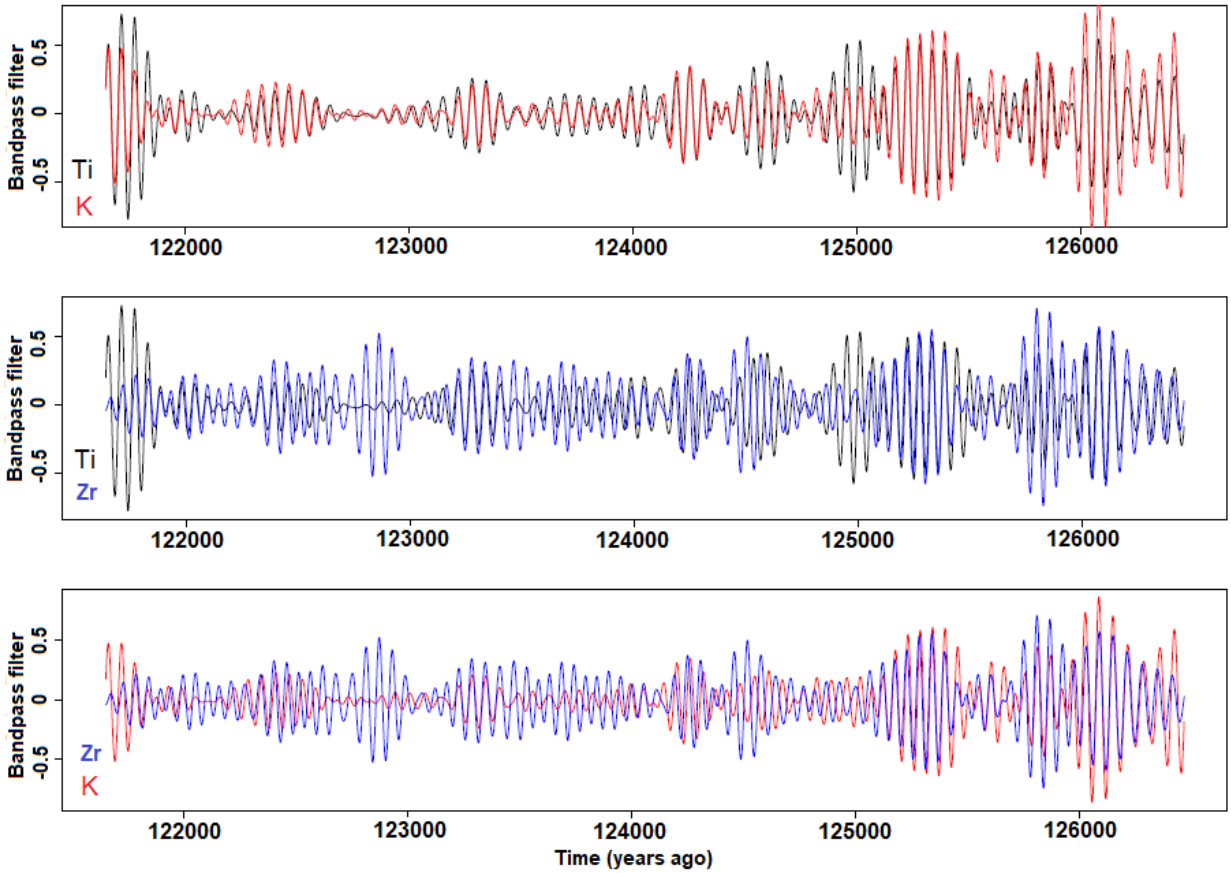

Figure 30: Bandpass filter output in the decadal scale for major elements from the terrigenous fraction showing high coherence between them.

According to Wu et al. (2018), the time frame in which the transition from non-diatomic facies (sky blue panel in Figure 31), indicative of initial stages of sapropel deposition to the diatomic facies (red and green panel related in Figure 31), is when the contribution of the Aegean Sea riverine input decreases and more of southern borderland input comes in to the location of the studied core. If this is considered true, the K contribution from Northern Borderlands decreases and become more similar to how Ti might behave from the Nile discharge. Hence K and Zr would start showing a phase relation close to anti-phase to each other, as correctly seen here in the yearly scale in red and green panels (Figure 31 bottom-most polar plots).

Looking into clay minerals composition Figure A6, there is a prominent increase in Kaolinite/Chlorite ratio in the later stages of sapropel deposition (in the diatomic region), indicating a decreased contribution from NBEM. This further supports the conclusion that there was a change in the amount of contribution of detrital material coming in from northern and southern borderlands.

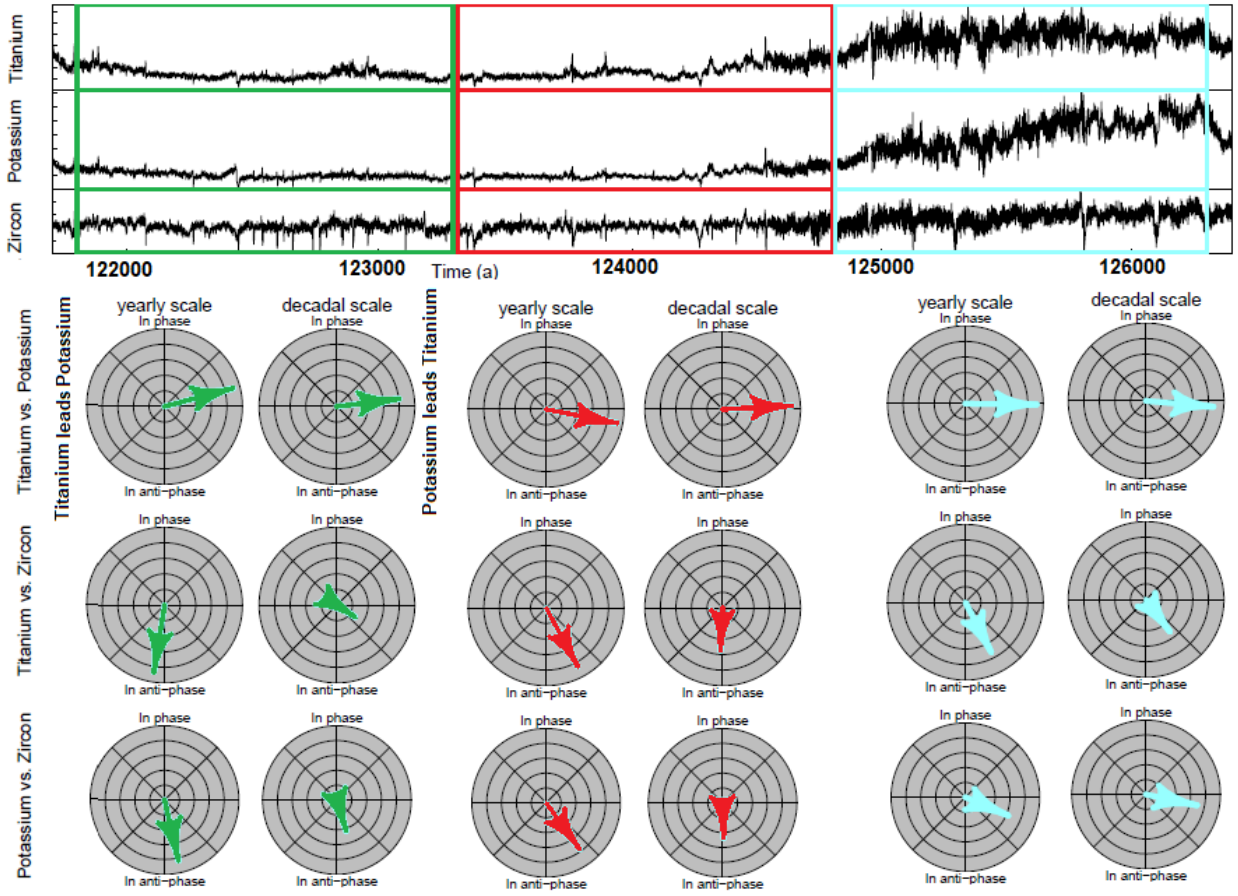

Figure 31: Phase analysis plots in yearly and decadal scale for major elements from terrigenous fraction. Colour-coded according to the sub-divided sections for multiple analysis. Profiles of the elements are shown in the top of the figure.

The likely reason for this change is that during initial stages of sapropel deposition the increased monsoonal precipitation led to an influx of material from both northern and southern borderlands through some global teleconnection. But since there were extensive vegetational cover formation in the North Africa, the Nile sediment contribution was less during the initial stage (Hennekam, 2015; Wu et al., 2018) and

might have increased through time due to shrinking vegetational cover as ITCZ shifted back south.

Hence it shows that, there exists a complex interplay between various sources of riverine input into the site of the studied sediment core.

3.5.2 Marine organic productivity and water column stratification

Since variation in marine productivity is partly controlled by upwelling conditions and vertical mixing in the water column/ stratification, phase analysis between productivity indicator Br and $U^{k'}_{37}$ SST was done to analyze the response time of short-scale cycles intrinsic to the system. The phase analysis reveals that there is a lead of Br from $U^{k'}_{37}$ SST by around 1.3 years (coherence of around 0.6) (Figure 32). This intimates that there is a yearly cycle of periods of higher productivity (when the vertical mixing of water column and upwelling occurred) and is followed by increasing temperature conditions (leading to more stratification of water column). This indicates a cycle where an increase in productivity drives to a more anoxic condition (and increased preservation of organic matter) followed by a period of more stratified water column development and higher surface water temperature. Hence this shows inter-connected cycles of increased productivity periods followed up by increased SST and water stratification conditions.

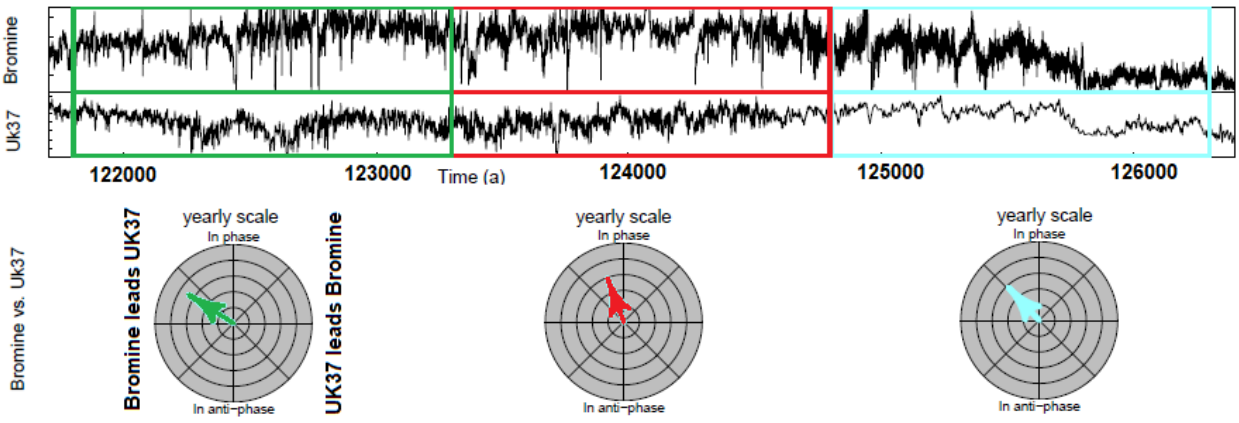

Figure 32: Phase relation between MOC and productivity indicator Br and SST- Br is leading $U^{k'}_{37}$ SST

3.5.3 Dynamics of terrestrial vs. marine organic matter transport

Br is validated to be of autochthonous origin in the studied sapropel presenting MOC and paleoproductivity. In contrary, TARFA ratio is supposed to represent organic carbon transported by detrital fraction (allochthonous) with respect to marine productivity (fatty acids of autochthonous origin). This is corroborated in the anti-phase relation seen between them (Figure 33 red and green panel), with a coherence of around 0.6 in the sapropel. During the initial stages of sapropel deposition, they seemed to have a different phase relation which could be attributed to gradually increasing marine productivity and change in vegetation cover during this time.

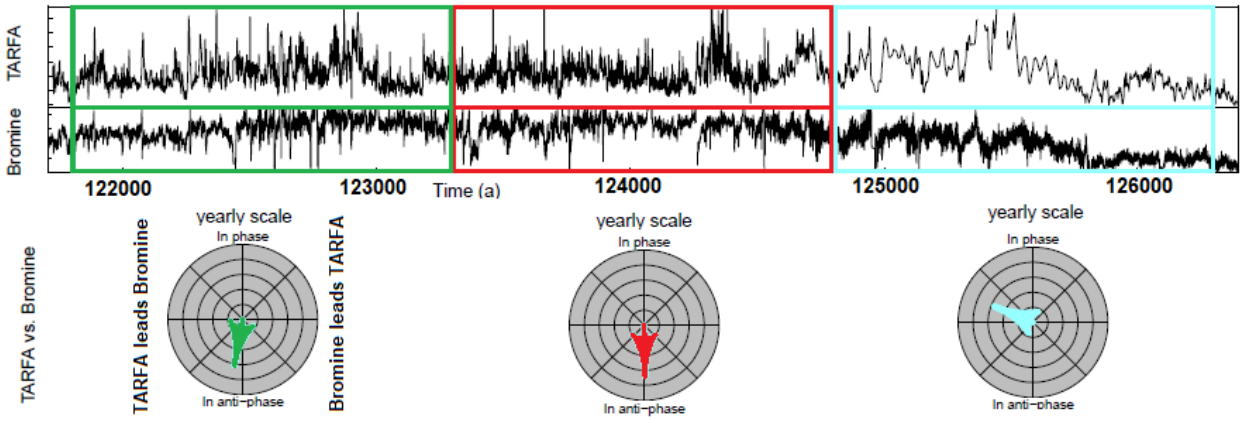

Figure 33: Anti-phase relation between Br and TARFA- autochthonous vs. allochthonous origin

3.5.4 Decadal-scale oscillations during sapropel formation and its implications

The wavelet analysis adds in another dimension into looking at how spectral density changes over time. The wavelet analysis (Figure 35) in the non-diatomic facies, from the beginning of sapropel till around 124.6 kya shows hardly any yearly cycles as expected from the low sedimentation rate. On the other hand, the high sedimentation region shows yearly cycles in all the biomarker proxies. In the centennial scale, TARFA and $U^{k'}_{37}$ show high spectral signal towards the beginning and end of the sapropel, giving a cyclicity of between 250- 640 years. It is difficult to understand what these signals might indicate since it is quite broad and spread over several hundreds of years.

In the decadal scale, oscillating high and low spectral power density is observed for CCaT and ACL. And this is nearly in sync with each other indicating some multi-decadal

oscillation in play. They also show high coherence in bandpass filter output (Figure 34). Similar kind of decadal oscillation signals are also observed in several elemental data like for Ca, Fe and for Ti and K though only to a lower density (Figure 36). This implies oscillation dynamics of various geochemical parameters coming together.

The phase analysis in the decadal scale (Figure 37) shows that there is a lead of CCaT from ACL by around 8.75 years with an average coherence of around 0.75. Since the coherence of combinations of other proxies isn't very high, the phase relation between them can't be clearly validated.

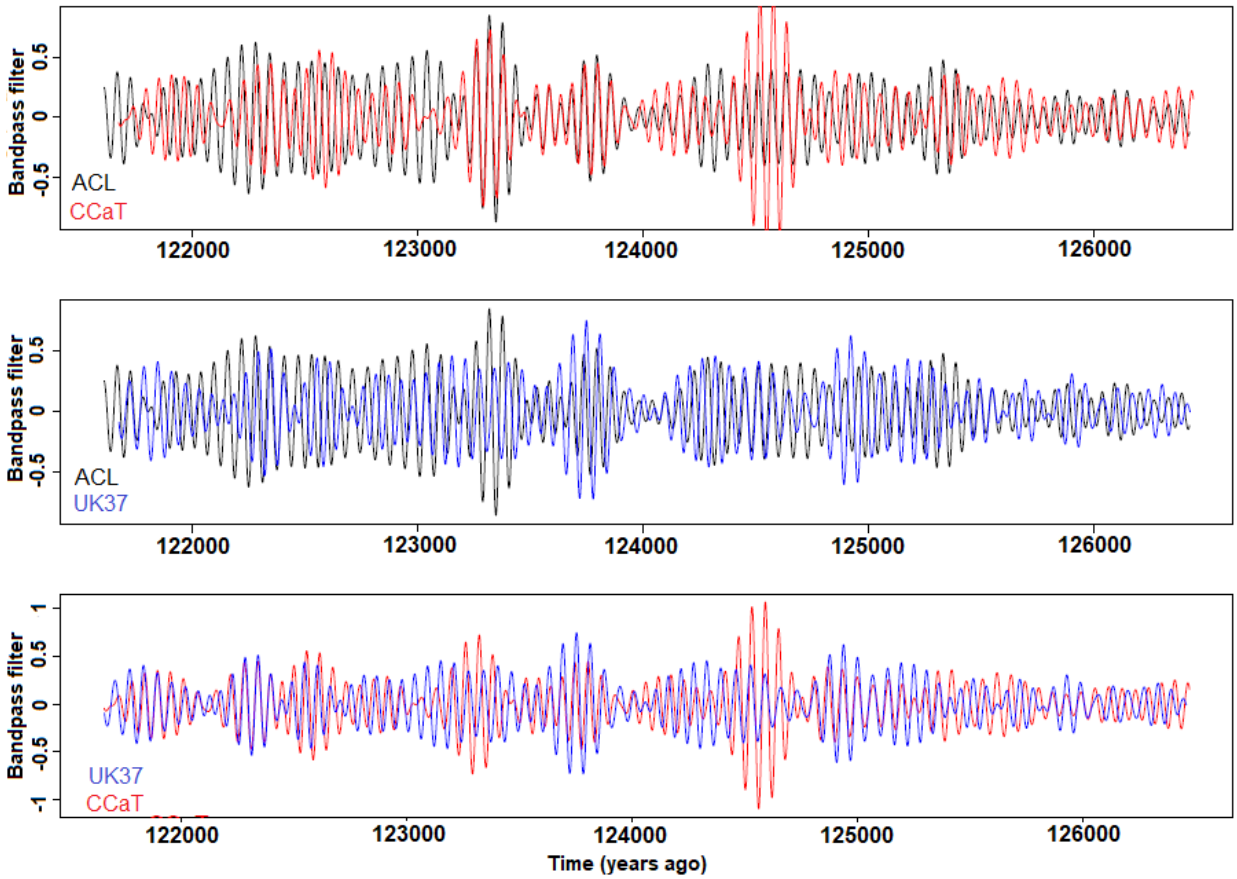

Figure 34: Bandpass filter output showing biomarker variability in the decadal scale

It is observed that there is no consistency or coherence in $U^{k'}_{37}$ derived SST and ACL values in the phase analysis, while CCaT derived temperature and ACL shows good coherence (Figure 34, 37). This indicates that something other than simple temperature is modulating this phase relation. First, there is an increase in CCaT values (indicating increased summer temperature and conditions of oxygen stress in the stratified water

column due to increased monsoonal precipitation) and following this, a nine-year lag or response time for a change in ACL (indicative of vegetational shift) can be implied. This lag could be the response time required for the vegetational changes to occur in the borderlands following a period of high precipitation.

Hence this likely reflects something similar to Atlantic multi-decadal oscillation (AMO) in play during these times of sapropel formation, setting up changes in global ocean circulation patterns and variability in surface temperatures. AMO is estimated to have a periodicity of around 60 years (Scafetta, 2014) and is associated with anomalies in SST over the North Atlantic and inter-hemispheric temperature contrast in the Atlantic. Zhang and Delworth (2006) and related statistical studies have shown that the positive phase of AMO is associated with a northward shift of ITCZ and accompanying increased summer rainfall in India and Sahel regions. Thus this point towards a multi-decadal variability in SST followed by changes in the precipitation pattern, corroborating the phase analysis results between CCaT and ACL as discussed above.

Zhang and Delworth (2006) and Toucanne et al. (2015) show storm events over the Mediterranean connected to North Atlantic origin during these pluvial periods of sapropel formation and monsoon precipitation, which give rise to increased rainfall over northern borderlands of the Mediterranean. This explains the similar oscillations in spectral density seen between various elemental data related to hydrological changes and ACL and CCaT (Figure 36). Thus a coupling between low and mid-latitude hydrological changes and the response of global climate system is evident in the Mediterranean during the last interglacial.

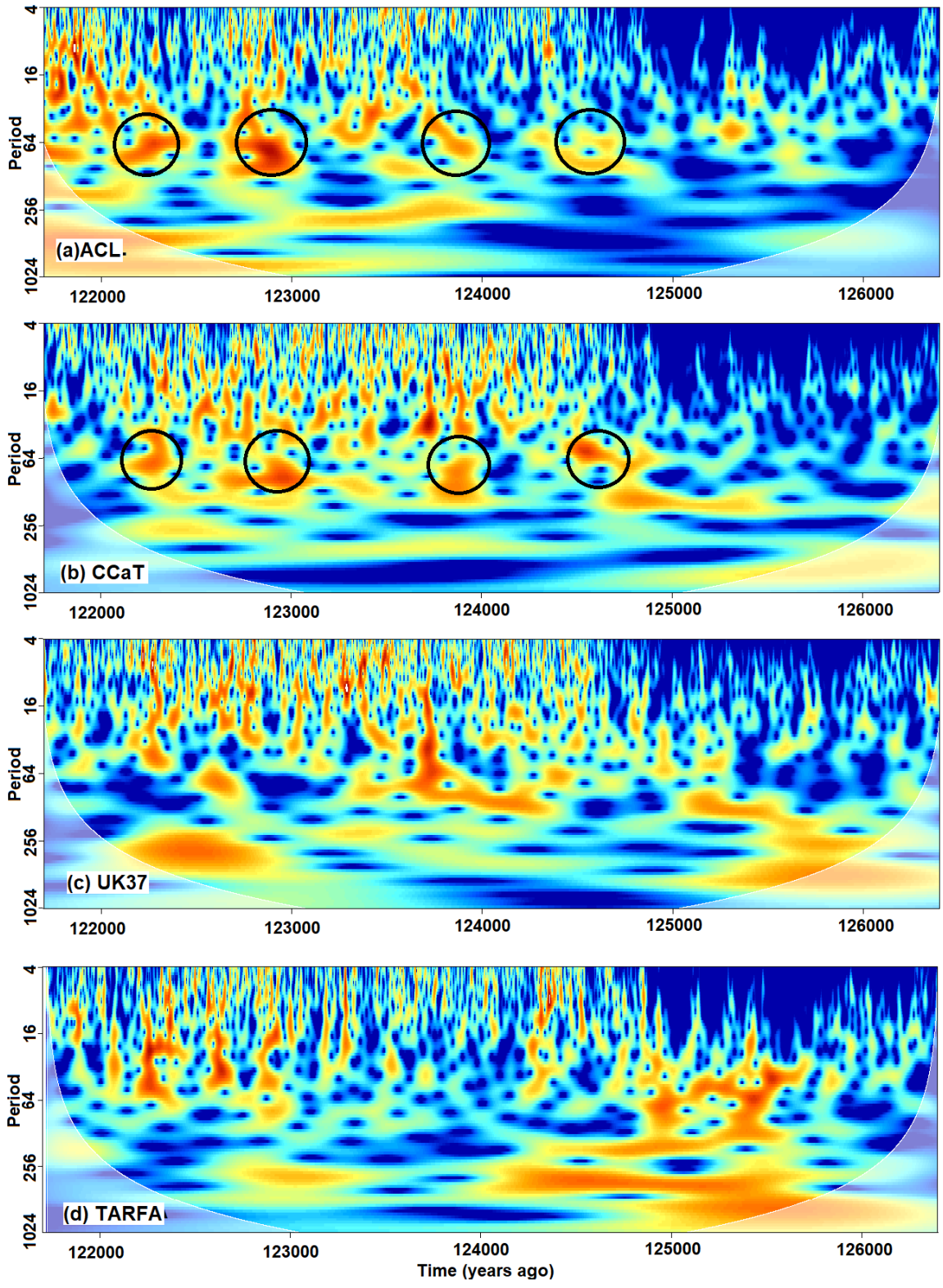

Figure 35: Wavelet analysis of biomarker proxies. Red and blue ends of the spectrum correspond to high and low spectral densities respectively. In-sync high spectral density encircled for ACL and CCaT.

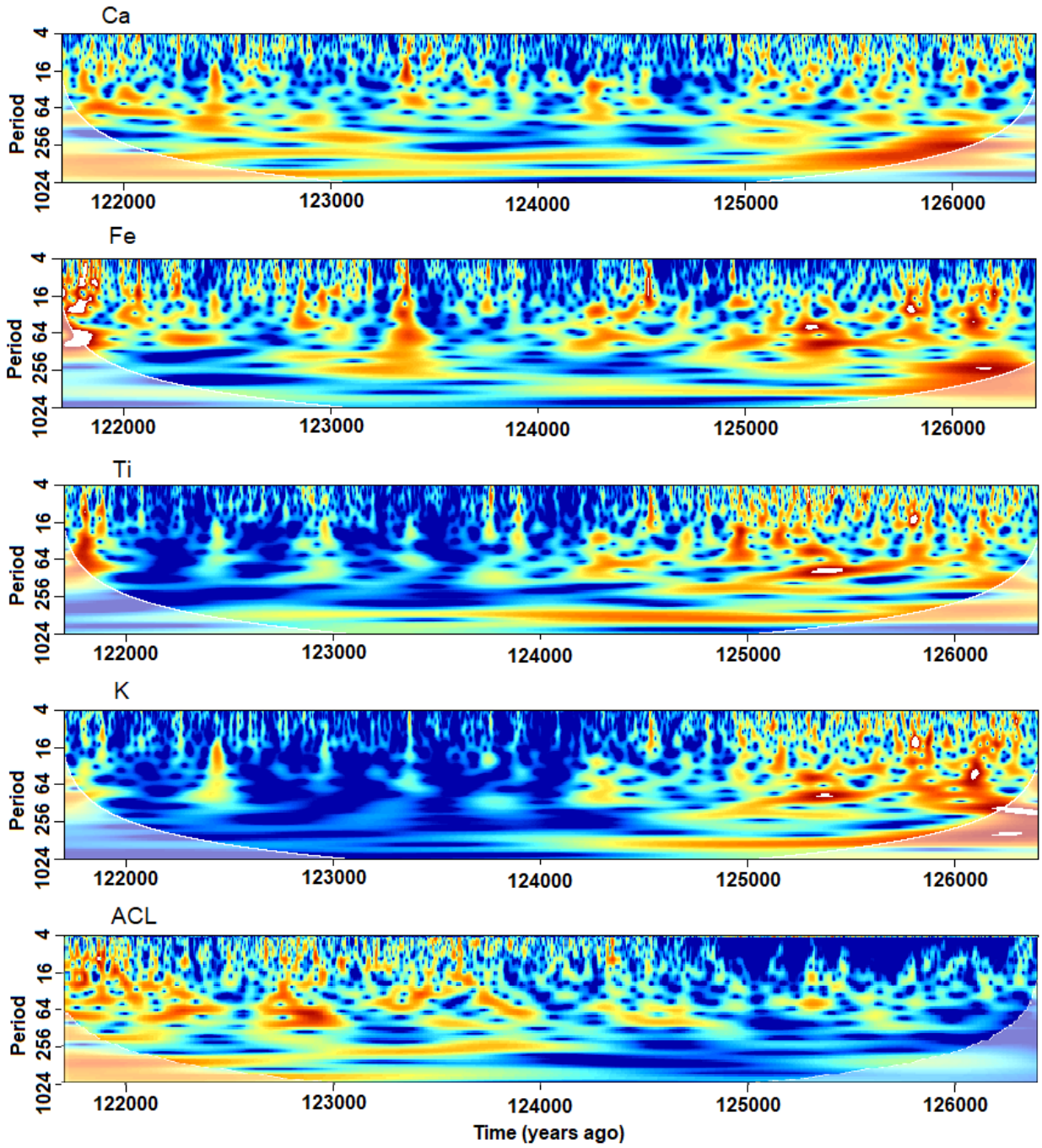

Figure 36: Wavelet analysis of elements Ca, Fe, Ti and K along with ACL values showing alternative high and low spectral density variation.

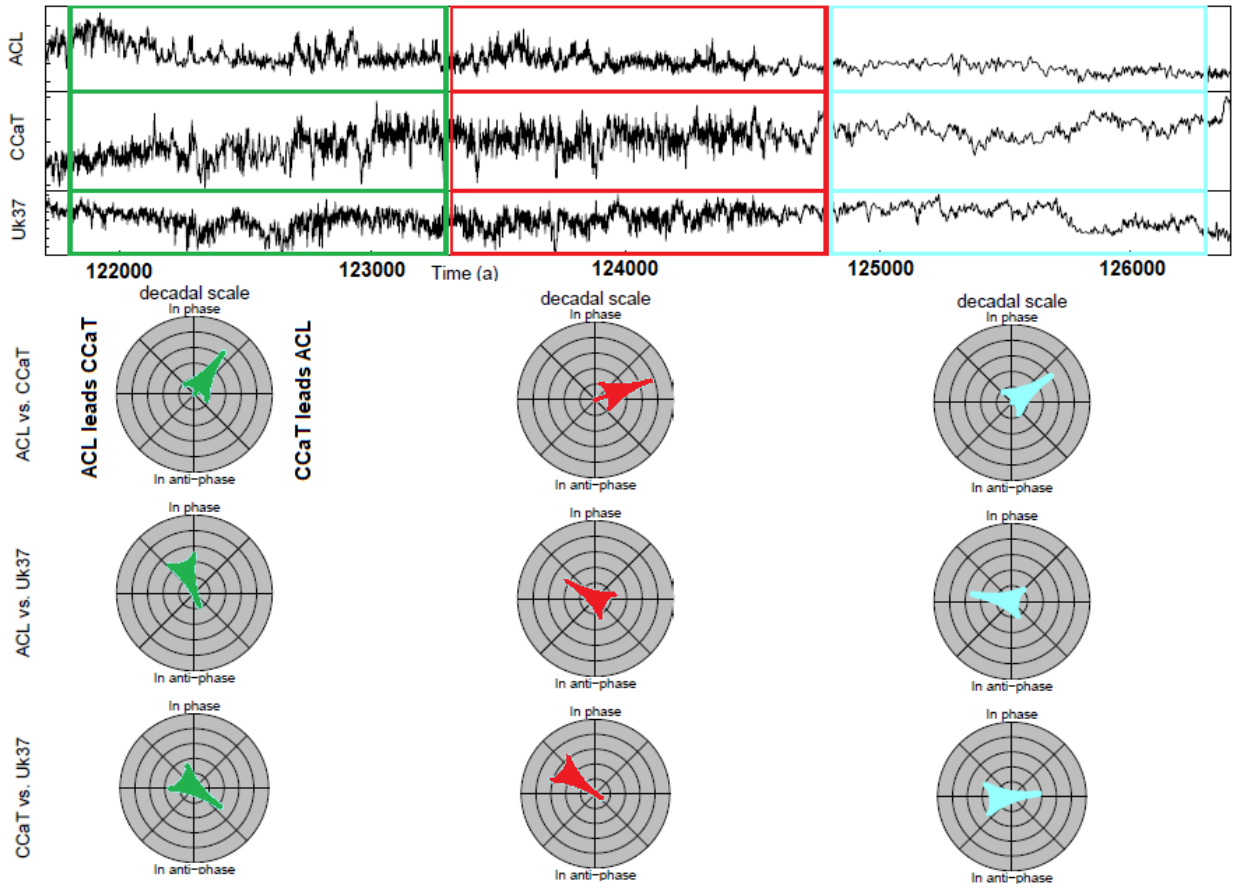

Figure 37: Phase analysis of various biomarkers in the decadal scale. The profiles of biomarkers are shown at the top of the figure.

4. CONCLUSION

Ultra-high resolution paleoclimate reconstruction of the climatic optimum during the last interglacial was successfully done using a comprehensive multi-proxy approach.

- The high-resolution FT-ICR-MS data was validated using the GC-FID and HPLC-MS methods, thus confirming the robustness of the FT data.
- Combined proxies like $U^{k'}_{37}$ indicated SST, elemental Br, $\delta^{18}O$ and isorenieratene from previous studies, have been used to establish the development of a deep chlorophyll maximum and intense water stratification during the early stages of sapropel deposition. Moreover, CCaT provides additional information concerning oxygen limitation due to severe water stratification conditions during monsoonal precipitation and sapropel deposition.

- Regional climate and vegetation changes as indicated by the average chain length of long-chain fatty acids transitioned from humid to drier conditions during sapropel deposition.
- Phase analysis between various detrital elements shows a variation in the contribution of sediments from northern and southern borderlands of the Eastern Mediterranean during different times of sapropel formation. Wavelet analysis of elemental data from Ca, Fe, K and Ti imply a coupling between low and mid-latitude hydrological changes during this time.
- Combined wavelet and phase analysis shows a pronounced multi-decadal oscillation in CCaT and ACL where changes in vegetational pattern and associated conditions lags the SST changes during monsoonal precipitation by around nine years.

Hence the study presented here provides a comprehensive multi-proxy analysis of this extreme climate event in the recent geologic history at an unprecedented detail.

REFERENCES

Agnihotri, R., Altabet, M.A., Herbert, T.D., Tierney, J.E., 2008. Subdecadally resolved paleoceanography of the Peru margin during the last two millennia. Geochemistry, Geophysics, Geosystems 9. doi:10.1029/2007GC001744

Alfken, S., Wörmer, L., Lipp, J.S., Wendt, J., Taubner, H., Schimmelmann, A., Hinrichs, K., 2019. Organic Geochemistry Micrometer scale imaging of sedimentary climate archives – Sample preparation for combined elemental and lipid biomarker analysis. Organic Geochemistry 127, 81–91.

Becker, K.W., Lipp, J.S., Versteegh, G.J.M., Wörmer, L., Hinrichs, K.U., 2015. Rapid and simultaneous analysis of three molecular sea surface temperature proxies and application to sediments from the Sea of Marmara. Organic Geochemistry 85, 42–53.

Berger, A., Loutre, M.F., 1991. Insolation values for the climate of the last 10 million years. Quaternary Science Reviews 10, 297–317.

Cane, T., Rohling, E.J., Kemp, A.E.S., Cooke, S., Pearce, R.B., 2002. High-resolution stratigraphic framework for Mediterranean sapropel S5: Defining temporal relationships between records of Eemian climate variability. Palaeogeography, Palaeoclimatology, Palaeoecology 183, 87–101.

Casford, J.S.L., Rohling, E.J., Abu-Zied, R.H., Fontanier, C., Jorissen, F.J., Leng, M.J., Schmiedl, G., Thomson, J., 2003. A dynamic concept for eastern Mediterranean circulation and oxygenation during sapropel formation. Palaeogeography, Palaeoclimatology, Palaeoecology 190, 103–119.

Conkright, M.E., Locarnini, R.A., Garcia, H.E., O'Brien, T.D., Boyer, T.P., Stephens, C., Antonov, J.I., 2002. World Ocean Atlas 2001: Objective analyses, data statistics, and figures CD-ROM documentation. National Oceanographic Data Center Internal Report (NOAA Atlas NESDIS) 17, 17.

Diefendorf, A.F., Freimuth, E.J., 2017. Extracting the most from terrestrial plant-derived n-alkyl lipids and their carbon isotopes from the sedimentary record: A review. Organic Geochemistry 103, 1–21.

Ehrmann, W., Schmiedl, G., Beuscher, S., Krüger, S., 2017. Intensity of african humid periods estimated from saharan dust fluxes. PLoS ONE 12, 1–18.

Evans, T.W., Lipp, J.S., Könneke, M., Elvert, M., Adhikari, R.R., Hinrichs, K.-U., Taubner, H., 2018. Lipid biosynthesis of Nitrosopumilus maritimus dissected by lipid specific radioisotope probing (lipid-RIP) under contrasting ammonium supply. Geochimica et Cosmochimica Acta 242, 51–63.

Grant, K.M., Ramsey, C.B., Satow, C., Bar-Matthews, M., Ayalon, A., Rohling, E.J., Roberts, A.P., Medina-Elizalde, M., 2012. Rapid coupling between ice volume and polar temperature over the past 150,000 years. Nature 491, 744–747.

H. Trauth, M., 2015. MATLAB® Recipes for Earth Sciences. Springer Berlin Heidelberg, Berlin, Heidelberg. doi:10.1007/978-3-662-46244-7

Hennekam, R., 2015. High-frequency climate variability in the late Quaternary eastern

Mediterranean Associations of Nile discharge and basin overturning circulation dynamics.

Hughen, A.K., Timothy, I.E., Li, X., and Matthew, M., 2004. Abrupt Tropical Vegetation Response to Rapid Climate Changes. Science 304, 1955.

Jolliffe, I.T., 2005. Principal Component Analysis, Second. ed. Springer, Aberdeen.

Kemp, A.E.S., Pearce, R.B., Koizumi, I., Pike, J., Rance, S.J., 1999. letters to nature corrections Experimental veri ® cation of the quasi-unit-cell model of quasicrystal structure In vivo regulation of axon extension and path ® nding by growth-cone calcium transients Extreme Th1 bias of invariant V a 24J a Q Tcells in typ 399, 350–355.

Kemp, A.E.S., Villareal, T.A., 2013. High diatom production and export in stratified waters - A potential negative feedback to global warming. Progress in Oceanography 119, 4–23.

Kim, J.-H., Helmke, P., Rampen, S., Marino, G., Hopmans, E.C., Buscail, R., Sangiorgi, F., Rodrigo-Gámiz, M., Sinninghe Damsté, J.S., Huguet, C., Schouten, S., Pross, J., Middelburg, J.B.M., 2014. Influence of deep-water derived isoprenoid tetraether lipids on the TEX86H paleothermometer in the Mediterranean Sea. Geochimica et Cosmochimica Acta 150, 125–141.

Knapp, 1980. Handbook of analytical derivatization reactions, Journal of Pharmaceutical Sciences. John Wiley & Sons, Ltd. doi:10.1002/jps.2600690549

M ETEOR -Berichte 03-1 Ostatlantik-Mittelmeer-Schwarzes Meer, 2003.

Marino, G., Rohling, E.J., Rijpstra, W.I.C., Sangiorgi, F., Schouten, S., Sinninghe Damsté, J.S., 2007. Aegean sea as driver of hydrographic and ecological changes in the eastern Mediterranean. Geology 35, 675–678.

Martinez-Ruiz, F., Kastner, M., Gallego-Torres, D., Rodrigo-Gámiz, M., Nieto-Moreno, V., Ortega-Huertas, M., 2015. Paleoclimate and paleoceanography over the past 20,000yr in the Mediterranean Sea Basins as indicated by sediment elemental proxies. Quaternary Science Reviews 107, 25–46.

Meyers, P.A., 1997. Organic geochemical proxies of paleoceanographic, paleolimnologic, and paleoclimatic processes. Organic Geochemistry 27, 213–250.

Moller, T., 2012. Formation and paleoclimatic interpretation of a continuously laminated sapropel S 5 : a window to the climate variability during the Eemian interglacial in the Eastern Mediterranean.

Morel, F.M.M., Milligan, A.J., Saito, M.A., 2003. Marine Bioinorganic Chemistry: The Role of Trace Metals in the Oceanic Cycles of Major Nutrients, in: Treatise on Geochemistry. Elsevier, pp. 113–143.

Müller, P.J., Kirst, G., Ruhland, G., von Storch, I., Rosell-Melé, A., 1998. Calibration of the alkenone paleotemperature index U37K′ based on core-tops from the eastern South Atlantic and the global ocean (60°N-60°S). Geochimica et Cosmochimica Acta 62, 1757–1772.

Percival, D.B., Walden, A.T., 1993. Spectral Analysis for Physical Applications. Cambridge University Press, Cambridge. doi:10.1017/CBO9780511622762

Poynter, J.G., Farrimond, P., Robinson, N., Eglinton, G., 1989. Aeolian-Derived Higher Plant Lipids in the Marine Sedimentary Record: Links with Palaeoclimate, in: Paleoclimatology and Paleometeorology: Modern and Past Patterns of Global Atmospheric Transport. Springer Netherlands, Dordrecht, pp. 435–462.

Qin, W., Carlson, L.T., Armbrust, E.V., Stahl, D.A., Ingalls, A.E., Devol, A.H., Moffett, J.W., 2015. Confounding effects of oxygen and temperature on the TEX 86 signature of marine Thaumarchaeota. Proceedings of the National Academy of Sciences 112, 10979–10984.

Rohling, E.J., Abu-Zied, R.H., Casford, J.S.L., Hayes, A., Hoogakker, B.A.A., 2009. The physical geography of the Mediterranean. Oxford University Press.

Rohling, E.J., Cane, T.R., Bouloubassi, I., Kemp, A.E.S., Kroon, D., Schiebel, R., Lorre, A., Emeis, K.C., Cooke, S., Jorissen, F.J., Sprovieri, M., 2002. African monsoon variability during the previous interglacial maximum. Earth and Planetary Science Letters 202, 61–75.

Rohling, E.J., Gieskes, W.W.C., 1989. Late Quaternary changes in Mediterranean intermediate water density and formation rate. Paleoceanography 4, 531–545.

Rohling, E.J., Marino, G., Grant, K.M., 2015. Mediterranean climate and oceanography, and the periodic development of anoxic events (sapropels). Earth-Science Reviews 143, 62–97.

Rossignol-Strick, M., Nesteroff, W., Olive, P., Vergnaud-Grazzini, C., 1982. After the deluge: Mediterranean stagnation and sapropel formation. Nature 295, 105–110.

Sangiorgi, F., Maffioli, P., Capotondi, L., Morigi, C., Negri, A., Giunta, S., Dinelli, E., Emeis, K.-C., Corselli, C., Principato, M.S., 2005. Geochemical and micropaleontological characterisation of a Mediterranean sapropel S5: A case study from core BAN89GC09 (south of Crete). Palaeogeography, Palaeoclimatology, Palaeoecology 235, 192–207.

Scafetta, N., 2014. Multi-scale dynamical analysis (MSDA) of sea level records versus PDO, AMO, and NAO indexes. Climate Dynamics 43, 175–192.

Schouten, S., Hopmans, E.C., M, E.S., 2002. Distributional variations in marine crenarchaeotal membrane lipids: a new tool for reconstructing ancient sea water temperatures? 204, 1–10.

Struck, U., Emeis, K.-C., Krom, M.D., Rau, G.H., Voß, M., 2002. Biological productivity during sapropel S5 formation in the Eastern Mediterranean Sea: evidence from stable isotopes of nitrogen and carbon. Geochimica et Cosmochimica Acta 65, 3249–3266.

Thomson, J., Croudace, I.W., Rothwell, R.G., 2006. A geochemical application of the ITRAX scanner to a sediment core containing eastern Mediterranean sapropel units. Geological Society, London, Special Publications 267, 65–77.

Toucanne, S., Angue Minto'o, C.M., Fontanier, C., Bassetti, M.A., Jorry, S.J., Jouet, G., 2015. Tracking rainfall in the northern Mediterranean borderlands during sapropel deposition. Quaternary Science Reviews 129, 178–195.

Tzedakis, P.C., Crucifix, M., Mitsui, T., Wolff, E.W., 2017. A simple rule to determine which insolation cycles lead to interglacials. Nature 542, 427–432.

van Santvoort, P.J.M., de Lange, G.J., Langereis, C.G., Dekkers, M.J., Paterne, M., 1997. Geochemical and paleomagnetic evidence for the occurrence of "missing"sapropels in eastern Mediterranean sediements. Paleoceanography 12, 773–786.

Volkman, J.K., Gillan, F.T., Bavor, H.J., Johns, R.B., Perry, G.J., 2003. Microbial lipids of an intertidal sediment—I. Fatty acids and hydrocarbons. Geochimica et Cosmochimica Acta 44, 1133–1143.

Weldeab, S., Emeis, K.C., Hemleben, C., Schmiedl, G., Schulz, H., 2003. Spatial productivity variations during formation of sapropels S5 and S6 in the Mediterranean Sea: Evidence from Ba contents. Palaeogeography, Palaeoclimatology, Palaeoecology 191, 169–190.

Wörmer, L., Elvert, M., Fuchser, J., Lipp, J.S., Buttigieg, P.L., Zabel, M., Hinrichs, K.-U., 2014. Ultra-high-resolution paleoenvironmental records via direct laser-based analysis of lipid biomarkers in sediment core samples. Proceedings of the National Academy of Sciences 111, 15669–15674.

Wu, J., Filippidi, A., Davies, G.R., de Lange, G.J., 2018. Riverine supply to the eastern Mediterranean during last interglacial sapropel S5 formation: A basin-wide perspective. Chemical Geology 485, 74–89.

Zhang, R., Delworth, T.L., 2006. Impact of Atlantic multidecadal oscillations on India/Sahel rainfall and Atlantic hurricanes. Geophysical Research Letters 33, 1–5.

Ziegler, M., Jilbert, T., De Lange, G.J., Lourens, L.J., Reichart, G.J., 2008. Bromine counts from XRF scanning as an estimate of the marine organic carbon content of sediment cores. Geochemistry, Geophysics, Geosystems 9, 1–6.

APPENDIX

(I) Tables:

Table A1: Sample extraction details

Sample range (cm)	Mean depth (mm)	Sediment weight (g)	% TLE used in GC-FID	% TLE used in LC
0-1	3555.1	0.87	8	0.5
9.5-10.5	3644	0.27	8	0.005
19.5-20.5	3744	0.17	8	0.005
29.5-30.5	3844	0.19	8	0.005
39.5-40.5	3944	0.15	8	0.005
50-52	4045	0.11	8	0.005
52-53	4060	0.10	8	0.5
53-55	4075	0.12	8	0.5
59.5-60.5	4144	0.13	8	0.005
69.5-70.5	4244	0.14	8	0.5
79.5-80.5	4344	0.31	8	0.005
89.5-90.5	4444	0.61	8	0.002
95-96	4499	0.76	8	0.5
45-45.5	3996.5	0.11	8	0.5
45.5-46	4001.5	0.10	8	0.5
46-46.5	4006.5	0.07	8	0.5
46.5-47	4011.5	0.08	8	0.5
47-47.5	4016.5	0.11	8	0.5
47.5-48	4021.5	0.11	8	0.5
48-48.5	4026.5	0.10	8	0.5
48.5-49	4031.5	0.10	8	0.5
49-49.5	4036.5	0.07	8	0.5
49.5-50	4041.5	0.14	8	0.005

(II) Figures:

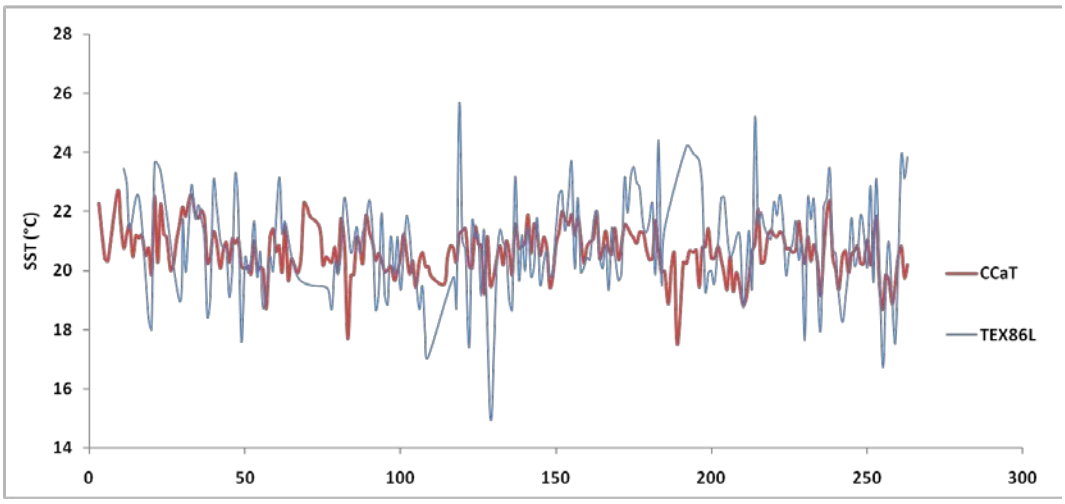

Figure A1: TEX_{86}^{L}= log(GDGT-2/(GDGT-1+GDGT-2+GDGT-3) and SST= 67.5* TEX_{86}^{L} +46.9 (Kim et al., 2014). The x-axis is length or depth, where 250 units = 5cm (or 1 unit= 0.02mm – resolution of measurement).

Since the percentage of successful spectra was low for TEX_{86}^{L} (around 17-40%), it wasn't used as a proxy in this study.

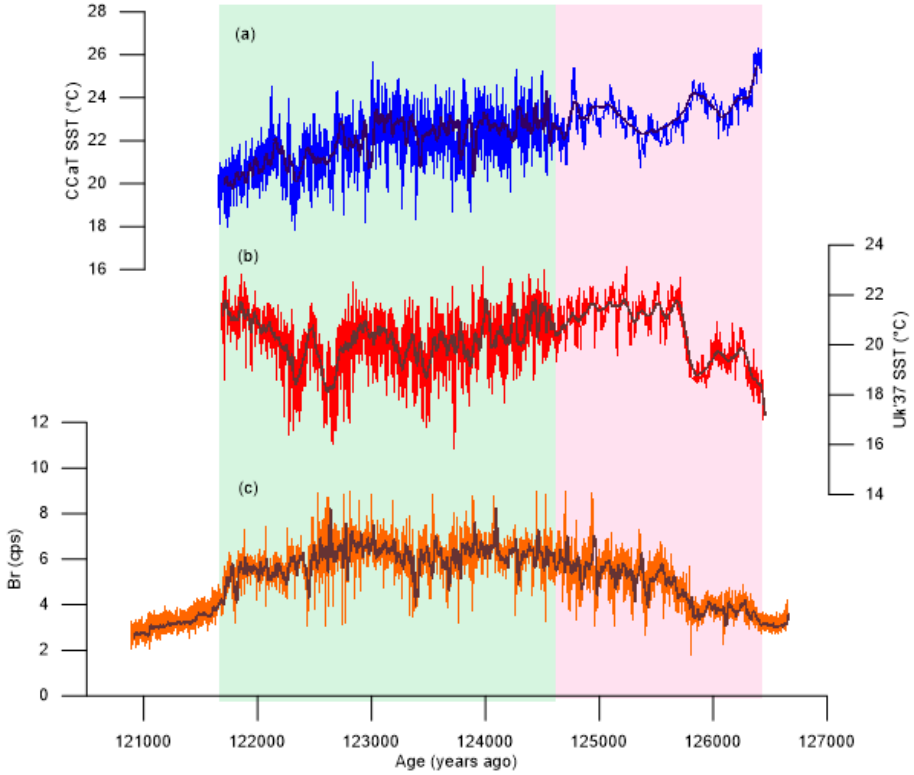

Figure A2: Increased organic matter within the sapropel- (a) CCaT based SST (b) $U^{k'}_{37}$ based SST (c) Br profile indicating MOC.

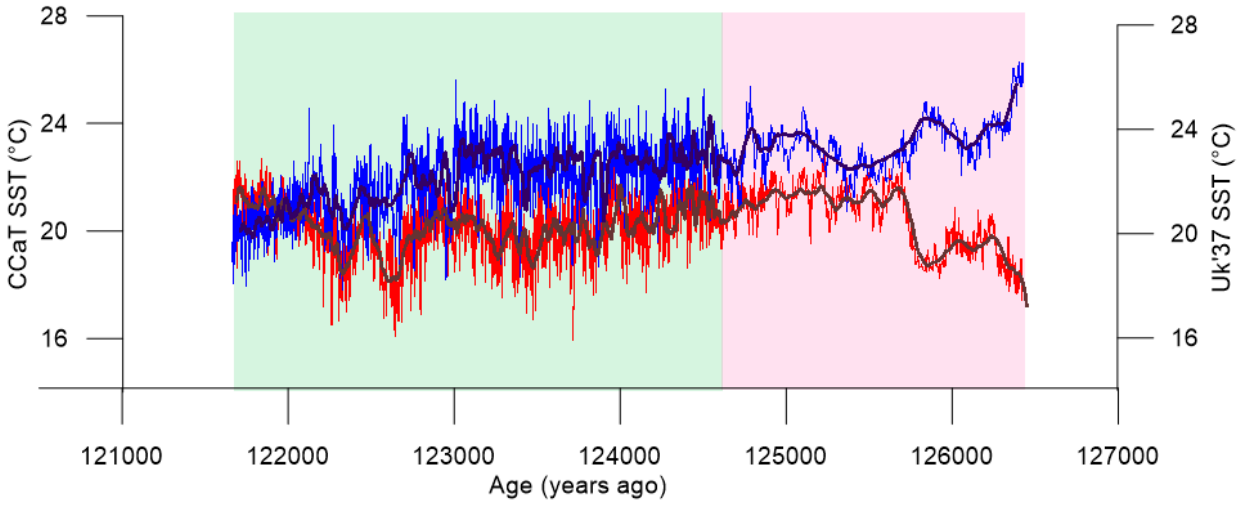

Figure A3: Comparing $U^{k'}_{37}$ (red) and CCaT(blue) based SSTs.

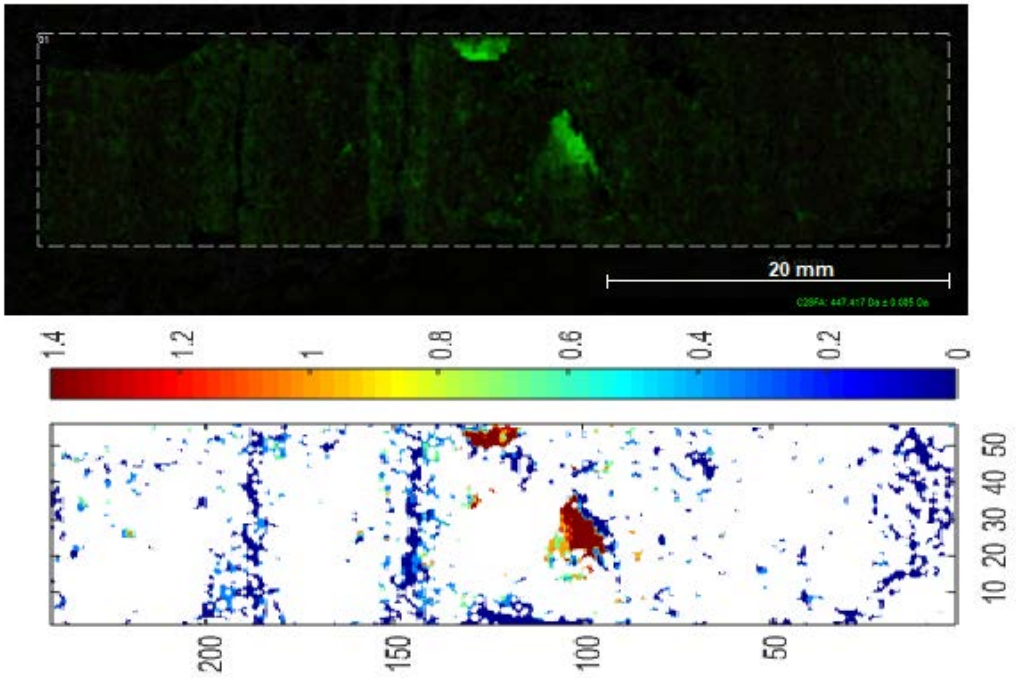

Figure A4: Anomalous region of high signal values around 125.7 kyr shown in the 5 cm section measured. The top figure indicates the distribution of C_{28} fatty acid, as a sample image on the thin-section slide. The bottom figure corresponds to the MSI of TARFA values generated from MATLAB.

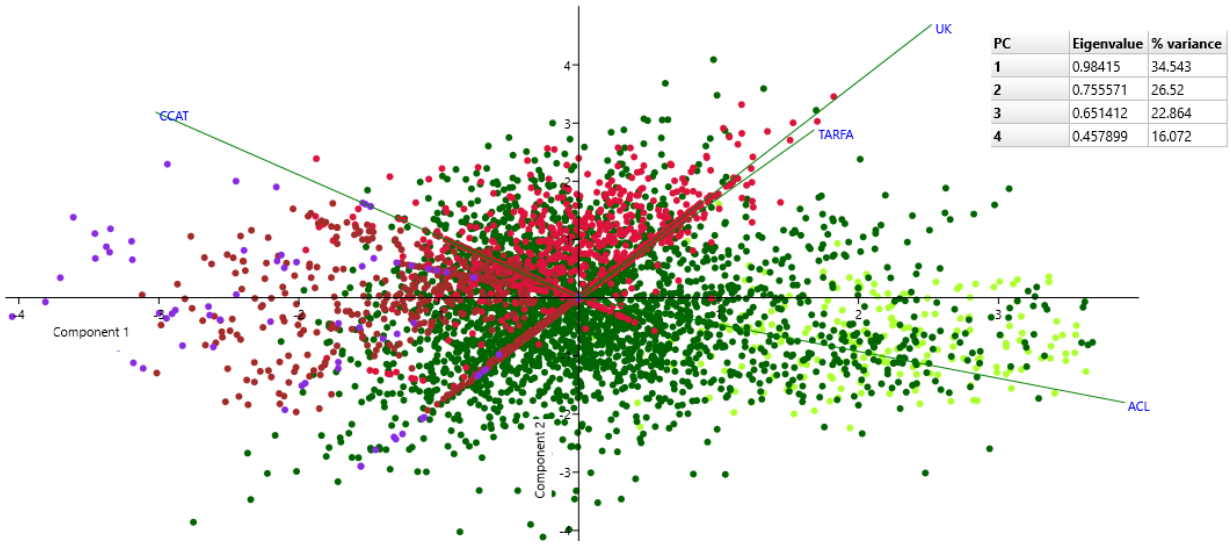

Figure A5: PCA analysis on biomarkers with their eigenvalues and % of the variance

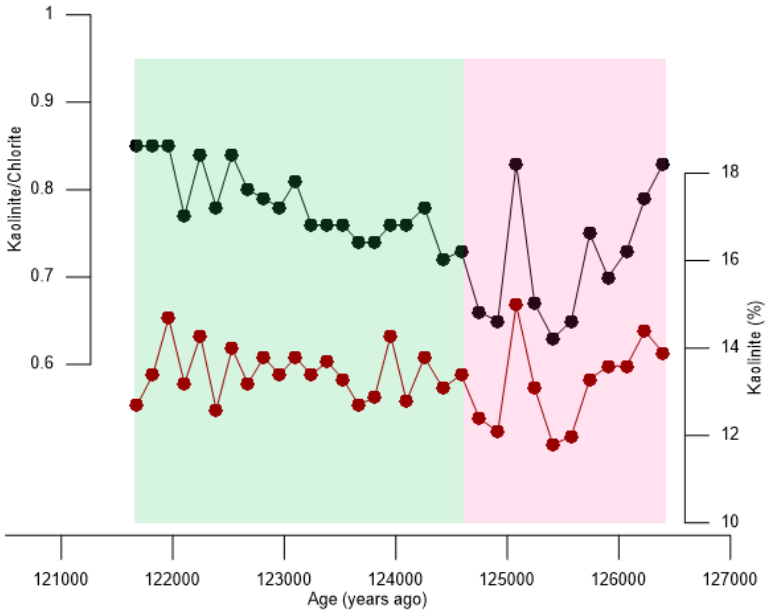

Figure A6: Kaolinite/Chlorite ratio and Kaolinite (%) for sapropel S5 from clay mineral flux (Ehrmann et al., 2017)

(III) Programming scripts:

R-scripts used for Spectral and Phase Analysis (Credits: David De Vleeschouwer)

```
# First we make sure the working environment is empty... No left-overs from previous work
rm(list = ls())
```

```
# We set the working directory.
setwd("/Users/pdoc3/Documents/Sapropel MIS 5/")

# We load the R packages from which we want to use functions
library(astrochron)
library(biwavelet)
library(RColorBrewer)
library(colorRamps)
library(IRISSeismic)
library(plotrix)
library(shape)

# We read the datasets
ACL <- read.csv("Sapropel_ACL.csv", header = T)
colnames(ACL) <- c("Age (a)", "ACL")

CCAT <- read.csv("Sapropel_CCAT.csv", header = T)
colnames(CCAT) <- c("Age (a)", "CCaT (SST ??C)")

Uk37 <- read.csv("Sapropel_Uk37.csv", header = T)
colnames(Uk37) <- c("Age (a)", "Uk37 (SST ??C)")

##############################################################################
# We generate multi-taper method power spectra of the datasets.
##############################################################################
ACL_i <- linterp(ACL, dt = 0.5, genplot = F) # In order to do so, we first need to interpolate the
series to equally-spaced intervals. Median sampling interval of ACL is 0.479, therefore I chose
to interpolate at 0.5 yr intervals
ACL_i <- noLow(ACL_i, smooth = 0.25) # It is also important to remove the linear trend.
Calculating a spectrum without detrending generates in a big peak at the lowest-possible
frequency (i.e. the Rayleigh frequency)
ACL_i[,2]=ACL_i[,2]/sd(ACL_i[,2]) # Normalizing the proxy values
ACL_mtm <- mtm(ACL_i, ntap = 5, genplot = F, output = 1) # Multitaper method with three
DPSS tapers

CCAT_i <- linterp(CCAT, dt = 0.6, genplot = F) # Median sampling interval is 0.608 yr, therefore
I chose to interpolate at 0.6 yr intervals
CCAT_i <- noLow(CCAT_i, smooth = 0.25)
CCAT_i[,2]=CCAT_i[,2]/sd(CCAT_i[,2])
CCAT_mtm <- mtm(CCAT_i, ntap = 5, genplot = F, output = 1)

Uk37_i <- linterp(Uk37, dt = 0.5, genplot = F) # Median sampling interval is 0.51 yr, therefore I
chose to interpolate at 0.5 yr intervals
Uk37_i <- noLow(Uk37_i, smooth = 0.25)
Uk37_i[,2]=Uk37_i[,2]/sd(Uk37_i[,2])
Uk37_mtm <- mtm(Uk37_i, ntap = 5, genplot = F, output = 1)

# Plotting of MTM spectra
dev.off()
par(mar = c(4, 4, 1, 1), oma = c(0, 0, 0, 0)) # Setting margins and space inbetween panels
```

```
layout(matrix(c(1,2,3), 3, 1, byrow = TRUE), heights=c(1,1,1))

plot(1/ACL_mtm$Frequency, ACL_mtm$Power, type = "l", log = "xy", xaxs = "i", xlab = "", ylab =
"", xlim = c(5,5000), ylim = c(1e-5,2e-2))
lines(1/ACL_mtm$Frequency, ACL_mtm$AR1_99_power, col = "red")
mtext(side = 1, "Period (year)",line=2.5, cex=1.0)
mtext(side = 2, "Spectral Power",line=2.5, cex=1.0)
text(10, 0.015, "(a) ACL", cex = 2.5)
text(3000,0.015, "99% conf. lim.", col = "red", cex = 1.2)

plot(1/CCAT_mtm$Frequency, CCAT_mtm$Power, type = "l", log = "xy", xaxs = "i", xlab = "",
ylab = "", xlim = c(5,5000), ylim = c(1e-5,2e-2))
lines(1/CCAT_mtm$Frequency, CCAT_mtm$AR1_99_power, col = "red")
mtext(side = 1, "Period (year)",line=2.5, cex=1.0)
mtext(side = 2, "Spectral Power",line=2.5, cex=1.0)
text(10, 0.005, "(b) CCaT", cex = 2.5)
text(3000,0.006, "99% conf. lim.", col = "red", cex = 1.2)

plot(1/Uk37_mtm$Frequency, Uk37_mtm$Power, type = "l", log = "xy", xaxs = "i", xlab = "", ylab
= "", xlim = c(5,5000),ylim = c(1e-5,2e-2))
lines(1/Uk37_mtm$Frequency, Uk37_mtm$AR1_99_power, col = "red")
mtext(side = 1, "Period (year)",line=2.5, cex=1.0)
mtext(side = 2, "Spectral Power",line=2, cex=1.0)
text(10, 0.015, "(c) Uk37", cex = 2.5)
text(3000,0.01, "99% conf. lim.", col = "red", cex = 1.2)

##############################################################################
# We generate wavelet transforms of the datasets.
##############################################################################
dt = 0.5
ACL_wavelet=wt(ACL_i, pad = T, dt = dt, dj = 1/12, s0 = 2 * dt, J1 = NULL,max.scale = NULL,
mother = "morlet", param = -1, lag1 = NULL,sig.level = 0.99, sig.test = 0, do.sig = F)
dt = 0.6
CCAT_wavelet=wt(CCAT_i, pad = T, dt = dt, dj = 1/12, s0 = 2 * dt, J1 = NULL,max.scale =
NULL, mother = "morlet", param = -1, lag1 = NULL,sig.level = 0.99, sig.test = 0, do.sig = F)
dt = 0.5
Uk37_wavelet=wt(Uk37_i, pad = T, dt = dt, dj = 1/12, s0 = 2 * dt, J1 = NULL,max.scale = NULL,
mother = "morlet", param = -1, lag1 = NULL,sig.level = 0.99, sig.test = 0, do.sig = F)

a=matlab.like(64)

dev.off()
par(mar = c(4, 4, 1, 1), oma = c(0, 0, 0, 0)) # Setting margins and space inbetween panels
layout(matrix(c(1,2,3), 3, 1, byrow = TRUE), heights=c(1,1,1))
plot.biwavelet(ACL_wavelet, fill.cols = a, plot.cb = F, ylim = c(4, 1024), zlim = c(4,12), xlim =
c(121700, 126400)) # Plotting wavelets takes a long time!
plot.biwavelet(CCAT_wavelet,fill.cols = a, plot.cb = F, ylim = c(4, 1024), zlim = c(4,12), xlim =
c(121700, 126400))
plot.biwavelet(Uk37_wavelet,fill.cols = a, plot.cb = F, ylim = c(4, 1024), zlim = c(4,12), xlim =
c(121700, 126400))
```

```
################################################################################
# Bandpass filtering
################################################################################

ACL_bandpass = bandpass(ACL_i, flow = 1/50, fhigh = 1/70, xmax = 1/20)
CCAT_bandpass = bandpass(CCAT_i, flow = 1/50, fhigh = 1/70, xmax = 1/20)
Uk37_bandpass = bandpass(Uk37_i, flow = 1/50, fhigh = 1/70, xmax = 1/20)

dev.off()
par(mar = c(4, 4, 1, 1), oma = c(0, 0, 0, 0)) # Setting margins and space inbetween panels
layout(matrix(c(1,2,3), 3, 1, byrow = TRUE), heights=c(1,1,1))
plot(ACL_bandpass,type = "l", xlab = "Time (a)", ylab = "Bandpass filter")
lines(CCAT_bandpass, col = "red")
text(122000,-1.25, "ACL", col = "black", cex = 2)
text(122000,-1.5, "CCaT", col = "red", cex = 2)

plot(ACL_bandpass, type="l",xlab = "Time (a)", ylab = "Bandpass filter")
lines(Uk37_bandpass, col = "blue")
text(122000,-1.25, "ACL", col = "black", cex = 2)
text(122000,-1.5, "Uk37", col = "blue", cex = 2)

plot(CCAT_bandpass, type = "l", col = "red",xlab = "Time (a)", ylab = "Bandpass filter")
lines(Uk37_bandpass, col = "blue")
text(122000,-1.25, "CCaT", col = "red", cex = 2)
text(122000,-1.5, "Uk37", col = "blue", cex = 2)
################################################################################
# Phase analysis
################################################################################
f_year_low=1/14
f_year_high=1/7
f_deca_low=1/70
f_deca_high=1/50
f_cent_low=1/800
f_cent_high=1/400

T1_all = seq(121800,124800 , by = 1500)
T2_all = seq(123300,126300, by = 1500)

phase_year_1=matrix(nrow = 3, ncol = 2)
phase_year_1[,1]=seq(122550,125550, by = 1500)
phase_year_2=phase_year_1
phase_year_3=phase_year_1
phase_deca_1=phase_year_1
phase_deca_2=phase_year_1
phase_deca_3=phase_year_1
phase_cent_1=phase_year_1
phase_cent_2=phase_year_1
phase_cent_3=phase_year_1

##### Start loop ----
for (i in 1:length(T1_all)){
```

```
T1=T1_all[i]
T2=T2_all[i]

idx1=which(ACL[,1]<T2 & ACL[,1]>T1)
idx2=which(CCAT[,1]<T2 & CCAT[,1]>T1)
idx3=which(Uk37[,1]<T2 & Uk37[,1]>T1)
ACL_win1=astrochron::detrend(ACL[idx1,c(1,2)], genplot = F)
CCAT_win1=astrochron::detrend(CCAT[idx2,c(1,2)], genplot = F)
Uk37_win1=astrochron::detrend(Uk37[idx3,c(1,2)], genplot = F)

res_ACL=length( ACL_win1[,1])/(T2-T1)
res_CCAT=length(CCAT_win1[,1])/(T2-T1)
res_Uk37=length(Uk37_win1[,1])/(T2-T1)
dt = signif(1/min(res_Uk37,res_CCAT,res_ACL),2)
time = seq(from = T1, to = T2, by = dt)

ACL_win1=approx(ACL[,1], ACL[,2], xout = time)$y
CCAT_win1=approx(CCAT[,1], CCAT[,2], xout = time)$y
Uk37_win1=approx(Uk37[,1], Uk37[,2], xout = time)$y

ACL_win1=ts(ACL_win1, frequency = 1/dt, start = T1)
CCAT_win1=ts(CCAT_win1, frequency = 1/dt, start = T1)
Uk37_win1=ts(Uk37_win1, frequency = 1/dt, start = T1)

win1=ts.union(ACL_win1,CCAT_win1)
win2=ts.union(ACL_win1, Uk37_win1)
win3=ts.union(CCAT_win1, Uk37_win1)

DF1 <- crossSpectrum(win1, spans = c(3,5))
DF2 <- crossSpectrum(win2, spans=c(3,5))
DF3 <- crossSpectrum(win3, spans=c(3,5))

# yearly scale ----
idx_year=which(DF1$freq < f_year_high & DF1$freq > f_year_low)

# ACL vs. CCAT
coh_year_1=max(DF1$coh[idx_year])
idx_coh=which(DF1$coh == coh_year_1)
phase_year_1[i,2]=DF1$phase[idx_coh]
# convert polar to cartesian
x_year_1 = (coh_year_1) * cos(phase_year_1[i,2])
y_year_1 = (coh_year_1) * sin(phase_year_1[i,2])

# ACL vs. Uk37
coh_year_2=max(DF2$coh[idx_year])
idx_coh=which(DF2$coh == coh_year_2)
phase_year_2[i,2]=DF2$phase[idx_coh]
# convert polar to cartesian
x_year_2 = (coh_year_2) * cos(phase_year_2[i,2])
y_year_2 = (coh_year_2) * sin(phase_year_2[i,2])
```

```
# CCAT vs. Uk37
coh_year_3=max(DF3$coh[idx_year])
idx_coh=which(DF3$coh == coh_year_3)
phase_year_3[i,2]=DF3$phase[idx_coh]
# convert polar to cartesian
x_year_3 = (coh_year_3) * cos(phase_year_3[i,2])
y_year_3 = (coh_year_3) * sin(phase_year_3[i,2])

# decadal scale ----
idx_deca=which(DF1$freq < f_deca_high & DF1$freq > f_deca_low)

# ACL vs. CCAT
coh_deca_1=max(DF1$coh[idx_deca])
idx_coh=which(DF1$coh == coh_deca_1)
phase_deca_1[i,2]=DF1$phase[idx_coh]
# convert polar to cartesian
x_deca_1 = (coh_deca_1) * cos(phase_deca_1[i,2])
y_deca_1 = (coh_deca_1) * sin(phase_deca_1[i,2])

# ACL vs. Uk37
coh_deca_2=max(DF2$coh[idx_deca])
idx_coh=which(DF2$coh == coh_deca_2)
phase_deca_2[i,2]=DF2$phase[idx_coh]
# convert polar to cartesian
x_deca_2 = (coh_deca_2) * cos(phase_deca_2[i,2])
y_deca_2 = (coh_deca_2) * sin(phase_deca_2[i,2])

# CCAT vs. Uk37
coh_deca_3=max(DF3$coh[idx_deca])
idx_coh=which(DF3$coh == coh_deca_3)
phase_deca_3[i,2]=DF3$phase[idx_coh]
# convert polar to cartesian
x_deca_3 = (coh_deca_3) * cos(phase_deca_3[i,2])
y_deca_3 = (coh_deca_3) * sin(phase_deca_3[i,2])

# centennial scale ----
idx_cent=which(DF1$freq < f_cent_high & DF1$freq > f_cent_low)

# ACL vs. CCAT
coh_cent_1=max(DF1$coh[idx_cent])
idx_coh=which(DF1$coh == coh_cent_1)
phase_cent_1[i,2]=DF1$phase[idx_coh]
# convert polar to cartesian
x_cent_1 = (coh_cent_1) * cos(phase_cent_1[i,2])
y_cent_1 = (coh_cent_1) * sin(phase_cent_1[i,2])

# ACL vs. Uk37
coh_cent_2=max(DF2$coh[idx_cent])
idx_coh=which(DF2$coh == coh_cent_2)
phase_cent_2[i,2]=DF2$phase[idx_coh]
```

```
# convert polar to cartesian
x_cent_2 = (coh_cent_2) * cos(phase_cent_2[i,2])
y_cent_2 = (coh_cent_2) * sin(phase_cent_2[i,2])

# CCAT vs. Uk37
coh_cent_3=max(DF3$coh[idx_cent])
idx_coh=which(DF3$coh == coh_cent_3)
phase_cent_3[i,2]=DF3$phase[idx_coh]
# convert polar to cartesian
x_cent_3 = (coh_cent_3) * cos(phase_cent_3[i,2])
y_cent_3 = (coh_cent_3) * sin(phase_cent_3[i,2])
### PLOT MASTER -----

par(mar = c(2.5, 5, 1, 1), oma = c(0, 0, 0, 0))
layout(matrix(c(1,1,1,2,2,2,3,3,3,4,5,6,7,8,9,10,11,12), 6, 3, byrow = TRUE),
heights=c(1,1,1,2,2,2))

par(mar=c(0,5,1,1))
plot(ACL[,1], ACL[,2], type = "l", xaxs = "i", yaxs = "i", xlab = "", ylab = "", tck=0.05, mgp = c(3,
0.2, 0), xaxt = 'n', xlim = c(121700,126400), ylim = c(24.7, 25.6))
mtext(side = 2, "ACL",line=2, cex=1.0)
rect(T1, 24.7 , T2, 25.6, lwd = 3, border = "darkslategray1")

par(mar=c(0,5,0,1))
plot(CCAT[,1], CCAT[,2], type = "l", xaxs = "i", yaxs = "i", xlab = "", ylab = "", tck=0.05, mgp =
c(3, 0.2, 0), xaxt = 'n', xlim = c(121700,126400), ylim = c(17.5,26.5))
mtext(side = 2, "CCAT (??C)",line=2, cex=1.0)
rect(T1, 17.5 , T2, 26.5, lwd = 3, border = "darkslategray1")

par(mar=c(2.5,5,0,1))
plot(Uk37[,1], Uk37[,2], type = "l", xaxs = "i", yaxs = "i", xlab = "", ylab = "", xlim =
c(121700,126400), tck=0.05, mgp = c(3, 0.2, 0), ylim = c(16,23.5))
mtext(side = 1, "Time (a)",line=1.5, cex=1.0)
mtext(side = 2, "Uk37 (??C)",line=2, cex=1.0)
rect(T1, 16 , T2, 23.5, lwd = 3, border = "darkslategray1")

# Plot ACL vs. CCat ----
par(mar=c(0.5,0.5,2.5,0.5))
plot(x_year_1,y_year_1, bty="n", axes = F, type = 'p', xlim = c(-1, 1), ylim = c(-1,1),xaxs="i",
yaxs="i", asp = 1, col="darkslategray1", xlab = "", ylab = "")
draw.circle(x = c(0,0,0,0,0),y = c(0,0,0,0,0), radius = c(1,0.8, 0.6, 0.4, 0.2), col = "grey")
segments(-1,0,1,0)
segments(0,-1,0,1)
segments(cos(pi/4),cos(pi/4),sin(-pi/4),sin(-pi/4))
segments(-cos(pi/4),cos(-pi/4),sin(pi/4),sin(-pi/4))
Arrows(0,0,x_year_1,y_year_1, code = 2, col = "darkslategray1", lwd = 5,
arr.type="curved",arr.adj = 1)
mtext(side = 2, "ACL vs. CCaT",line = -3)
mtext(side = 3, "yearly scale",line = 1)
mtext(side = 3, "In phase", line = 0, cex = 0.75)
mtext(side = 1, "In anti-phase", line = 0, cex = 0.75)
```

```
mtext(side = 4, "CCat leads ACL", line = -5, cex = 0.75)
mtext(side = 2, "ACL leads CCaT", line = -5, cex = 0.75)

par(mar=c(0.5,0.5,2.5,0.5))
plot(x_deca_1,y_deca_1, bty="n", axes = F, type = 'p', xlim = c(-1, 1), ylim = c(-1,1),xaxs="i",
yaxs="i", asp = 1, col="darkslategray1", xlab = "", ylab = "")
draw.circle(x = c(0,0,0,0,0),y = c(0,0,0,0,0), radius = c(1,0.8, 0.6, 0.4, 0.2), col = "grey")
segments(-1,0,1,0)
segments(0,-1,0,1)
segments(cos(pi/4),cos(pi/4),sin(-pi/4),sin(-pi/4))
segments(-cos(pi/4),cos(-pi/4),sin(pi/4),sin(-pi/4))
Arrows(0,0,x_deca_1,y_deca_1, code = 2, col = "darkslategray1", lwd = 5,
arr.type="curved",arr.adj = 1)
mtext(side = 3, "decadal scale",line = 1)
mtext(side = 3, "In phase", line = 0, cex = 0.75)
mtext(side = 1, "In anti-phase", line = 0, cex = 0.75)

par(mar=c(0.5,0.5,2.5,0.5))
plot(x_cent_1,y_cent_1, bty="n", axes = F, type = 'p', xlim = c(-1, 1), ylim = c(-1,1),xaxs="i",
yaxs="i", asp = 1, col="darkslategray1", xlab = "", ylab = "")
draw.circle(x = c(0,0,0,0,0),y = c(0,0,0,0,0), radius = c(1,0.8, 0.6, 0.4, 0.2), col = "grey")
segments(-1,0,1,0)
segments(0,-1,0,1)
segments(cos(pi/4),cos(pi/4),sin(-pi/4),sin(-pi/4))
segments(-cos(pi/4),cos(-pi/4),sin(pi/4),sin(-pi/4))
Arrows(0,0,x_cent_1,y_cent_1, code = 2, col = "darkslategray1", lwd = 5,
arr.type="curved",arr.adj = 1)
mtext(side = 3, "centennial scale",line = 1)
mtext(side = 3, "In phase", line = 0, cex = 0.75)
mtext(side = 1, "In anti-phase", line = 0, cex = 0.75)

# Plot ACL vs. Uk37 ----
par(mar=c(0.5,0.5,2.5,0.5))
plot(x_year_2,y_year_2, bty="n", axes = F, type = 'p', xlim = c(-1, 1), ylim = c(-1,1),xaxs="i",
yaxs="i", asp = 1, col="darkslategray1", xlab = "", ylab = "")
draw.circle(x = c(0,0,0,0,0),y = c(0,0,0,0,0), radius = c(1,0.8, 0.6, 0.4, 0.2), col = "grey")
segments(-1,0,1,0)
segments(0,-1,0,1)
segments(cos(pi/4),cos(pi/4),sin(-pi/4),sin(-pi/4))
segments(-cos(pi/4),cos(-pi/4),sin(pi/4),sin(-pi/4))
Arrows(0,0,x_year_2,y_year_2, code = 2, col = "darkslategray1", lwd = 5,
arr.type="curved",arr.adj = 1)
mtext(side = 2, "ACL vs. Uk37",line = -3)
mtext(side = 3, "In phase", line = 0, cex = 0.75)
mtext(side = 1, "In anti-phase", line = 0, cex = 0.75)

par(mar=c(0.5,0.5,2.5,0.5))
plot(x_deca_2,y_deca_2, bty="n", axes = F, type = 'p', xlim = c(-1, 1), ylim = c(-1,1),xaxs="i",
yaxs="i", asp = 1, col="darkslategray1", xlab = "", ylab = "")
draw.circle(x = c(0,0,0,0,0),y = c(0,0,0,0,0), radius = c(1,0.8, 0.6, 0.4, 0.2), col = "grey")
segments(-1,0,1,0)
```

```
segments(0,-1,0,1)
segments(cos(pi/4),cos(pi/4),sin(-pi/4),sin(-pi/4))
segments(-cos(pi/4),cos(-pi/4),sin(pi/4),sin(-pi/4))
Arrows(0,0,x_deca_2,y_deca_2, code = 2, col = "darkslategray1", lwd = 5,
arr.type="curved",arr.adj = 1)
mtext(side = 3, "In phase", line = 0, cex = 0.75)
mtext(side = 1, "In anti-phase", line = 0, cex = 0.75)

par(mar=c(0.5,0.5,2.5,0.5))
plot(x_cent_2,y_cent_2, bty="n", axes = F, type = 'p', xlim = c(-1, 1), ylim = c(-1,1),xaxs="i",
yaxs="i", asp = 1, col="darkslategray1", xlab = "", ylab = "")
draw.circle(x = c(0,0,0,0,0),y = c(0,0,0,0,0), radius = c(1,0.8, 0.6, 0.4, 0.2), col = "grey")
segments(-1,0,1,0)
segments(0,-1,0,1)
segments(cos(pi/4),cos(pi/4),sin(-pi/4),sin(-pi/4))
segments(-cos(pi/4),cos(-pi/4),sin(pi/4),sin(-pi/4))
Arrows(0,0,x_cent_2,y_cent_2, code = 2, col = "darkslategray1", lwd = 5,
arr.type="curved",arr.adj = 1)
mtext(side = 3, "In phase", line = 0, cex = 0.75)
mtext(side = 1, "In anti-phase", line = 0, cex = 0.75)

# Plot CCaT vs. Uk37 ----
par(mar=c(1,0.5,2.5,0.5))
plot(x_year_3,y_year_3, bty="n", axes = F, type = 'p', xlim = c(-1, 1), ylim = c(-1,1),xaxs="i",
yaxs="i", asp = 1, col="darkslategray1", xlab = "", ylab = "")
draw.circle(x = c(0,0,0,0,0),y = c(0,0,0,0,0), radius = c(1,0.8, 0.6, 0.4, 0.2), col = "grey")
segments(-1,0,1,0)
segments(0,-1,0,1)
segments(cos(pi/4),cos(pi/4),sin(-pi/4),sin(-pi/4))
segments(-cos(pi/4),cos(-pi/4),sin(pi/4),sin(-pi/4))
Arrows(0,0,x_year_3,y_year_3, code = 2, col = "darkslategray1", lwd = 5,
arr.type="curved",arr.adj = 1)
mtext(side = 2, "CCaT vs. Uk37",line = -3)
mtext(side = 3, "In phase", line = 0, cex = 0.75)
mtext(side = 1, "In anti-phase", line = 0, cex = 0.75)

par(mar=c(1,0.5,2.5,0.5))
plot(x_deca_3,y_deca_3, bty="n", axes = F, type = 'p', xlim = c(-1, 1), ylim = c(-1,1),xaxs="i",
yaxs="i", asp = 1, col="darkslategray1", xlab = "", ylab = "")
draw.circle(x = c(0,0,0,0,0),y = c(0,0,0,0,0), radius = c(1,0.8, 0.6, 0.4, 0.2), col = "grey")
segments(-1,0,1,0)
segments(0,-1,0,1)
segments(cos(pi/4),cos(pi/4),sin(-pi/4),sin(-pi/4))
segments(-cos(pi/4),cos(-pi/4),sin(pi/4),sin(-pi/4))
Arrows(0,0,x_deca_3,y_deca_3, code = 2, col = "darkslategray1", lwd = 5,
arr.type="curved",arr.adj = 1)
mtext(side = 3, "In phase", line = 0, cex = 0.75)
mtext(side = 1, "In anti-phase", line = 0, cex = 0.75)

par(mar=c(1,0.5,2.5,0.5))
plot(x_cent_3,y_cent_3, bty="n", axes = F, type = 'p', xlim = c(-1, 1), ylim = c(-1,1),xaxs="i",
```

```
yaxs="i", asp = 1, col="darkslategray1", xlab = "", ylab = "")
draw.circle(x = c(0,0,0,0,0),y = c(0,0,0,0,0), radius = c(1,0.8, 0.6, 0.4, 0.2), col = "grey")
segments(-1,0,1,0)
segments(0,-1,0,1)
segments(cos(pi/4),cos(pi/4),sin(-pi/4),sin(-pi/4))
segments(-cos(pi/4),cos(-pi/4),sin(pi/4),sin(-pi/4))
Arrows(0,0,x_cent_3,y_cent_3, code = 2, col = "darkslategray1", lwd = 5,
arr.type="curved",arr.adj = 1)
mtext(side = 3, "In phase", line = 0, cex = 0.75)
mtext(side = 1, "In anti-phase", line = 0, cex = 0.75)
}
```

Python Script for video generation (Credits: Sreejith Varma)

```
##############################################################################
# python script to convert a series of graph plot images into a single graph image and then
create
# a video showing a compressed version of the single graph and a zoomed version of the same
below
# The script reads a txt file with names of the images, their start and end regions in pixels
# each image is cropped based on start and end positions and then stitched together with a line
# connecting the graphs using start and end pixels
# the script uses opencv-python for image processing (cv2)
##############################################################################
# loads opencv & numpy libraries
import cv2
import numpy as np
# creates lists of images, start and end regions as well as start and end pixels
# each image is cropped using start and end regions (spos & epos)
# the images are then stitched together end of prev to start of next
# a line is drawn to complete the graph using end pixel (epix_x, epix_y) of prev
# to start pixel (spix_x, spix_y) of next
img = [ ]; spos = [ ]; epos = [ ]; spix_x = [ ]; spix_y = [ ]; epix_x = [ ]; epix_y = [ ]
# each input image must be of same height and width as h & w
# zoom region is of value s;
# the final video has the compressed & zoom image seperated by m pixels horizontally
h = 462; w = 1022; s = 1022; m = 30
# the final image height =
# h_fin (compressed image height at top) + h_z (zoomed image height at bot) + m (separator)
pixels
# the final image width =
# w_fin (compressed image width at top) + w_z (pixels at start showing the y-axix; same for
both) pixels
h_fin = 240; w_fin = 1280
h_z = 475; w_z = 70
# creates the output video named output.avi in running folder of type DIVX, 120 fps and size as
above
fourcc = cv2.VideoWriter_fourcc('D','I','V','X')
out = cv2.VideoWriter('output.avi', fourcc, 60.0, (w_fin+w_z, h_fin+h_z+m))
# reads the images.txt file and loads the arrays with relevent file name and position pixel data
```

```
lines = [line.rstrip('\n') for line in open('images.txt')]
for i in range(len(lines)):
    linedata = lines[i].split(';')
    filename = linedata[0]
    spos.append(int(linedata[1]))
    epos.append(int(linedata[2]))
    spix_x.append(int(linedata[3]))
    spix_y.append(int(linedata[4]))
    epix_x.append(int(linedata[5]))
    epix_y.append(int(linedata[6]))
    #print(filename, size)
    img.append(cv2.imread(filename))
# creat a concatanated image from each with crop and line fitting
img_cat = np.zeros((h, w*len(lines), 3), dtype=np.uint8)
print(len(img))
w_start = 0; w_end = 0;
for i in range(len(img)):
    print(img[i].shape)
    c_s = spos[i]; c_e = epos[i];
    img_resize = cv2.resize(img[i], (w, h))
    # crops images according to the start and end positions in x-axis
    if i == 0:
        img_resize = img_resize[0:h, 0:c_e]
    else:
        img_resize = img_resize[0:h, c_s:c_e]
    img_width = img_resize.shape[1]
    w_start = w_end; w_end = w_end + img_width
    print(img_width, ',', w_start, ',', w_end)
    # concatanates it into a single image
    img_cat[0:h, w_start:w_end] = img_resize
    # adds a line based on start and end pixels
    if i > 0:
        p_sx = epix_x[i-1]; p_sy = epix_y[i-1]; p_ex = spix_x[i]; p_ey = spix_y[i]
        d_s = epos[i-1] - p_sx; d_e = p_ex - c_s
        cv2.line(img_cat, (w_start-d_s, p_sy), (w_start+d_e, p_ey), (0, 0, 255), 2)
img_cat_crop = img_cat[0:h, 0:w_end]
scl = w_end/(w_fin+w_z)
# creates a video with concat image on top and zoom image at bottom and m pix separation
# create rectangles and lines to show the region of concat image being shown in zoom image
# the image is then written into the output file as well as displayed for checking
# (0, 0, 255) gives red, (255, 0, 0) gives blue and (0, 110, 0) gives green in rectangle and line
for i in range(w_end-w_z-s+1):
    img_fin = np.zeros((h_fin+h_z+m, w_fin+w_z, 3), dtype=np.uint8)
    img_fin[0:h_fin, 0:w_fin+w_z] = cv2.resize(img_cat_crop, (w_fin+w_z, h_fin))
    img_fin[h_fin+m:h_fin+h_z+m, 0:w_z] = cv2.resize(img_cat_crop[0:h, 0:w_z], (w_z, h_z))
    img_fin[h_fin+m:h_fin+h_z+m, w_z:w_fin+w_z] = cv2.resize(img_cat_crop[0:h,
i+w_z:i+w_z+s], (w_fin, h_z))
    cv2.rectangle(img_fin, (int((i+w_z)/scl), 0), (int((i+w_z+s)/scl), h_fin), (0, 0, 255), 2)
    cv2.rectangle(img_fin, (w_z, h_fin+m), (w_fin+w_z, h_fin+h_z+m), (0, 0, 255), 2)
    cv2.line(img_fin, (int((i+w_z)/scl), h_fin), (w_z, h_fin+m), (0, 0, 255), 1)
    cv2.line(img_fin, (int((i+w_z+s)/scl), h_fin), (w_fin+w_z, h_fin+m), (0, 0, 255), 1)
```

```
    out.write(img_fin)
    #cv2.imshow("fin", img_fin)
    cv2.imshow("fin", cv2.resize(img_fin, (640, 480)))
    cv2.waitKey(2)
    out.release()
cv2.destroyAllWindows()
```